SYNTHETIC PATHWAYS TO MESOSTRUCTURED SUPERCONDUCTORS: QUANTUM MATERIALS FROM BLOCK COPOLYMER SELF-ASSEMBLY

A Dissertation

Presented to the Faculty of the Graduate School

of Cornell University

In Partial Fulfillment of the Requirements for the Degree of

Doctor of Philosophy

by

Peter Abraham Beaucage

December 2018

SYNTHETIC PATHWAYS TO MESOSTRUCTURED SUPERCONDUCTORS: QUANTUM MATERIALS FROM BLOCK COPOLYMER SELF-ASSEMBLY

Peter Abraham Beaucage, Ph. D.

Cornell University 2018

The ability to precisely control the properties of materials using atomic structure developed over the last 50 years directly led to the high-performance semiconductor based devices that have revolutionized modern life. Complex ordered mesoscale structures such as those prepared by block copolymer self-assembly may prove to be a powerful tool for tuning the electronic properties of materials, but few have explored this area, largely due to a lack of connections between the disparate fields of atomic quantum materials and soft matter self-assembly. In particular, the impact of three-dimensional mesoscale order on superconductors has not been explored at all, despite the possibility for emergent properties including increased critical fields, angle-dependent magnetic behavior, and symmetry-forbidden nonlinear magnetic and electronic properties. In this thesis, three routes to mesostructured superconductors using block copolymer self-assembly are developed to bridge this gap and form a stable platform for future mesostructure-superconductivity correlation studies.

In the first route, poly(isoprene-b-styrene-b-ethylene oxide) (ISO) triblock terpolymers are used to structure-direct niobium (V) oxides, which are subsequently converted to niobium nitrides via an optimized annealing procedure in ammonia gas. The resulting materials are superconductors with T_c of 7.8K. We demonstrate that the length scale and morphology of these materials can be tuned by varying the block copolymer dimensions and show first evidence of magnetic flux pinning on the mesoscale pores

of the material.

In the second route, intermediate oxynitrides are converted into carbonitrides, using a variety of times, temperatures, and gas compositions to more fully explore the compositional flexibility of the niobium-(oxygen)-nitrogen-carbon pseudo-ternary system. The best resulting carbonitrides have increased T_c of up to 16.0 K, nearing values expected for the bulk material, as well as improved mesostructure retention despite treatment at temperatures of up to 1000 ˚C. To demonstrate the versatility of this approach, materials with four distinct morphologies (alternating gyroid network, perforated lamellae, double gyroid matrix, and inverse hexagonal cylinders) are prepared using a single parent ISO terpolymer.

In the final route, mesoporous Si(ON) ceramic single mesocrystals are infiltrated with molten indium at pressures up to 40,000 psi. The resulting materials exhibit an inversion of the magnetic response from a type-I behavior characteristic of bulk In to a type-II behavior, coupled with an order-of-magnitude increase in the upper critical field. These results serve as a first demonstration of the plethora of fascinating emergent properties expected for superconducting mesostructures, and provide a robust, versatile, stable foundation for extensive mesostructure-superconductivity correlation studies.

BIOGRAPHICAL SKETCH

Peter Beaucage was born in Albuquerque, New Mexico on September 28th, 1991. After moving to Cincinnati, Ohio in 1994, he developed an interest in science at an early age, encouraged in no small part by countless hours spent with his father's graduate students and tagging along on trips to the Advanced Photon Source. At the age of twelve his family moved to Zürich, Switzerland for a yearlong sabbatical. He was fortunate to attend an immersive German program at Schulhaus Letten, where he was aided by incredible teachers, an inspiring cohort of global friends, and the breathtakingly beautiful surroundings. After returning to the US, he attended St. Xavier High School from 2005 to 2009, where he made countless lifelong friends and was instilled with values that inspire him to this day, particularly a staunch commitment to social justice and an ethos of responsible scholarship. Particular achievements include founding a 501(c)(3) nonprofit that continues to operate to this day, learning to weld to build theater sets, writing Monte Carlo simulations, participating in mock trial and copy-editing the school newspaper, and playing bass in the theater orchestra, where 17-hour days were good preparation for synchrotron runs. After graduating, Peter attended the University of Cincinnati, where he studied Chemical Engineering. He began pursuing research work during his first year, using SAXS to probe the micellization behavior of sucrose-esters as drug delivery agents in the lab of Prof. Carlos Co. That involvement led him to co-op work terms at the USAXS beamline at Argonne National Laboratory, where he had the opportunity to work with groups from across the field of materials science, studying everything from molten superalloys to solid hydrogen to penguin feathers. He also worked for an extended summer in the computational fluid dynamics group at Evonik Industries in Hanau, Germany and did additional work on SANS characterization of star polymers at Cincinnati. Peter was very active outside research and coursework as well;

highlights included a voting seat on curriculum and academic standards committees, managing a career fair for the Engineering college, leading student trips to Turkey and Ethiopia as an undergraduate TA and eventually expending his nonprofit there, and winning the national Chem-E Jeopardy championship at the 2012 AIChE meeting as a part of the Chem-E-Car team. He graduated with a B.S. in Chemical Engineering, *cum laude*, in May of 2013.

Since August 2013, he has been pursuing a Ph.D. at Cornell University working jointly between the groups of Profs. Uli Wiesner and Sol Gruner.

for all those who venture into the unknown

just for the fun of it

ACKNOWLEDGMENTS

None of the work done in my PhD would have been possible without a tremendous amount of advice, assistance, inspiration, and motivation from the best group of friends, family, mentors, and collaborators I could have ever hoped for. I am additionally very grateful to those funded this work; specific agencies and grants are acknowledged at the end of the corresponding chapters for clarity.

I first and foremost owe a tremendous debt of gratitude to my special committee. Uli, Sol, and Frank have been the best possible role models and mentors, giving me the space to define my own work while always being close by when encouragement, assistance, or insight was needed. Their infectious enthusiasm for great science, commitment to doing important and high-quality science, and incredible intuition are a constant inspiration to me.

My colleagues across these three groups were a continuous source of camaraderie, mentorship, and amazingly fun collaborations. Particular thanks are owed to Dr. Hiroaki Sai, Dr. Spencer Robbins, Dr. Jörg Werner, Dr. Kate Barteau for their assistance in quickly starting in the group and their ongoing help. I enjoyed fruitful collaborations and many good times in the office with Dr. Ethan Susca, Dr. Kasia Oleske, Dr. Yuk Mun Li, Dr. Qi Zhang, Sarah Hesse, Paxton Thedford, Swathi Rao, Leonie Deilmann, and others in the group.

A number of faculty from across the university were particularly helpful in providing advice, consultation, and mentorship. I particularly wish to thank Prof. Bruce van Dover for teaching me superconductivity in countless drop-in visits, Prof.

Lara Estroff for inspiring me to pursue a career that includes teaching, Prof. Mike Thompson for many friendly and helpful discussions, and Prof. Itai Cohen for showing me how to turn science into great stories.

I am grateful to Dr. Arthur Woll at CHESS for constant help with instrumentation and a (perhaps reckless) belief in my ability to work unsupervised with multi-million dollar equipment, but more importantly for his ongoing mentorship and support. He introduced me to some of the most fun collaborations I've done in the last five years.

I'll fondly remember the many good times after 2 am with the late-night scattering crew at CHESS and at other facilities, particularly Howie Joress, Bob Bell, Alan Jacobs, David Lynch, Kate Barteau, Hiro Sai, Jörg Werner, Sarah Hesse, Paxton Thedford, and more recently Aine Connolly, Johnny Zhang, Mike Thompson, and Bruce van Dover. *After we fix this one problem we can go to sleep!*

I'm grateful to Dr. Dave Moore at the National Renewable Energy Lab for assisting me during a six-month visit there during my Ph.D. work, and for consistently helpful advice and support.

Science is built on the back of miraculous technical achievements by people who too often go uncredited, and I owe thanks to many support staff. Marty Novak and Dave Wise provided outstanding machining and glassblowing support, respectively, turning hasty sketches and "hey-do-you-think-we-could…" into finished realities in minutes. Steve Kriske maintained the Physical Property Measurement System used in all superconductor characterization, Phil Carubia maintained some of the x-ray diffractometers used in this work, and Tony Condo managed the polymer

characterization and NMR facilities. The *in situ* nitriding and XLAM studies described here would not have been possible without the assistance of the entire CHESS operations group, in particular Dana Richter, John Conrad, and Kurt MacDonald, who on many occasions saved an experiment in the wee hours of the morning. And Dr. Mark Tate, a brilliant scientist in his own right, took countless hours away from his own work to help me maintain the rotating anode SAXS camera.

I would never have gone down this path if not for a number of teachers and mentors who took risks to believe in me with little reason to, nudged me at critical moments in what proved to be the right direction, and have provided ongoing mentorship and support. Special thanks go to John D'Alessandro, Wally Koral, Larry Merkel, and Tom Cline of St. Xavier High School, Prof. Carlos Co at the University of Cincinnati, and Dr. Jan Ilavsky at Argonne National Lab.

Alex Boys, Ethan Susca, Bob Bell, Karen Heinselman, Joe Caron, Heather Hunt, Ben MacMurray, Dave Moore, Ryan Page, Duncan Sutherland, Matt Barone, Dan Weinstock, and countless others turned my time at Cornell from a productive Ph.D. to some of the best years of my life. I will never forget the board game nights, wine tours, backpacking trips, hockey games, hikes, nights at the coffee roaster, kickball games, and other adventures.

Finally, but perhaps most significantly, I would like to thank my family for their love, inspiration, and support.

TABLE OF CONTENTS

LIST OF FIGURES

LIST OF TABLES

CHAPTER 1

INTRODUCTION

Block Copolymer Self-Assembly for Nanoscale Structures

Block copolymer self-assembly (BCP SA) has emerged over the past several decades as a robust, versatile, and tunable method for accessing three dimensional ordered structures with length scales typically between 10-100 nm. In particular, BCP SA allows access to a variety of low-symmetry network phases (including the alternating gyroid, double/alternating diamond, and others) with length scales and morphologies quantitatively tunable by changing block lengths. While neat block copolymers can incorporate chemical functionality e.g. for ion transport, they have found some of their most exciting applications in the templating of inorganic materials, beginning with aluminosilicates(*1*) and extending through to functional materials from metals(*2*) to semiconductors(*3*). The exceptionally high specific surface areas and accessible pores in these materials have led them to a large number of applications in energy conversion and storage, such as fuel cell electrodes(*4*), solar cells(*5*), and even integrated nanobatteries(*6*). One relatively unexplored area, however, is the application of the ordered nature of block copolymer derived nanostructures to manipulate material properties, e.g. the photonic or phononic behavior. Theoretical studies have shown that even relatively simple materials such as metals can have rich emergent electronic properties from low-symmetry mesostructures. For example, a low-loss metal gyroid can exhibit circularly polarized light propagation and photonic bandgaps, potentially allowing access to negative index of refraction in the visible

range(*7*). Further theoretical studies have shown the existence of topologically protected Weyl points in strained alternating gyroids(*8*), and the existence of phononic bandgaps in gyroids and several other network structures accessible with BCP SA(*9*).

Mesoscopic Effects in Superconductors

Superconductors are a prominent example of the type of correlated electron system that might be expected to exhibit even more interesting emergent properties. It has been known for nearly as long as superconductivity has been well understood that confinement and order on the mesoscale can dramatically impact the properties of these materials(*10*). Superconductors are characterized by two phenomena: first, and most well known, an electrical resistance of exactly zero below a critical temperature, current, and magnetic field, and second, the spontaneous development of a circulating supercurrent that actively expels applied magnetic field. It is this phenomenon that leads to the most interesting emergent properties in structured superconductors. Particularly, in type II superconductors (all compounds and niobium and lead metals), rather than an immediate loss of the superconducting state above the critical field, the material allows the entry of discrete bundles of magnetic flux, separated by superconducting area. These “vortices”, and their movement through the material, control the magnetic behavior in the high field regime. They can be pinned on defect sites in the material, limiting their motion.

The work comprising this thesis forms a holistic approach to the synthesis of three-dimansionally crystallographically ordered mesoporous superconductors using block copolymer-inorganic hybrid co-assembly. Pathways are explored to three material

classes: the niobium oxynitrides, niobium carbonitrides, and finally mesostructured indium metal. The diversity of these pathways presents a substantial foundation for future experimental and theoretical exploration of the impacts of 3D mesoscale order on flux pinning and other properties in superconductors.

Outline

In chapter two, I present the first block copolymer self-assembly derived synthetic route to a mesostructured superconductor – niobium nitride with the alternating gyroid ($I4_132$) structure, templated by a poly(isoprene-block-styrene-block-ethylene oxide) ABC triblock terpolymer via ammoniolysis of sol-gel niobium oxide in two steps, isolating the challenge of controlled crystal growth (necessary for structure retention) from the oxygen-nitrogen exchange (necessary for superconductivity). The resulting materials have a T_c of about 7.8 K, dramatically below the best literature reported values of ca. 15 K, likely due to a significant retained oxygen fraction in the material. Nevertheless, the first potential evidence of flux pinning in such a material is observed as inflection points in high field-dependent magnetization.

In chapter three, I use *in situ* small- and wide-angle x-ray scattering (SAXS/WAXS) during ammoniolysis to demonstrate the extension of this synthetic route from the custom ABC triblocks to commercially available Pluronics ABA poly(ethylene oxide-b-propylene oxide-b-ethylene oxide) triblocks. The resulting hexagonally ordered niobium nitride is not superconducting due to a high fraction of oxygen, but demonstrates that the *in situ* apparatus developed is an extremely facile route to discovery of synthetic pathways to such materials. In addition, the ordered nitrides may prove to be interesting materials for catalysis or other applications.

In chapter four, I first extend the methodology previously developed to produce niobium carbides by annealing a preliminary nitride in a blend of methane, hydrogen, and nitrogen at temperatures up to 1000 ˚C. The resulting carbides have improved structure retention (relative to the nitrides from chapter two) and exhibit nearly two orders of magnitude higher flux exclusion and T_c as high as 16 K. By variation of the annealing temperature, the final [C/N] ratio can be varied resulting in materials with different superconducting transition temperature. This synthetic route is used to demonstrate the versatility of the block copolymer-derived synthesis by preparing materials with four different morphologies from a single parent ISO triblock terpolymer: hexagonal cylinders, the double-gyroid matrix ($Ia3d;Q^{230}$), perforated lamellae, and the alternating gyroid network phase ($I4_132;Q^{214}$). Interestingly, the superconducting transition temperature of the four morphologies vary by as much as 4 K from morphology to morphology with minimal variation of the underlying lattice parameter – suggesting that confinement effects or even potentially effects of the order may be influencing the superconducting behavior.

In chapter five, a method is developed using laser spike annealing and microbeam synchrotron diffraction to perform high-throughput studies of material processing, a technique we term XLAM (X-ray Laser Anneal Mapping). The technique is applied, as first proof of principle, to bismuth oxide. The delta phase of bismuth oxide has the highest known oxygen ion conductivity of any solid oxide, but is only stable about 730 ˚C. Previous attempts to stabilize it by rapid cooling have been unsuccessful, while stabilization by alloying with other materials results in a dramatically reduced conductivity. Using XLAM, we discover a rapid-quench processing regime where the

delta phase can be stabilized to room temperature, resulting in a material with an oxygen ion conductivity of 10^{-5} S cm^{-1}, the highest reported value for any solid oxide at room temperature by several orders of magnitude. This method can be readily applied to high-throughput annealing studies of mesostructured materials (e.g. by performing combined microbeam GISAXS-WAXS) and may result in the discovery of processing regimes that lead to other families of block copolymer-derived mesostructured superconductors, e.g. complex oxides.

In chapter six, a route to block copolymer derived mesoporous superconductors is developed based on infiltration of a mesostructured Si(O,N) ceramic with molten indium at pressures around 30,000 psi. The resulting materials exhibit a broadened superconducting transition, with a small fraction of the material becoming superconducting at temperatures as high as 3.7 K (as compared to the bulk value of 3.1 K). More interestingly, the material's field-dependent magnetization behavior switches from a classic type-I system (as expected and measured for bulk In) to a hysteretic curve characteristic of a type-II material. The critical field at which no superconducting fraction remains is enhanced from about 150 Oe to well over 1200 Oe. This result is explained as a consequence of the confinement of the material to a small thickness, with resulting dramatic decrease in the coherence length allowing the existence of vortices in the material.

REFERENCES

1. M. Templin *et al.*, *Science.* **278**, 1795–8 (1997).
2. S. C. Warren *et al.*, *Nat. Mater.* **11**, 460–467 (2012).
3. H. Arora *et al.*, *Science.* **330**, 214–219 (2010).
4. J. Lee *et al.*, *Nat. Mater.* **7**, 222–228 (2008).
5. E. J. W. Crossland *et al.*, *Nano Lett.* **9**, 2807–12 (2009).
6. J. G. Werner, G. G. Rodríguez-Calero, H. D. Abruña, U. Wiesner, *Energy Environ. Sci.* **11**, 1261–1270 (2018).
7. K. Hur *et al.*, *Angew. Chemie - Int. Ed.* **50**, 11985–11989 (2011).
8. M. Fruchart *et al.*, *Proc. Natl. Acad. Sci. U. S. A.* **115**, E3655–E3664 (2018).
9. K. Hur, R. G. Hennig, U. Wiesner, *J. Phys. Chem. C.* **121**, 22347–22352 (2017).
10. R. Doll, M. Näbauer, *Phys. Rev. Lett.* **7**, 51–52 (1961).

CHAPTER 2

BLOCK COPOLYMER SELF-ASSEMBLY DIRECTED SYNTHESIS OF MESOPOROUS GYROIDAL SUPERCONDUCTORS[1]

Abstract

Superconductors with periodically ordered mesoporous structures are expected to have very different properties compared to their bulk counterparts. Systematic studies of such phenomena to date are sparse, however, due to a lack of versatile synthetic approaches to such materials. Here we demonstrate the formation of three-dimensionally (3D) continuous gyroidal mesoporous niobium nitride (NbN) superconductors from chiral ABC triblock terpolymer self-assembly directed sol-gel derived niobium oxide (Nb_2O_5) with subsequent thermal processing in air and ammonia gas (NH_3). Superconducting materials exhibit a critical temperature, T_c, of about 7-8 K, a flux exclusion of about 5% compared to a dense NbN solid, and an estimated critical current density, J_c, of 440 A/cm^2 at 100 Oe and 2.5 K. We expect block copolymer self-assembly directed mesoporous superconductors to provide interesting subjects for mesostructure-superconductivity correlation studies.

Introduction

Mesoscale structures in the form of periodically ordered mesoporous arrays with pore sizes between 2 and 50 nm and various achiral or chiral mesoscale

[1] Spencer W. Robbins, Peter A. Beaucage, Hiroaki Sai, Kwan Wee Tan, Jörg G. Werner, James P. Sethna, Francis J. DiSalvo, Sol M. Gruner, R. Bruce van Dover, Ulrich Wiesner, *Science Advances* e1501119 (2016).

morphologies are expected to affect the properties of superconductors, including their critical field, critical current, and flux pinning behavior (*1-6*). Despite growing interest in mesoscale science (*7*), to date only a few studies exist pursuing these phenomena. For example, there have been reports of a superconducting oxide asymmetric membrane with a mesoporous layer on a macroporous substrate (*8*), a sputtered superconducting Nb layer on a nanoporous Si substrate (*9*), of lithographically fabricated Nb shifted strip arrays (*10*), and biotemplated oxide superconductors with micron-scale structural ordering (*11*). The sparsity of such studies is due, in part, to a lack of synthetic approaches to mesostructured superconductors allowing systematic investigations of the effect of mesostructure on superconductivity. In all these cases, the materials in question were prepared by lithographic or templating approaches, not self-assembly, and as a result offer limited tunability and no access to three-dimensional, chiral morphologies.

Block copolymer (BCP) self-assembly (SA) has proven to be a powerful tool to direct the feature size, morphology, and porosity of various functional inorganic materials on the mesoscale (*12, 13*). In principle, this structural control provides an ideal platform for tuning and studying mesostructural effects on superconducting properties of inorganic materials, but has not been exploited to date. To the best of our knowledge, the sole example in peer-reviewed literature involving block copolymers and superconductors describes the deposition of ferromagnetic/superconducting bilayers on a diblock copolymer substrate *(14)*. In contrast, here we demonstrate the use of BCP SA to structure direct a superconductor, niobium nitride (NbN), into films of periodically ordered mesoporous materials with the alternating gyroid (G^A)

morphology exhibiting a superconducting transition at 7-8 K. We expect this study to pave the way towards investigations of superconductors with a plethora of BCP SA directed mesostructures.

Results and Discussion

We used two triblock terpolymers poly(isoprene)-*block*-poly(styrene)-*block*-poly(ethylene oxide) with molar masses of 63.8 kg mol^{-1} (ISO-64k) and 86.2 kg mol^{-1} (ISO-86k), to structure direct sol-gel derived niobium oxide (Nb_2O_5) into 3D alternating gyroid network structures by solvent evaporation-induced self-assembly (Figure 2.1) (*15*). BCP directed co-continuous cubic gyroid structures usually consist of two interpenetrating network sub-volumes related to one another by an inversion operation (*16*). If these two minority networks are constituted by the same block (*e.g.* in AB diblock copolymers), the structure is referred to as a double gyroid ($G^D, Ia\bar{3}d$) (*16*). In the case pursued here where the two minority sub-volumes are made up of different blocks (*i.e.* the A and C end blocks in ABC triblock terpolymers; blue and green blocks/volumes in Figure 2.1), the resulting chiral structure is called the alternating (or single) gyroid (G^A, $I4_132$) and lacks an inversion center in its unit cell (*16*). The chemical structures of the ISO terpolymers and inorganic sol-gel precursors used in this study are depicted in Figure 2.1 (left) together with a schematic of the synthesis approach and evolution of the alternating gyroid structure during different processing steps (bottom).

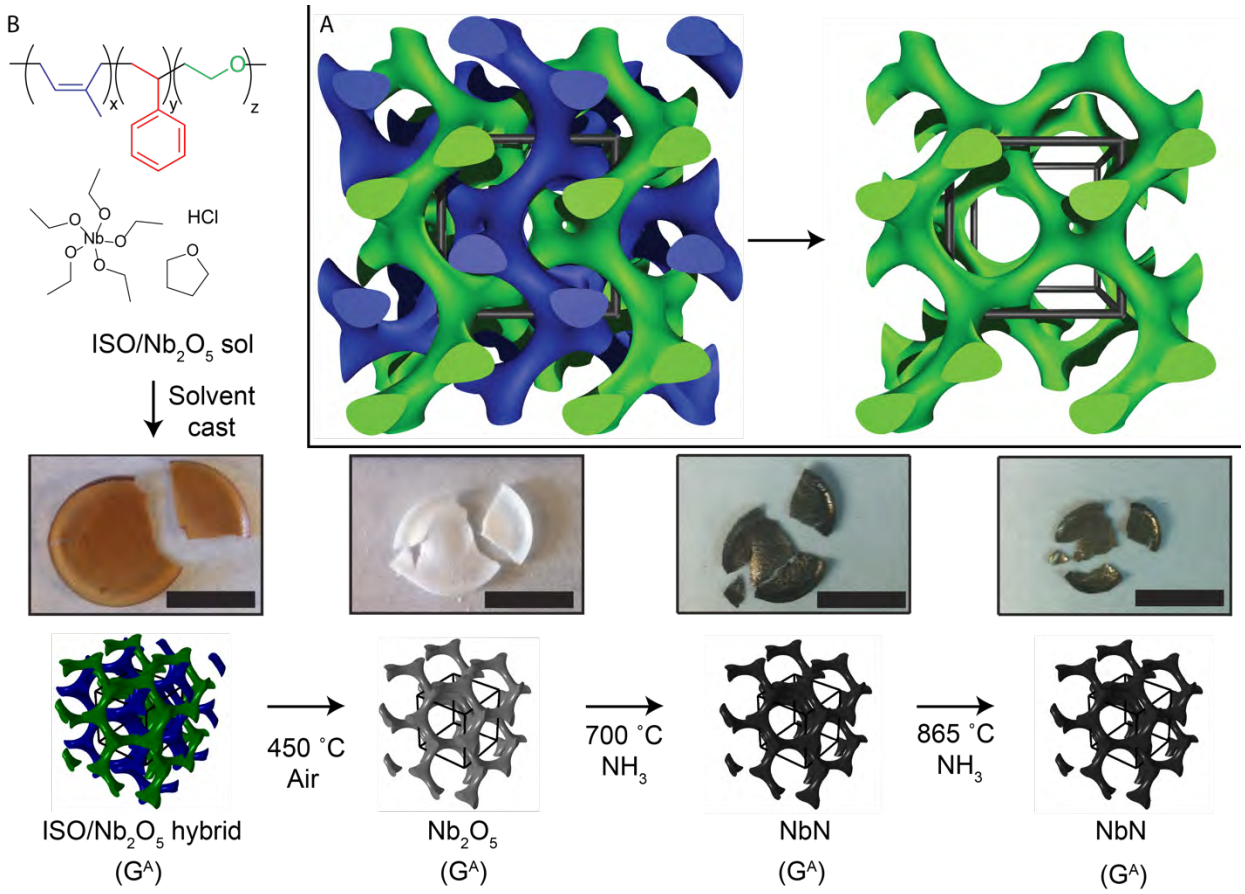

Fig. 2.1. (A) Alternating gyroid before and after processing with unit cell indicated by black cube and (B) chemical structures of compounds (left) and schematic of synthesis and processing steps with photographs of final materials (bottom). Block terpolymers ISO are combined with the Nb_2O_5 sol-gel precursors in a common solvent. Hybrid BCP/Nb_2O_5 alternating gyroid (G^A) structures are generated by solvent evaporation induced self-assembly. After calcination in air the mesoporous Nb_2O_5 G^A's are transformed *via* a two-step nitriding process to NbN G^A's. Scalebars in all photographs represent 1 cm.

Superconducting NbN has been previously synthesized by nitriding sol-gel derived Nb_2O_5 fibers (*17)*. The resulting materials were not mesoporous and required

nitriding temperatures of 1050 °C to exhibit superconductivity. Finding appropriate thermal treatments of BCP directed mesoporous inorganic materials is typically a balance between optimizing structure preservation by reducing processing temperatures and improving material properties by increasing processing temperatures. At 1050 °C, the mesostructure of the present BCP SA directed materials collapsed (see Figure 2.S1). Lower nitriding temperatures of 600 °C used earlier (*18*), or even 700 °C, retained the mesostructure well but resulting materials were not superconducting. Numerous heating profiles were explored to strike a balance between superconductivity and the retention of an ordered mesoporous structure. Ultimately, a two-step nitriding procedure consisting of first nitriding at 700 °C, then cooling to room temperature, and finally re-nitriding at 850-865 °C was necessary to successfully generate periodically ordered mesoporous nitrides that exhibited a superconducting transition. Interestingly, while materials nitrided in a single step at 850 °C retained ordered mesoporosity, they were not superconducting.

After solution casting and solvent evaporation, the terpolymers were removed by calcination in air at 450 ˚C, yielding freestanding single network alternating gyroidal mesoporous films of amorphous Nb_2O_5. The Nb_2O_5 alternating gyroids were converted into films of gyroidal mesoporous superconducting niobium nitride (NbN) by heating under flowing gaseous ammonia (NH_3) in two steps, first to 700 °C and subsequently to 850 ˚C for ISO-64k and 865 ºC for ISO-86k. The materials at different processing steps are depicted in Figure 2.1. The as-made hybrids exhibit a yellow/brown color that disappears for the oxides upon calcination to 450 ˚C. Nitrided samples appear as black and metallic shining solids. It is interesting that the materials

remain close to their original shape with only a few cracks, rather than disintegrating into many pieces or even powders upon heat treatments.

Small angle X-ray scattering (SAXS) was used to quantitatively characterize the mesostructural periodic order of ISO-64k/86k derived materials (Figure 2.2A/B) at various processing stages *(12)*. The SAXS patterns for as-made BCP-oxide hybrid materials (Figure 2.2A/B, bottom) are consistent with the alternating gyroid morphology and a d_{100}-unit cell size of 52.3 nm for ISO-64k and 61.8 nm for ISO-86k. After calcining in air at 450 °C (Figure 2.2A/B, second from bottom), the patterns remain consistent with the G^A morphology, but the peaks shift to higher q values and broaden, with a d_{100}-spacing of 37.2 nm for ISO-64k and 49.5 for ISO-86k. Peak broadening indicates some loss of long-range order of the mesoscale structure. The corresponding lattice shrinkage is typical during removal of organic material and condensation/crystallization of inorganic material in BCP-oxide systems (*18*). After nitriding under NH_3 first at 700 °C and then at 850/865 °C, the SAXS patterns continue to shift to higher q values and to broaden (Figure 2.2A/B, second from top and top). The 700 °C samples have d_{100}-spacings of 30.7 nm for ISO-64k and 43.8 nm for ISO-86k. While the ISO-86k derived sample treated to 865ºC shows higher order reflections consistent with a G^A lattice and a d_{100}-spacing of 35.7 nm, the ISO-64k derived sample brought to 850 °C only shows one reflection making structural lattice assignment by SAXS alone impossible. Assuming a G^A lattice the corresponding d_{100}-spacing from the first order reflection would be 27.0 nm. Using BCPs with different molar mass therefore enables tuning of the lattice parameters of the periodic SA

structures. In all samples except the ISO-64k derived 850ºC nitride, significant orientation of the mesostructure was observed, as indicated by spots in the two-dimensional SAXS patterns (Figures 2.S2-S3).

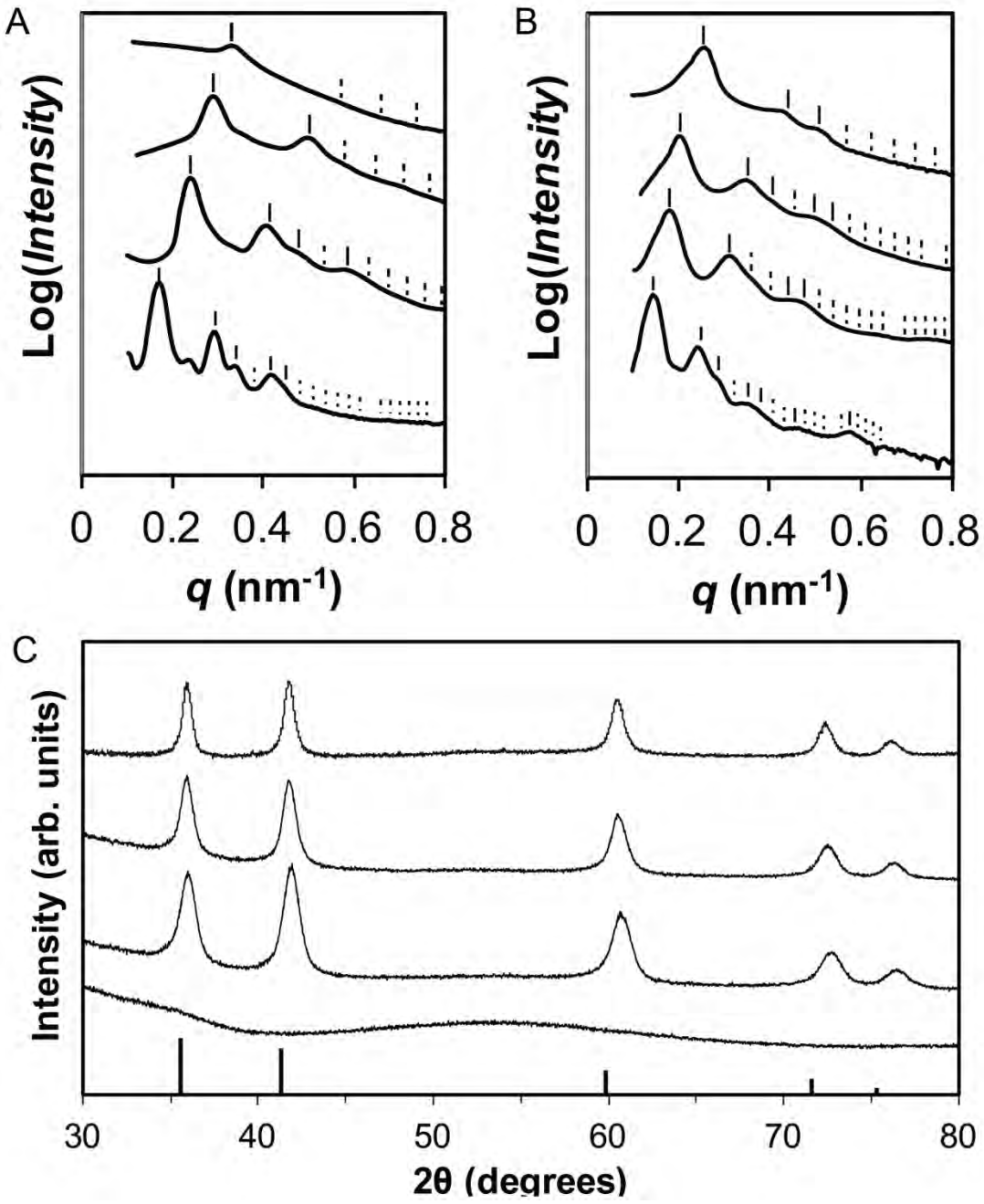

Fig. 2.2. Material characterization by X-ray scattering. (A,B) SAXS patterns of samples derived from ISO-64k (A) and ISO-86k (B) at various processing stages. From bottom to top: ISO/oxide hybrids; samples calcined at 450 °C in air: samples nitrided at 700 °C; sample nitrided at 850/865 °C. Observed (solid) and expected

(dashed) peak positions for the alternating gyroid (G^A) structure are indicated by ticks above each curve. Curves for the ISO-86k derived samples were integrated using a selected angular range due to significant orientation of the mesostructure. **(C)** Powder XRD patterns of samples at various processing stages. From bottom to top: sample calcined at 450ºC in air; samples nitrided at 700ºC, 850ºC, and 865ºC, respectively. All patterns are from samples derived from ISO-64k, except the top trace, which is from a sample derived from ISO-86k. Bottom tick marks indicate expected peak positions and relative intensities for a cubic rock salt niobium nitride pattern (PDF Card # 04-008-5125).

In order to corroborate the structural assignments from SAXS and to provide real space images of the structural sample evolution, scanning electron microscopy (SEM) was used to characterize the mesoscale morphology of the materials obtained at different processing stages. SEM images of ISO-64k and ISO-86k derived samples are shown in Figure 2.3 and Figure 2.S4. It is evident that as the materials progress through the heat treatments and shrink, they never completely lose their periodic order. Both final nitrides exhibit projections with four- and six- fold pore symmetry as expected for the cubic alternating gyroid morphology, further corroborating the structural assignments (Figure 2.S5-2.S6). Despite experiencing heat treatments up to 865 °C, the materials remained mesoporous rather than structurally collapsing.

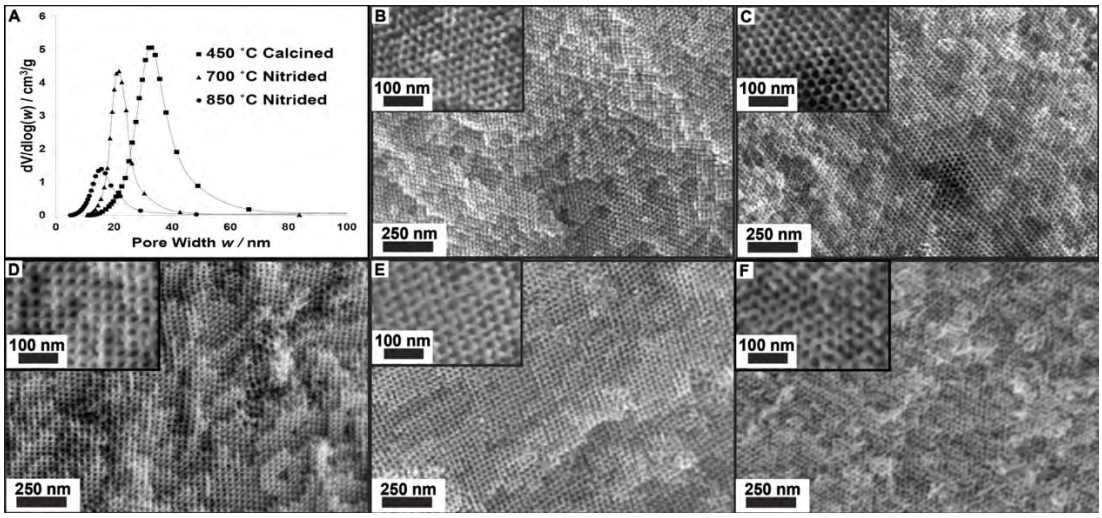

Fig. 2.3. Material characterization by N_2 sorption and Scanning Electron Microscopy (SEM). (A) Pore size distributions from N_2 sorption measurements for ISO-64k derived samples at various processing stages. **(B-F)** SEM images of mesoporous samples at different processing stages. ISO-64k derived gyroidal NbN after nitriding at 700 ºC (B) and after nitriding at 850 ºC (C). ISO-86k-derived gyroidal Nb_2O_5 after calcination at 450 °C in air (D); Gyroidal NbN after nitriding at 700 °C (E) and after nitriding at 865 °C (F).

Porosity was established and pore size distributions obtained *via* analysis of N_2 sorption measurements performed on powders of ISO-64k derived samples calcined at 450 °C, nitrided at 700 °C, and nitrided at 850 °C. The isotherms (Figure 2.S7) exhibit typical type-IV curves with H_1-type hysteresis (*18, 19)*. In all cases, as expected, the surface area is dominated by mesoporosity (diameters 2-50 nm) rather than microporosity (diameters <2 nm). In Figure 2.3A $dV/d\log(w)$ *vs*. pore width (where V is pore volume and *w* is pore width) is plotted for the three different samples

showing a decrease in average BJH model pore sizes from 31 nm to 21 nm to 16 nm with increasing processing temperature. Resulting surface areas and pore volumes are summarized in Table 2.S1. BET model surface areas decrease from 111 m^2 g^{-1} to 86 m^2 g^{-1} to 59 m^2 g^{-1}, while pore volumes decrease from 1.01 cm^3 g^{-1} to 0.71 cm^3 g^{-1} to 0.41 cm^3 g^{-1} for samples treated to 450 °C, 700 °C, and 850 °C, respectively. These results are consistent with the observations of structural shrinkage from SAXS and SEM and corroborate open and accessible mesoporosity. As an example, assuming a bulk density of 8.47 g cm^{-3} for the nitride and using the N_2 sorption-derived pore volume, the sample treated at 850 °C had 77.5% porosity.

The atomic crystal structure of the materials at different processing stages was characterized using powder X-ray diffraction (XRD, Figure 2.2C). After calcination, the BCP-directed oxides were amorphous Nb_2O_5 (Figure 2.2C, bottom). Nitriding at 700 °C for 12 h leads to material crystallization into a cubic rock salt structure, characteristic of many binary metal nitrides including NbN. From analysis of the XRD data, the cubic lattice parameter for this material is 4.31 Å. After further nitriding in the second step at 850 °C (Figure 2.2C, 2nd to top trace), the materials retained the rock salt structure but the lattice parameter increased to 4.33 Å. After further nitriding at 865ºC instead of 850 ºC (Figure 2.2C, top trace), the lattice parameter remained at 4.33 Å. The lattice parameter for the 850 °C and 865 ºC nitrided samples are similar to those measured by Nomura *et al.* using the same nitriding temperature for macroscopic Nb_2O_5 fibers (*17*) but are smaller than that of pure bulk cubic NbN (*17*,*20*). We attribute this difference in lattice parameter to residual oxygen content and

anion vacancies, consistent with a lattice parameter based compositional estimate based on Vegard's law (Figure 2.S8). Interestingly, Nomura *et al.* did not observe the rock salt structure in NbN fibers until nitriding at 800 °C (and superconductivity was first observed at 1050 °C) (*17*). We attribute the ability to generate a cubic crystal structure in our mesostructured materials at lower temperatures to the porosity of the gyroidal Nb_2O_5 film and the resulting short solid-state diffusion lengths for oxygen and nitrogen atoms to reach a reactive solid-pore interface. The coherent scattering domain size, determined from a Debye-Scherrer analysis of x-ray peak widths, was found to be 7.2 nm in the 700 ºC nitride ISO-64k derived material. After further nitriding at 850 ºC, the domains grew to 9.0 nm. In the 865 ºC nitrided ISO-86k derived sample, the domain size was approximately 13.6 nm. These domain sizes are considerably smaller than the unit cell mesopore repeat, but are comparable to the pore wall diameter, consistent with structure retention upon thermal processing even at the highest temperature. The pore wall diameters were measured via SEM image analysis and found to be 9.9 nm ± 1.5 nm for the 700 ºC ISO-64k derived nitride, 10.5 nm ± 1.5 nm for the ISO-64k 850 ºC nitride, and 15.2 nm ± 3.1 nm for the ISO-86k 865 ºC nitride. High-resolution transmission electron microscopy (TEM) images of the final ISO-64k and ISO-86k-derived materials (Figures 2.S9-2.S11) confirm this observation and exhibit a (200) plane spacing of 2.2 A, comparable to the lattice parameter measured by XRD.

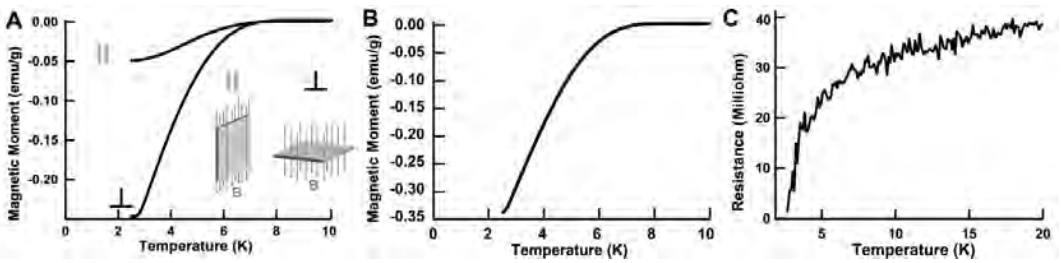

Fig. 2.4. Magnetization and electrical resistance of superconducting gyroids. (**A**) Temperature dependent magnetization from 2.5 to 10 K for ISO-64k derived NbN films in a 200 Oe applied field with film long axis either parallel (top, ||) or perpendicular (bottom, ⊥) to the applied field (see insets for different geometries tested). (**B**) Temperature dependent magnetization from 2.5 to 10 K for ISO-86k derived NbN films in 100 Oe applied field with film axis perpendicular to field. (**C**) Temperature dependent four-point electrical resistance of ISO-86k derived NbN films showing a drop beginning at approximately 7 K.

We characterized the magnetization behavior of our materials at low temperatures. The zero-field cooled temperature dependent magnetization was measured for film samples of 850 °C nitrided materials oriented with their long axis either parallel or perpendicular to the applied magnetic field (Figure 2.4A). Both geometries show a superconducting transition with a similar trend: a critical temperature, T_c, of 7.8 K and a broad transition down to 2.5 K. Nitrided samples treated to 865 °C behaved the same (Figure 2.4B). The observed T_c is below that of pure bulk NbN (16 K) (*17, 20*). Samples oriented with their long axis perpendicular to the applied magnetic field have larger demagnetization than the parallel-oriented samples, which is expected given the aspect ratio (~10) of the films. The

perpendicular-oriented sample was also temperature swept to 30 K to ensure no changes occurred between 10 K and 30 K (Figure 2.S12). Field-cooled magnetization data are comparable to the zero-field cooled data (Figure 2.S13). Additionally, the parallel-oriented sample was zero field cooled to 2.5 K and its low field dependent magnetization was measured to estimate the flux exclusion and critical current, J_c, of the material (Figure 2.S14). Interestingly, samples nitrided in single steps to only 700 °C or 850 °C did not exhibit a superconducting transition.

From the slope of the field dependent magnetization at low fields (Figure 2.S14) and using the fractional density of the material calculated from the N_2 sorption data, the flux exclusion was calculated to be 5% compared to a dense, perfect superconductor with the same outer dimensions. This suggests that the flux lines are not perfectly excluded from the perimeter of the sample and may be passing through the mesopores. The field-dependent magnetic moment exhibits changes in slope around -19.8 kOe and -33.7 kOe (Figure 2.S15). These fields correspond well to one flux quantum per pore on a ~33nm lattice and two flux quanta per pore on a ~35nm lattice, respectively. Assuming a Bean model interpretation (*21*,*22*), the subtle increases in magnetization at these fields indicate an increase in critical current due to pinning of the flux quanta. Additional SAXS experiments showed that some fractions of sample of the same batch processed under identical conditions indeed have mesoscale repeat distances of 33.0 nm (Figure 2.S16). This degree of heterogeneity is not surprising in light of the substantial shrinkage (>50% for ISO-86k) samples undergo during processing. The critical current density, J_c, was estimated as 440

A/cm^2 at 100 Oe and 2.5 K. This relatively low value (*20*) may indicate weak links such as cracks or grains of poor superconductivity through the film thickness.

The electrical conductivity and resistance of the samples were characterized by two techniques: room-temperature, two-point conductivity of a ISO-64k derived sample after the final nitridation at 850 °C and four-point temperature-dependent resistance measurements of a ISO-86k derived sample after final nitridation at 865 °C. In the two-point resistance measurement, the sample was found to have a conductivity of 4.0 S/cm at room temperature, similar to values previously measured for mesoporous mixed transition metal nitrides that were generated by nitriding oxides (*18*). In the four-point measurement, the electrical resistance of an ISO-86k derived film after all processing steps was measured as a function of temperature from 300 K to 2 K. As shown in Figure 2.4C, the material exhibited a dramatic drop in electrical resistance at approximately 7 K, consistent with the behavior expected for a superconductor and the T_c values observed in magnetometry.

As noted above, the T_c of 7-8 K for the mesoporous superconducting materials is below that of pure, bulk NbN, which is around 16 K. Non-stoichiometry, different crystal structures, oxygen content, atomic vacancies, and small feature sizes can all lower or suppress the T_c in niobium nitrides (*17, 23-28*). The experimental T_c and lattice parameters for the superconducting mesoporous networked materials studied here are consistent with values for a composition $NbN_{1-x}O_y\square_{x-y}$ (where $\square$ represents

vacancies) rather than highly stoichiometric δ-NbN (*20, 28-30*, see also Figure 2.S8). This is not surprising considering the nitride precursor is Nb_2O_5 and the relatively low nitriding temperatures employed. For the present system, the nitriding temperatures necessary for generating superconducting materials (at least 850 °C) were in the same range in which loss of long-range periodic order of the alternating gyroid mesostructure occurred. In future studies, as processing steps for block copolymer self-assembly directed mesoporous superconductors are optimized, we anticipate higher quality structural control for superconducting samples.

Conclusion

Block copolymer self-assembly is considered a hallmark of soft condensed matter physics. Due to structural versatility as well as precise tunability of morphology, dimensionality, and feature size, block copolymer self-assembly directed inorganic mesostructure formation is an ideal platform for studying periodically ordered mesostructural effects on superconducting properties. Generating such ordered mesoporous superconductors is not limited to niobium nitride nor to the particular synthetic strategy shown in this work. For example, block copolymer self-assembly could be used to tailor-make periodically ordered mesoporous superconductors *via* selective block etching and subsequent metal (*31*) or metal oxide (*32*) backfilling, or by block copolymer directed self-assembly of superconducting oxides. Periodic ordering of superconductors on the mesoscale may be expected to lead to a host of novel properties and applications. For example, pinning of superconducting vortex lines on the periodic mesostructure may be expected to lead to commensurate-incommensurate transitions with applied magnetic field intensity, to angle dependent

forces as the vortex lines align with the pore axes, and to vortex avalanches (*33-35*). The chiral nature of some mesostructured superconductors will likely only couple weakly to the underlying superconducting pairing (*36*) but may give rise to unusual bulk material properties such as nonlinear coupling to magnetic fields *(37)*. These properties may be expected to be of higher magnitude than those of chiral molecular systems since the London penetration depth (*e.g.* 39 nm for Nb and 370 nm for NbN) (*38,39*) is comparable to the chiral superstructure repeat distance. Finally, backfilling of mesopores with second material components should allow for leveraging the enormous surface areas to enhance interfacial superconductivity between non-superconducting constituents. Previously such studies have been restricted to planar interfaces between non-superconducting constituents, including metal-metal interfaces (*40*), metal-semiconductor interfaces (*41,42*), metal-insulator interfaces (*43*), semiconductor-semiconductor interfaces *(19,44)*, and insulator-insulator interfaces (*45, 46*). Mesostructured interfaces introduce topological degrees of freedom to the field of interfacial superconductivity. Obviously, much of this is speculation, as no one hitherto has ever produced a mesoporous superconducting material with a three-dimensionally continuous chiral cubic mesostructure. Moving forward, block copolymer self-assembly directed superconductors may provide a fertile area for the study of superconductivity and the effects of periodic and chiral mesostructural order on superconducting properties.

Materials and Methods

Materials. Hydrochloric acid (37 wt%, ACS/NF/FCC), niobium(V) ethoxide (99.999%, metals basis), and tetrahydrofuran (anhydrous, ≥99.9%, inhibitor-free) were all used as received. Anhydrous ammonia (99.9%, premium grade) was purified over a SAES MicroTorr MC400-702F purifier to remove residual oxygen and moisture.

Two poly(isoprene)-*block*-poly(styrene)-*block*-poly(ethylene oxide) (ISO) block copolymers were synthesized by sequential anionic polymerization using known procedures (*47, 48*). The block copolymer composition and polydispersity index (PDI) was characterized by a combination of size exclusion chromatography (GPC) and nuclear magnetic resonance (NMR). ISO-64k had an overall molar mass of 63.8 kg/mol and a PDI of 1.03. It was comprised of 18.7 kg/mol polyisoprene, 40.5 kg/mol polystyrene, and 4.6 kg/mol poly(ethylene oxide). ISO-86k had an overall molar mass of 86.2 kg/mol and a PDI of 1.09. It was comprised of 22.7 kg/mol polyisoprene, 58.7 kg/mol polystyrene, and 4.7 kg/mol poly(ethylene oxide).

Synthesis of Mesoporous Niobium Nitride. 75 mg of ISO-64k was dissolved in 2 mL anhydrous tetrahydrofuran (THF). The niobium oxide sol was prepared by a hydrolytic sol-gel route. First, 0.51 mL (2.03 mmol) of niobium(V) ethoxide was quickly added to 0.30 mL HCl in 1.00 mL of THF, and stirred vigorously in a 4 mL vial. After 5 minutes, 1.00 mL (12.3 mmol) THF was quickly added to the stirring vial. After 2 minutes, an aliquot of the transparent yellow sol was added to the polymer solution. The sol aliquot was 0.24 mL/75 mg ISO-64k to generate an alternating gyroid morphology. For the ISO-86k derived samples, a similar procedure was used with 100mg of ISO-86k dissolved in 4mL of anhydrous THF. The sol was

prepared as for the ISO-64k derived samples, with a sol aliquot of 0.31mL/100mg ISO-83k to generate an alternating gyroid morphology.

The ISO/oxide mixtures were stirred vigorously for at least 3 hours. Films were then cast in PTFE dishes. For the ISO-64k samples, the solvent was evaporated with the PTFE dish on a glass petri dish covered by a glass dome, on a hot plate set to 50 ˚C overnight. For the ISO-86k derived samples, the solvent was evaporated with the PTFE dish on a glass petri dish covered by a glass dome with continuous dry nitrogen purge, on a hot plate set to 35º C for 24-48 hours. Films were subsequently aged at 130 ˚C for 2.5 h in a vacuum oven. To remove any closed layers on the polymer/oxide hybrid films, the films were treated with a CF_4 plasma in an Oxford PlasmaLab 80+ reactive ion etcher system at 300 W for 40 minutes on each side of the film.

Films were calcined in air to generate freestanding mesoporous oxides in a flow furnace: ramped 1 ˚C/min to 450 ˚C and held for 3 hours at 450 ˚C, and allowed to cool to ambient temperature.

For nitriding the resulting oxides, films were heated in a flow furnace under anhydrous ammonia gas in two heating steps. In the first step, the oxide samples were heated under flowing ammonia gas at a flow rate of 2.5 L/h and a heating ramp rate of 350 ˚C/h to 700 ˚C, with a dwell time of 12 h at 700 ˚C. The tube was cooled to room temperature under flowing ammonia and purged with N_2. One tube valve was opened to air for 30 minutes, then the tube end was removed and the samples were removed from the tube. In the second step, samples were heated again under flowing ammonia gas at a flow rate of 2.5 L/h and a heating ramp rate of 350 ˚C/h to 850 ˚C or 865ºC, with a dwell time of 3 h at 850/865 ºC. The tube was cooled to room temperature

under flowing ammonia and purged with N_2. One tube valve was opened to air for 30 minutes, then the tube end was removed. Finally, samples were removed for characterization. The resulting freestanding mesoporous films were around 160 μm thick with lengths and widths around 5 mm.

Magnetization Characterization. Magnetization measurements were performed on a Quantum Design Physical Property Measurement System equipped with a 9T superconducting magnet (model number PPMS-9T) using the Vibrating Sample Magnetometer (VSM) setup. For samples in the perpendicular configuration to the magnetic field geometry, small flakes (lengths and widths around 1.5mm) of the mesoporous films with a mass of 1-2 mg were mounted on a fused quartz cylinder using Lakeshore IMI-7031 low temperature varnish. The quartz cylinder was then loaded into a gold-coated brass half tube holder. For samples in the parallel configuration to the magnetic field geometry, flakes were mounted on a fused quartz paddle holder using Lakeshore IMI-7031 low temperature varnish. Samples were zero field cooled to 2.5 K. When the temperature stabilized, a magnetic field of 200 Oe was applied. The samples were then heated at a rate of 0.15 K/min from 2.5 K to 10 K while measuring the magnetic moment of the samples in the 200 Oe field.

For the field cooled magnetization characterization (Figure 2.S13), the sample was cooled under an applied field of 50 Oe to a temperature of 2 K. The sample was then heated at a rate of 1 K/min from 2.5 K to 30 K while measuring the magnetic moment.

For samples measured to 30 K in the perpendicular configuration, samples were zero field cooled to 2.5 K. Then a field of 70 Oe was applied and the temperature

was swept at a rate of 0.5 K/min to 15 K, followed by 20 K/min to 300 K (only values from 2.5 to 30 K were plotted in Figure 2.S12).

The flux exclusion was calculated from the susceptibility determined from the initial slope of a field-dependent magnetization measurement performed on an ISO-64k derived nitride at 2.5 K (Figure 2.S14). The reported critical current, J_c, was calculated from the low field-dependent magnetization of an ISO-64k derived nitride using the Bean critical state model *(21)* at 2.5 K and 100 Oe. The mesoporosity of the sample was not taken into account when calculating the flux exclusion and critical current due to the lack of an appropriate model. The values reported are compared to a dense NbN solid.

For the high-field magnetization characterization, a sample of the final ISO-86k derived 865ºC nitride was mounted in a polypropylene capsule (Quantum Design) in the PPMS VSM and cooled to 2.5K. A field of 100Oe was applied to locate the sample, then the magnetic moment was measured as a function of applied field during a sweep at 10 Oe/s first from 0 to 50kOe, then from 50 to -50kOe, and finally from -50 to 0 kOe. The points of slope change reported were determined from the intersection points of linear fits to the data, as shown in figure 2.S15.

XRD Characterization. Powder X-ray diffraction (XRD) data for the oxide and nitrides were collected on a Rigaku Ultima IV diffractometer equipped with a D/teX Ultra detector, using CuK_α radiation and a scan rate of 2 °/min. Lattice parameters of the NbN samples were calculated from $2*d_{200}$ ($2\theta \approx 42°$). Crystallite sizes reported are the lower limit of the coherent scattering domain size as determined from a Debye-Scherrer analysis of all five peaks between 30 and 80 degrees. Instrumental and other

sources of peak broadening were not accounted for in this analysis, but are not expected to have a significant effect given the small size of the coherent scattering domains observed.

SAXS Characterization. Small angle X-ray scattering (SAXS) patterns were obtained on either a home-built beamline equipped with a Rigaku RU-3HR copper rotating anode generator, a set of orthogonal Franks focusing mirrors and a phosphor-coupled CCD detector, as described in detail elsewhere (*49*) or at the G1 station of the Cornell High Energy Synchrotron Source (CHESS) with a typical beam energy of 10.5 keV and sample-to-detector distance of 2.6 m or more. The two-dimensional patterns obtained from a point-collimated beam were azimuthally integrated using the Nika software package *(50)* to yield the one-dimensional plots shown in Figure 2.2. The ISO-64k oxide pattern (Figure 2.S2) and ISO-86k nitride pattern (Figure 2.S16) were collected at CHESS while all other patterns were collected on the home-built beamline. The ISO-86k data exhibited significant orientation of the mesostructure and were integrated azimuthally over a selected angular range of 197-331º for the hybrid, 57.5º-92.5º for the 700ºC nitride, and 88.5º-103.5º for the 865ºC nitride. The two-dimensional data are shown in Figure 2.S3.

SEM Characterization. Fractured and powdered monoliths samples were directly mounted on stubs using carbon tape. Oxide samples were coated with Au-Pd to increase conductivity while nitride samples required no coating. The samples were characterized by scanning-electron microscopy (SEM) on a TESCAN MIRA3 LM FE-SEM instrument and a Zeiss LEO-1550 FE-SEM equipped with in-lens detectors. Pore wall thickness was measured using ImageJ software, taking the average of 100

measurements on each image. Reported uncertainties in pore wall thickness are the standard deviation of the same set of 100 measurements. Fourier transforms shown in figures 2.S5-2.S6 were calculated using ImageJ.

TEM Characterization. Powdered monoliths after final heat treatment were drop cast from isopropyl alcohol on carbon coated copper TEM grids (Electron Microscopy Sciences, Inc.). The samples were imaged by standard transmission electron microscopy on an FEI Tecnai T12 with an accelerating voltage of 120kV. High resolution transmission electron microscopy (HR-TEM) images were acquired on a FEI Tecnai F20 with an accelerating voltage of 200kV. Lattice parameters were determined by Fourier transforms of HR-TEM images.

Low Temperature Conductivity Characterization. After all heat treatments, a piece of the ISO-86k derived nitride was used for a four point resistance measurement. Contacts were made on the sample using Epo-Tek H20E silver-filled epoxy and connected via a carrier chip to a Quantum Design Physical Property Measurement System (PPMS) resistivity puck (Figure 2.S17). The carrier chip was used to mechanically isolate the sample to prevent cracking during cooling. It consists of four sputtered gold contact pads on a 100nm thermal oxide layer atop a (100) silicon substrate. The sample was electrically connected to the pads using Epo-Tek H20E and the pads were then wire-bonded to the PPMS contacts. The excitation current was 25 microamps. Because of the sample's mesoporosity, the cross-sectional area was not estimated and the values reported are resistance, not resistivity.

Room Temperature Conductivity Characterization. After all heat treatments a piece of a nitride was used for a two point conductivity measurement. A portion of the

sample's top surface was masked and Au-Pd coated to generate contacts. The mask was removed and drops of In-Ga liquid metal eutectic were placed on the Au-Pd contacts. Resistance was measured across the known cross-section of the sample and was used to calculated conductivity. Mesoporosity was not taken into account in the conductivity calculations, which provide a lower bound for the conductivity of the sample.

N_2 Sorption Characterization N_2 sorption characterization was performed on a Micromeritics ASAP 2020 surface area and porosity analyzer at -196 °C. The powdered samples were degassed at 120 °C under vacuum for at least 6 h prior to measurements. Surface areas were determined using the Brunauer-Emmett-Teller (BET) method (*51*) and pore size distributions were calculated employing the Barrett-Joyner-Halenda (BJH) method (*52*).

Acknowledgements

H.S. was supported by the National Science Foundation (NSF) Single Investigator Award (DMR-1104773). P.A.B. was supported by the NSF Graduate Research Fellowship Program (DGE-1144153). J.P.S. was supported by NSF DMR-1312160. This work was supported as part of the Energy Materials Center at Cornell (EMC2), an Energy Frontier Research Center funded by the U.S. Department of Energy, Office of Science, Basic Energy Sciences (DOE) under Award # DE-SC0001086. This work made use of the Cornell Center for Materials Research Shared Facilities, which are supported through the NSF MRSEC program (DMR-1120296); the Cornell High

Energy Synchrotron Source (CHESS), which is supported by the NSF and the National Institutes of Health/National Institute of General Medical Sciences under NSF award DMR-0936384; the Cornell NanoScale Facility, a member of the National Nanotechnology Infrastructure Network, which is supported by the NSF (ECCS-15420819) and the x-ray detector laboratory of S.M.G., which is supported by DOE grant DE-FG02-11ER16210. The authors thank Robert T. Bell for advice and assistance with fabrication of conductivity measurement substrates.

Coauthor Contributions

U.W. and S.M.G. conceived the idea and J.P.S. helped identify the nitride as the material of interest. S.W.R., R.B.V., and U.W. came up with the experimental design. S.W.R. and P.A.B. synthesized the samples and performed the room temperature conductivity, magnetization, and XRD measurements. P.A.B. performed the low-temperature conductivity and high field magnetization measurements. S.W.R. performed the N_2 sorption measurements. H.S., P.A.B., and S.M.G. measured and analyzed the SAXS data. K.W.T. conducted SEM characterization. J.G.W. conducted TEM characterization. F.J.D. supervised and analyzed the XRD experiments. R.B.V. supervised and analyzed the magnetization and conductivity experiments. S.W.R., P.A.B., and U.W. wrote the paper with help from F.J.D., S.M.G., and J.P.S.. All authors commented on the manuscript. U.W. supervised the project.

REFERENCES

1. R. Córdoba *et al.*, Magnetic field-induced dissipation-free state in superconducting nanostructures. *Nat. Commun.* **4**, 1437 (2013).
2. L. Piraux, X. Hallet, Artificial vortex pinning arrays in superconducting films deposited on highly ordered anodic alumina templates. *Nanotechnology* **23**, 355301 (2012).
3. U. Welp *et al.*, Superconducting transition and vortex pinning in Nb films patterned with nanoscale hole arrays. *Phys. Rev. B* **66**, 212507 (2002).
4. J. Vanacken *et al.*, Vortex pinning in superconductors laterally modulated by nanoscale self-assembled arrays. *Physica C* **468**, 585 (2008).
5. A. Lungu *et al.*, Superconductivity in nanostructured lead. *Physica C* **349**, 1 (2001).
6. Y. J. Hsu, S. Y. Lu, Y. F. Lin, Nanostructures of Sn and their enhanced, shape-dependent superconducting properties. *Small* **2**, 268 (2006).
7. U.S. Department of Energy Basic Energy Sciences, "From Quanta to the Continuum: Opportunities for Mesoscale Science" (2012, http://www.meso2012.com).
8. E.-S. Jang *et al.*, Asymmetric High-T_c Superconducting Gas Separation Membrane. *Chem. Mater.* **19**, 3840 (2007).
9. C. Cirillo *et al.*, Quantum phase slips in superconducting Nb nanowire networks deposited on self-assembled Si templates. *Appl. Phys. Lett.* **101**, 172601 (2012).

10. Y. Tsuchiya *et al.***,** Flux avalenches in Nb superconductng shifted strip arrays. *Supercond. Sci. Technol.* 26 095004 (2013).

11. E. Culverwell, S.C. Wimbush, S.R. Hall, Biotemplated synthesis of an ordered macroporous superconductor with high critical current density using a cuttlebone template. *Chem. Comm.* **2008**, 9 1055 (2008).

12. B. Smarsly, M. Antonietti, Block Copolymer Assemblies as Templates for the Generation of Mesoporous Inorganic Materials and Crystalline Films. *Eur. J. Inorg. Chem.* **2006**, 1111 (2006).

13. M. C. Orilall, U. Wiesner, Block copolymer based composition and morphology control in nanostructured hybrid materials for energy conversion and storage: solar cells, batteries, and fuel cells. *Chem. Soc. Rev.* **40**, 520 (2011).

14. L. Ruiz-Valdepeñas *et al.*, Imprinted labyrinths and percolation in Nd-Co/Nb magnetic/superconducting hybrids. *J. Appl. Phys.* **115**, 213901 (2014).

15. M. Templin *et al.*, Organically Modified Aluminosilicate Mesostructures from Block Copolymer Phases. *Science* **278**, 1795 (1997).

16. A. J. Meuler, M. A. Hillmyer, F. S. Bates, Ordered Network Mesostructures in Block Polymer Materials. *Macromolecules* **42**, 7221 (2009).

17. K. Nomura, Y. Takasuka, K. Kamiya, H. Nasu, Preparation of NbN fibres by nitridation of sol-gel derived Nb_2O_5 fibres. *J. Mater. Sci.: Mater. Electron.* **5**, 53 (1994).

18. S. W. Robbins, H. Sai, F. J. DiSalvo, S. M. Gruner, U. Wiesner, Monolithic gyroidal mesoporous mixed titanium-niobium nitrides. *ACS Nano* **8**, 8217 (2014).

19. K. Murase *et al.*, Superconducting behavior in PbTe-SnTe superlattices. *Surf. Sci.* **170**, 486 (1986).

20. W. Martienssen, H. Warlimont, *Springer Handbook of Condensed Matter and Materials Data*. (Springer, 2006).

21. C. P. Bean, Magnetization of Hard Superconductors. *Phys. Rev. Lett.* **8**, 250 (1962).

22. C. P. Bean, Magnetization of High-Field Superconductors. *Rev. Mod. Phys.* **36**, 31 (1964).

23. E. K. Storms, A. L. Giorgi, E. G. Szklarz, Atom vacancies and their effects on the properties of NbN containing Carbon, Oxygen or Boron—II: Superconducting transition temperature. *J. Phys. Chem. Solids* **36**, 689 (1975).

24. W. Lengauer, Characterization of nitrogen distribution profiles in fcc transition metal nitrides by means of T_c measurements. *Surf. Interface Anal.* **15**, 377 (1990).

25. J. R. Gavaler, M. A. Janocko, J. K. Hulm, C. K. Jones, Superconducting properties as a function of thickness in NbN films. *Physica* **55**, 585 (1971).

26. L. Kang *et al.*, Suppression of superconductivity in epitaxial NbN ultrathin films. *J. Appl. Phys.* **109**, 033908 (2011).

27. U. Patel *et al.*, Synthesis and superconducting properties of niobium nitride nanowires and nanoribbons. *Appl. Phys. Lett.* **91**, 162508 (2007).

28. G. i. Oya, Y. Onodera, Transition temperatures and crystal structures of single-crystal and polycrystalline NbN_x films. *J. Appl. Phys.* **45**, 1389 (1974).

29. N. Terao, New phases of niobium nitride. *J. Less Common Met.* **23**, 159 (1971).

30. G. Brauer, Nitrides, carbonitrides and oxynitrides of niobium. *J. Less Common Met.* **2**, 131 (1960).

31. V. N. Urade, T.-C. Wei, M. P. Tate, J. D. Kowalski, H. W. Hillhouse, Nanofabrication of Double-Gyroid Thin Films. *Chem. Mater.* **19**, 768 (2007).

32. E. J. W. Crossland *et al.*, A Bicontinuous Double Gyroid Hybrid Solar Cell. *Nano Lett.* **9**, 2807 (2008).

33. R. A. Webb, R. F. Voss, G. Grinstein, P. M. Horn, Magnetic Field Behavior of a Josephson-Junction Array: Two-Dimensional Flux Transport on a Periodic Substrate. *Phys. Rev. Lett.* **51**, 690 (1983).

34. K. Harada, et al.**,** Direct observation of vortex dynamics in superconducting films with regular arrays of defects. *Science* **274** 5290 (1996).

35. L. Civale et al.**,** Vortex confinement by columnar defects in YBa2Cu3O7 crystals: Enhanced pinning at high fields and temperatures. *Phys. Rev. Lett.* **67** 648 (1991).

36. X.-L. Qi, T. L. Hughes, S. Raghu, S.-C. Zhang, Time-Reversal-Invariant Topological Superconductors and Superfluids in Two and Three Dimensions. *Phys. Rev. Lett.* **102**, 187001 (2009).

37. M. Kauranen, J. J. Maki, T. Verbiest, S.V. Elshocht, A. Persoons**,** Quantitative determination of electric and magnetic second-order susceptibility tensors of chiral surfaces. *Phys. Rev. B* **55** R1985 (1997).

38. B.W. Maxfield, W.L. McLean, Superconducting penetration depth of niobium. *Phys. Rev.* **139**, A1515 (1965).

39. D. E. Oates *et al.*, Surface-impedance measurements of superconducting NbN films. *Phys. Rev. B* 43, 7655 (1991).

40. M. B. Brodsky, Superconductivity in an Ag-Pd-Ag epitaxial metal film sandwich. *Phys. Rev. B* 25, 6060 (1982).

41. M. J. Burns, J. R. Lince, R. S. Williams, P. M. Chaikin, Electron localization and superconductivity in very thin epitaxially grown Ag films on Ge (001). *Solid State Commun.* 51, 865 (1984).

42. R. Akihama, Y. Okamoto, Superconductivity in Au(10Å)/Ge(13Å) alternating ultra-thin layered films. *Solid State Commun.* 53, 655 (1985).

43. A. Gozar *et al.*, High-temperature interface superconductivity between metallic and insulating copper oxides. *Nature* 455, 782 (2008).

44. N. Y. Fogel *et al.*, Direct evidence for interfacial superconductivity in two-layer semiconducting heterostructures. *Phys. Rev. B* 73, 161306 (2006).

45. N. Reyren *et al.*, Superconducting Interfaces Between Insulating Oxides. *Science* 317, 1196 (2007).

46. J. Mannhart, D. G. Schlom, Oxide Interfaces—An Opportunity for Electronics. *Science* 327, 1607 (2010).

47. J. Allgaier, A. Poppe, L. Willner, D. Richter, Synthesis and Characterization of Poly[1,4-isoprene-*b*-(ethylene oxide)] and Poly[ethylene-*co*-propylene-*b*-(ethylene oxide)] Block Copolymers. *Macromolecules* 30, 1582 (1997).

48. S. Warren, F. J. DiSalvo, U. Wiesner, Nanoparticle-tuned assembly and disassembly of mesostructured silica hybrid. *Nat. Mater.* **6**, 248 (2007).

49. A. C. Finnefrock, R. Ulrich, G. E. S. Toombes, S. M. Gruner, U. Wiesner, The Plumber's Nightmare:1 A New Morphology in Block Copolymer−Ceramic Nanocomposites and Mesoporous Aluminosilicates. *J. Am. Chem. Soc.* **125**, 13084 (2003).

50. J. Ilavsky, Nika – software for 2D data reduction. *J. Appl. Cryst.* **45**, 324 (2012).

51. S. Brunauer, P. H. Emmett, E. Teller, Adsorption of Gases in Multimolecular Layers. *J. Am. Chem. Soc.* **60**, 309 (1938).

52. E. P. Barrett, L. G. Joyner, P. P. Halenda, The Determination of Pore Volume and Area Distributions in Porous Substances. I. Computations from Nitrogen Isotherms. *J. Am. Chem. Soc.* **73**, 373 (1951).

APPENDIX: SUPPLEMENTARY MATERIALS

Additional Figures

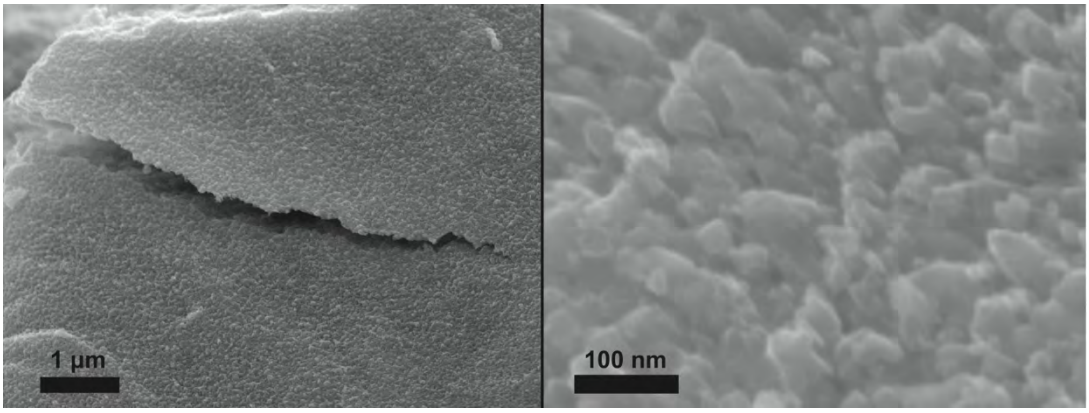

Figure 2.S1. Cross-sectional SEM images of ISO-64K derived material nitrided in one step at 1050 °C. The ordered mesoporosity is lost as the structure collapses under the high temperature nitriding conditions.

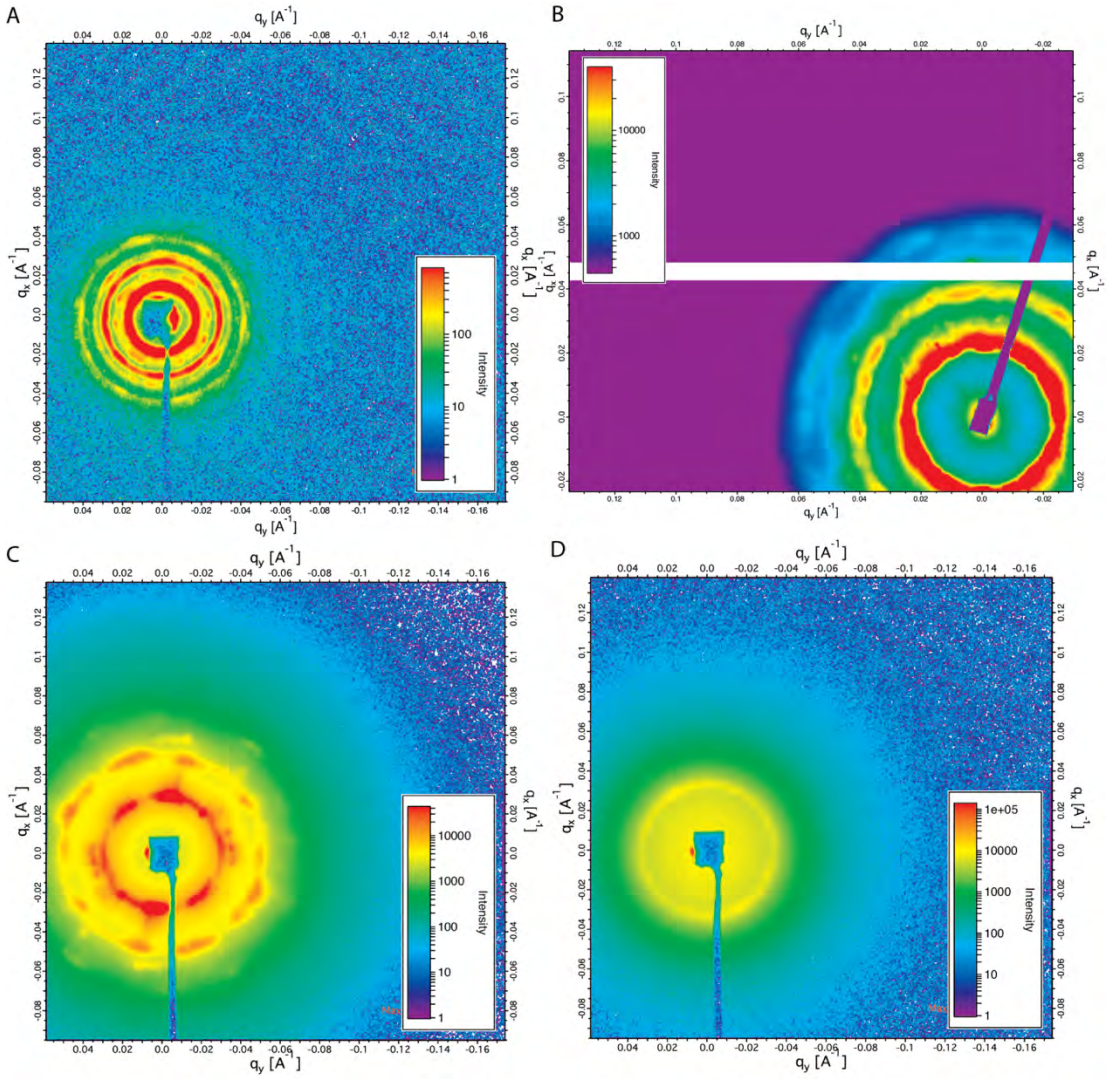

Figure 2.S2. Two-dimensional SAXS patterns of ISO-64k derived samples at various processing stages. (A) ISO-64k-Nb_2O_5 hybrid, (B) mesoporous Nb_2O_5 after calcination at 450ºC, (C) NbN nitrided at 700ºC, and (D) NbN nitrided at 850ºC. A different x-ray detector with a central gap was used for (B). Only (D) shows a smooth powder-pattern like ring. All other panels show spot-like peaks indicative of long-range ordering of the mesostructure.

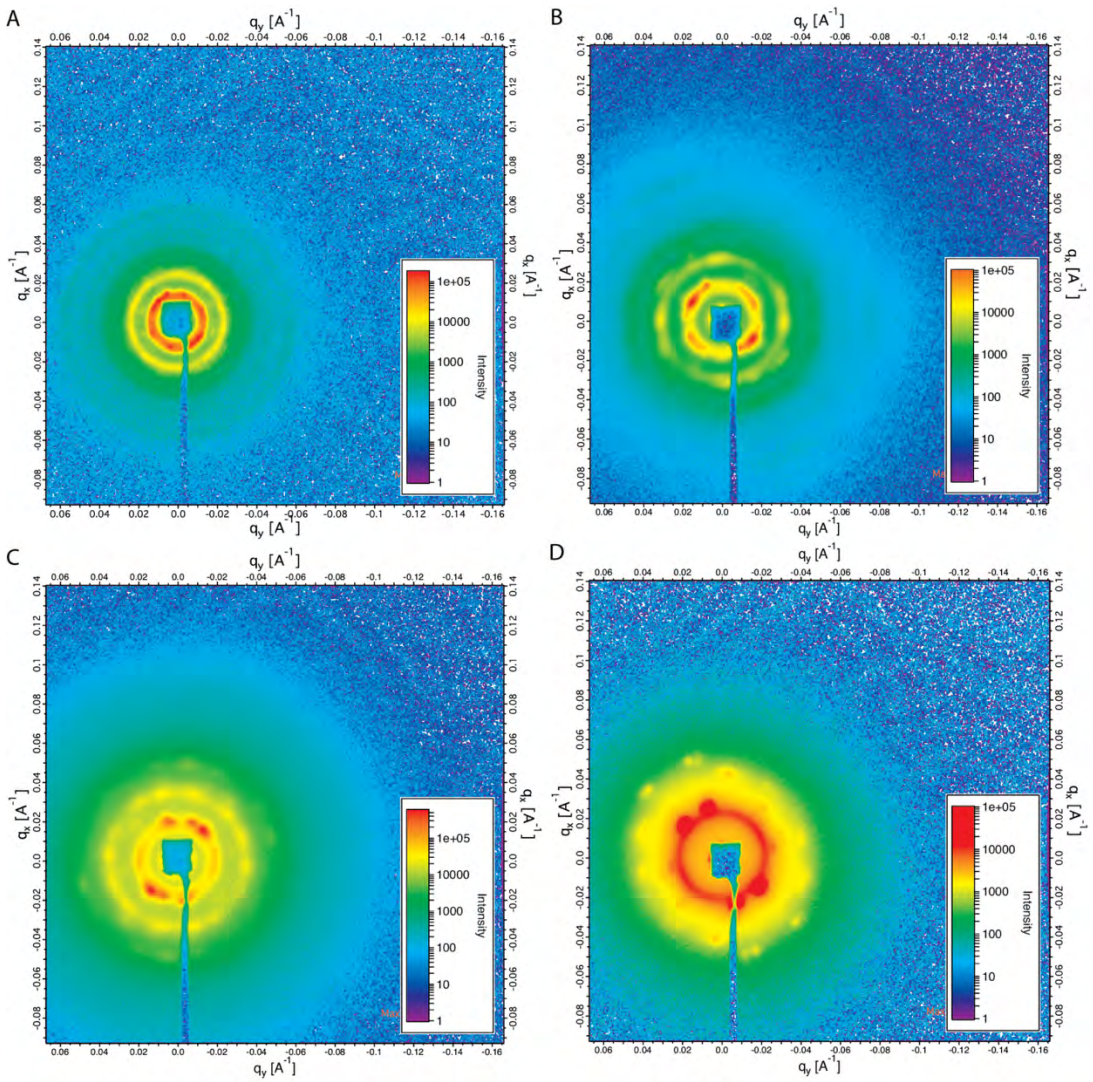

Figure 2.S3. Two-dimensional SAXS patterns of ISO-86k derived samples at various processing stages. (A) ISO-86k-Nb_2O_5 hybrid, (B) mesoporous Nb_2O_5 after calcination at 450ºC, (C) NbN nitrided at 700ºC, and (D) NbN nitrided at 865ºC. All patterns exhibit significant orientation and asymmetric compression of the mesostructure indicated by spots of increased intensity that fall on elliptical, rather than circular rings.

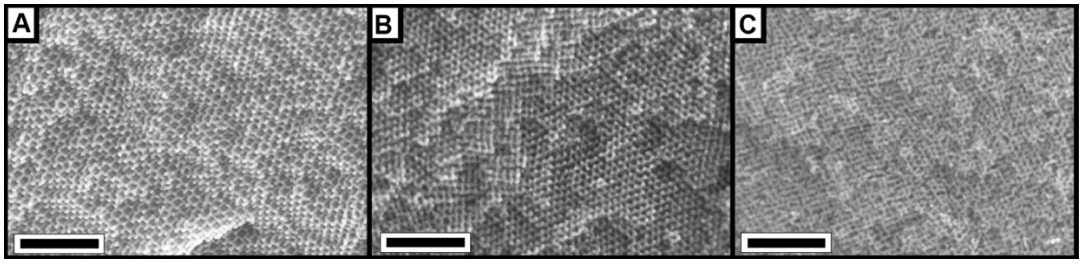

Figure 2.S4. **SEM images of ISO-64k derived mesoporous samples at different processing stages.** Periodically ordered gyroidal Nb_2O_5 (A) after calcination at 450 °C in air; Periodically ordered gyroidal NbN after nitriding at 700 °C (B) and after nitriding at 850 °C (C). All scalebars are 250 nm.

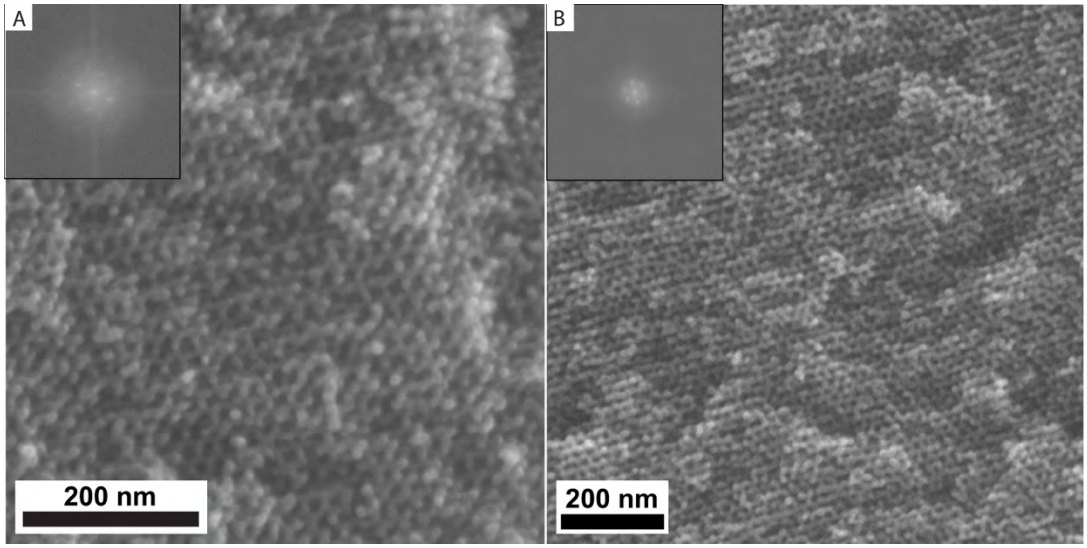

Figure 2.S5. Cross-sectional SEM images of an ISO-64k derived monolith after final 850 °C nitriding. The insets are FFTs of large square portions of the images. (A) shows a four-fold pattern consistent with the projection of the cubic alternating gyroid *($I4_132$)* along [100], while (B) shows a six-fold pattern consistent with the projection along [111].

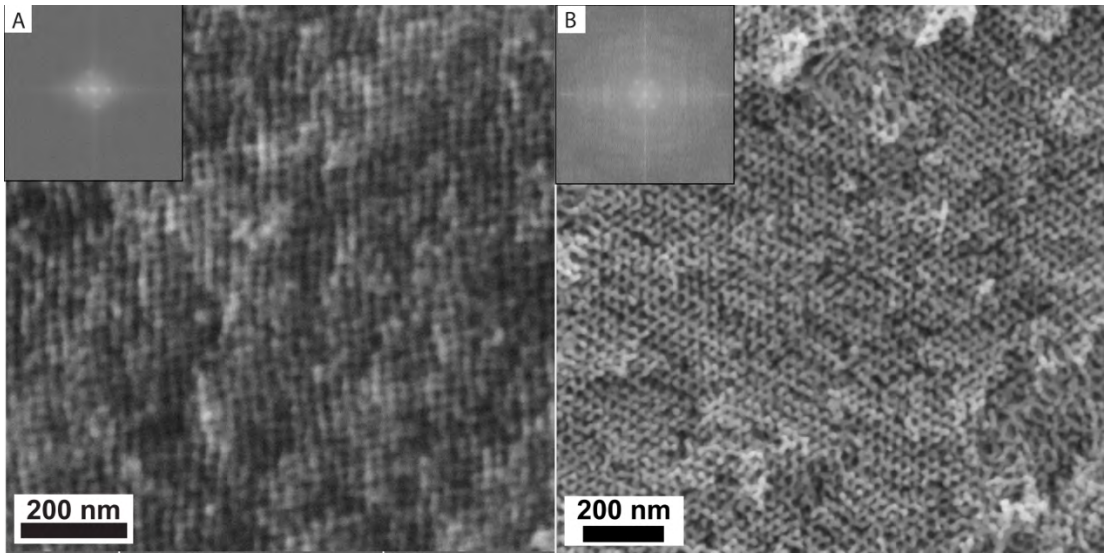

Figure 2.S6. Cross-sectional SEM images of an ISO-86k derived monolith after final 865ºC nitriding. The insets are FFTs of large square portions of the images. (A) shows a four-fold pattern consistent with the projection of the cubic alternating gyroid *($I4_132$)* along [100], while (B) shows a six-fold pattern consistent with the projection along [111].

Table 2.S1. Surface area and pore volume, as measured by N_2 sorption, of ISO-64K derived materials at different stages of thermal processing.

Sample	Surface Area (m^2/g)	Pore Volume (cm^3/g)
450 °C Calcined	111	1.01
700 °C Nitrided	86	0.71
850 °C Nitrided	59	0.41

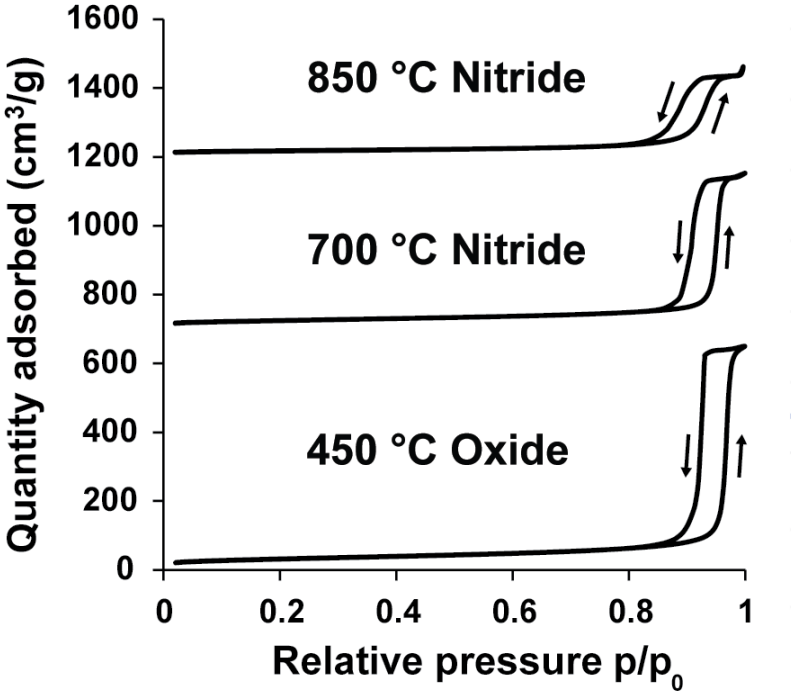

Figure 2.S7. N_2 adsorption/desorption isotherms for ISO-64k derived 450ºC calcined, 700ºC nitride, and 850ºC nitride powder samples. For visibility, the isotherms of the 700ºC and 850ºC derived nitrides are offset by 700 $cm^3\ g^{-1}$ and 1200 $cm^3\ g^{-1}$ along the *y*-axis, respectively.

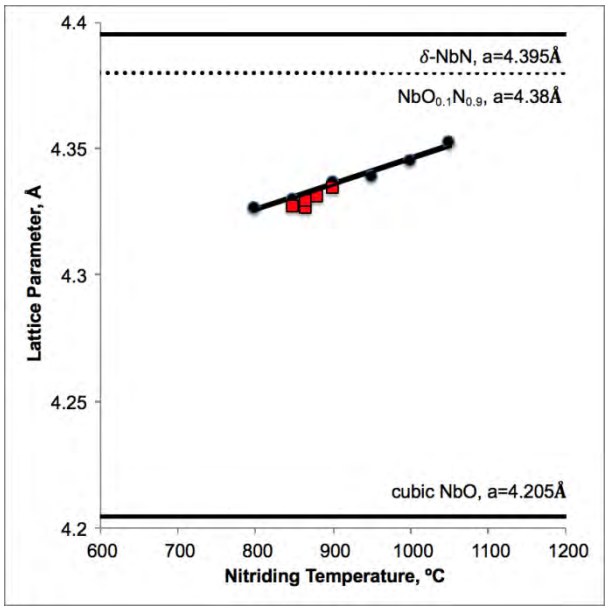

Figure 2.S8. XRD-derived lattice spacing as a function of nitriding temperature for NbN fibers (*17*, black circles and fit) and our materials (red squares). Reference lines are shown for the lattice parameters of cubic NbO, δ-$NbN_{0.9}O_{0.1}$, and δ-NbN (*17*). Assuming Vegard's law holds between the NbO and NbN, the measured lattice parameters indicate that the composition of our materials is approximately $NbO_{0.3}N_{0.7}$.

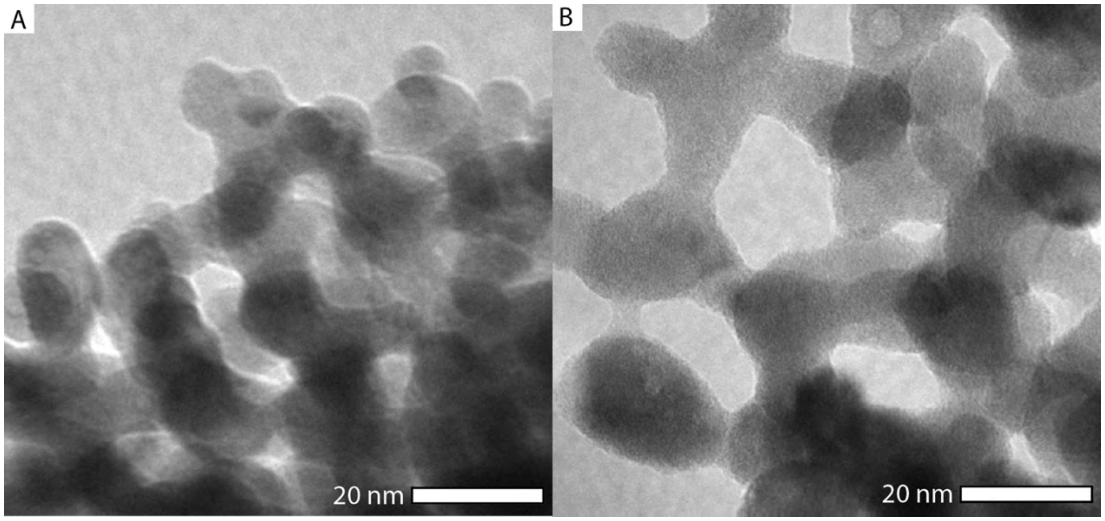

Figure 2.S9. TEM micrographs of nitrides derived from (A) ISO-64k and (B) ISO-86k after final heat treatments. The pore structure and spacing are consistent with results from SEM and SAXS measurements.

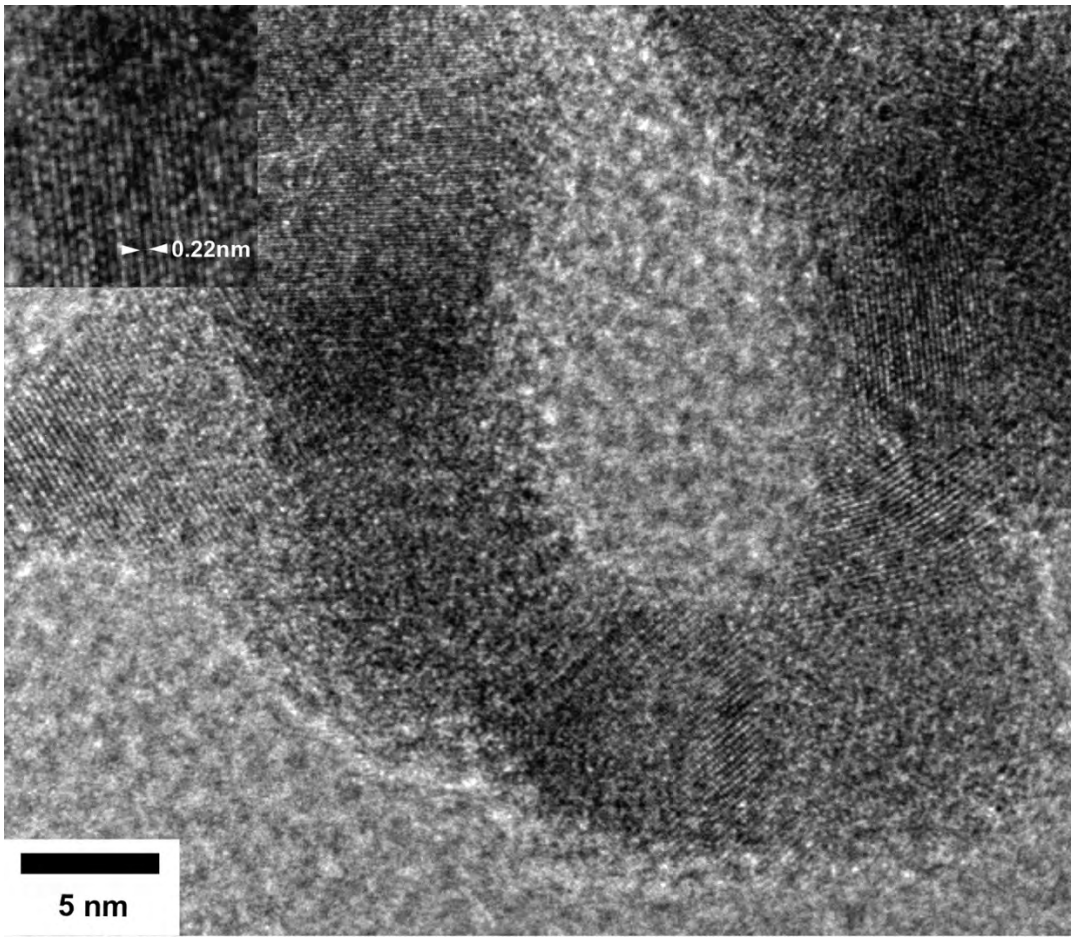

Figure 2.S10. High-resolution TEM micrograph of ISO-64k-derived nitride after final heat treatment. The observed crystallite sizes are consistent with our Debye-Scherrer analysis (see main text). The inset is an expanded view of a single crystallite showing an FFT-derived (200) plane spacing of 0.22 nm, consistent with a NbN lattice

parameter of 0.44 nm, which in turn is comparable to the lattice parameter determined by XRD (see main text).

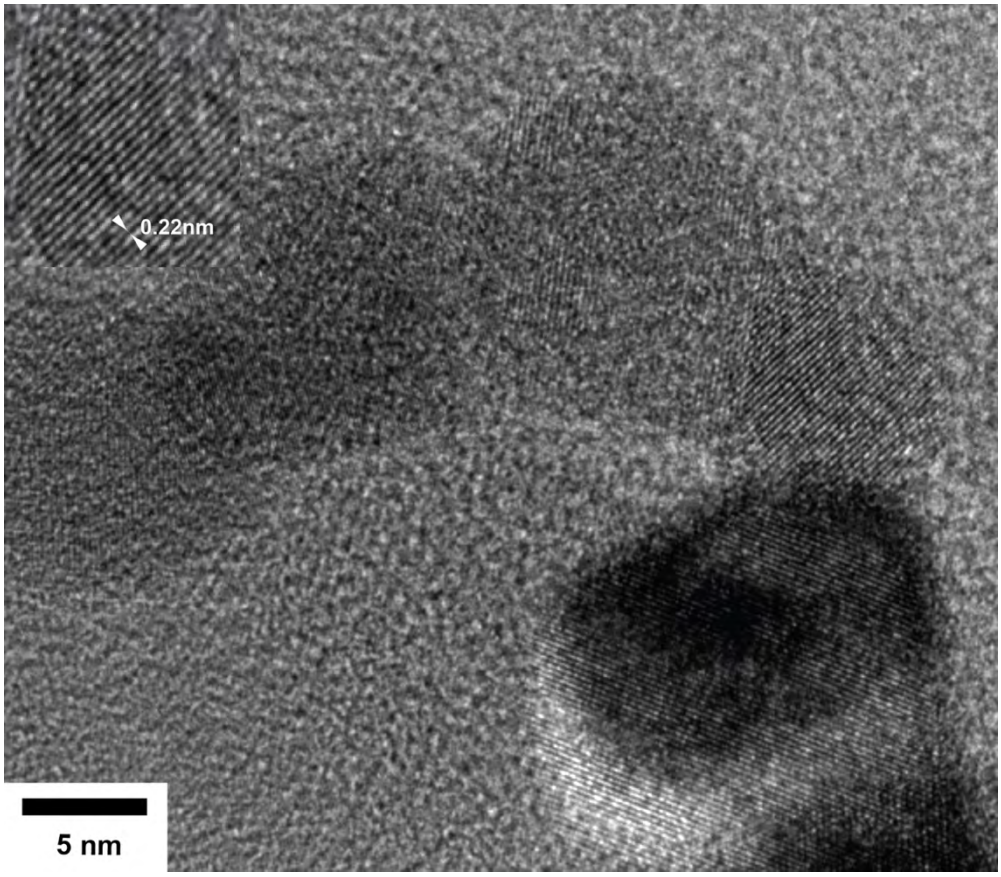

Figure 2.S11. High-resolution TEM micrograph of ISO-86k-derived nitride after final heat treatment. The observed crystallite sizes are consistent with our Debye-Scherrer analysis. The inset is an expanded view of a single crystallite showing an FFT-derived (200) plane spacing of 0.22 nm, consistent with a NbN lattice parameter of 0.44 nm, which in turn is comparable to the lattice parameters determined by XRD (see main text).

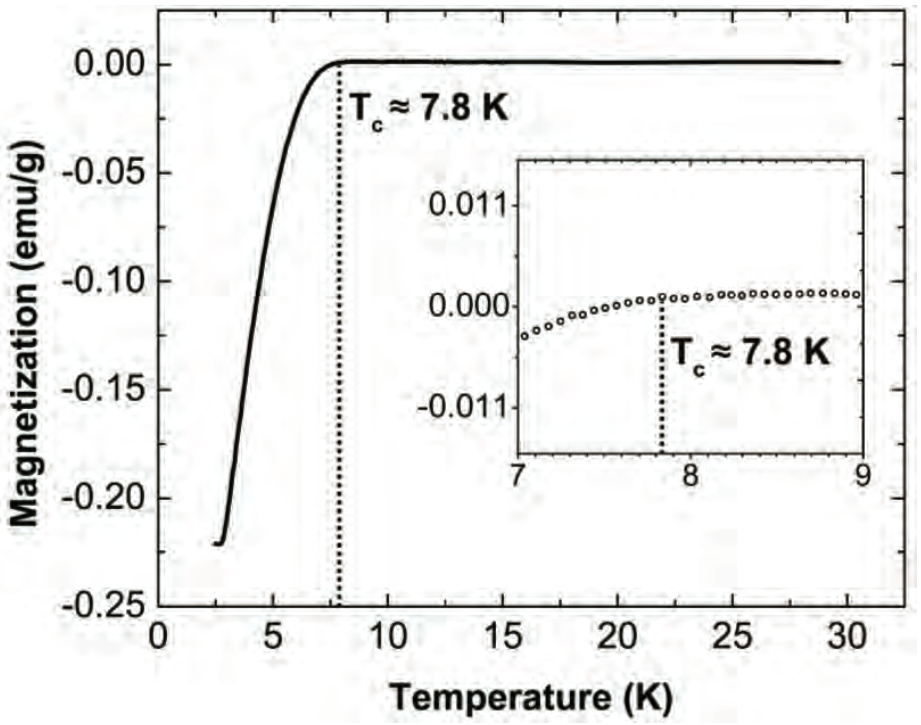

Figure 2.S12. Magnetization behavior of ISO-64k derived 850ºC gyroidal NbN material from 2.5K to 30K, measured in a perpendicular orientation with applied field of 70 Oe. The inset highlights the region between 7K and 9K where the T_c is located.

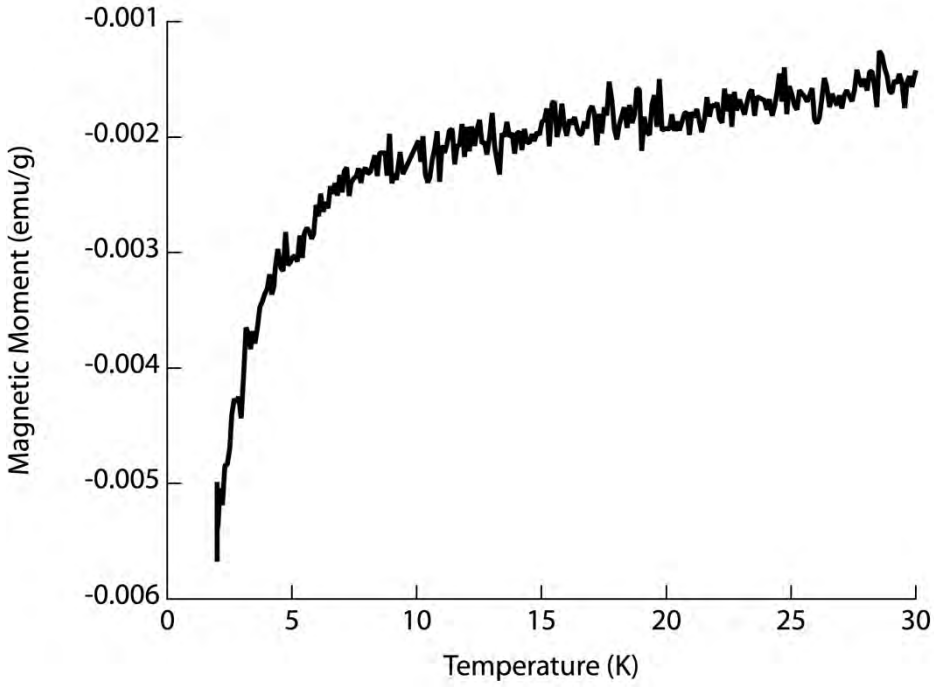

Figure 2.S13. Field-cooled magnetization behavior of ISO-86k derived 865ºC gyroidal NbN material from 2K to 30K, measured in a perpendicular orientation with applied field of 50 Oe. The field cooled data corroborate the zero field cooled data, showing a T_c of approximately 8 K and a broad transition down to 2 K.

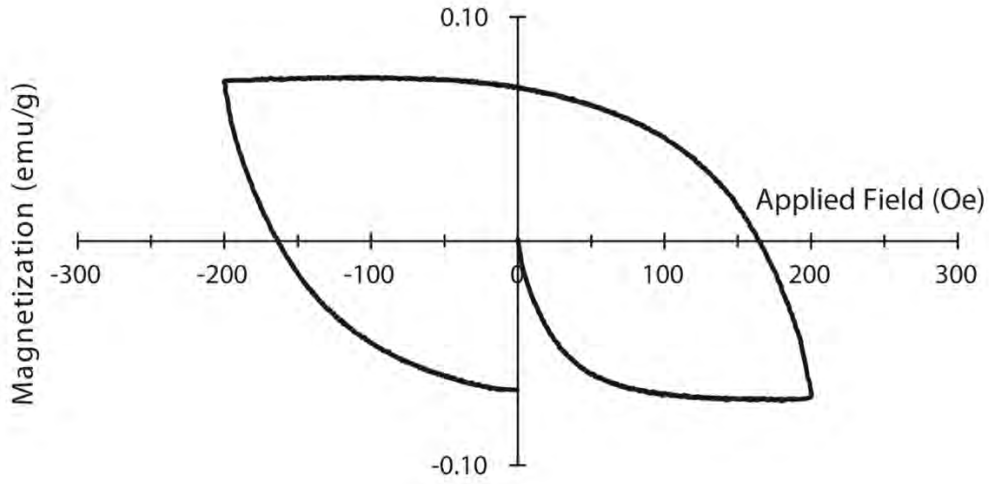

Figure 2.S14. Field sweeping magnetization behavior at 2.5K of ISO-64k derived NbN material heat treated to 850°C. The field was swept from 0 Oe to 200 Oe, then

from 200 Oe to -200 Oe and finally from -200 Oe to 0 Oe. The linear region at low fields was used to calculate the flux exclusion and the ΔM at 100 Oe was used to calculate J_c.

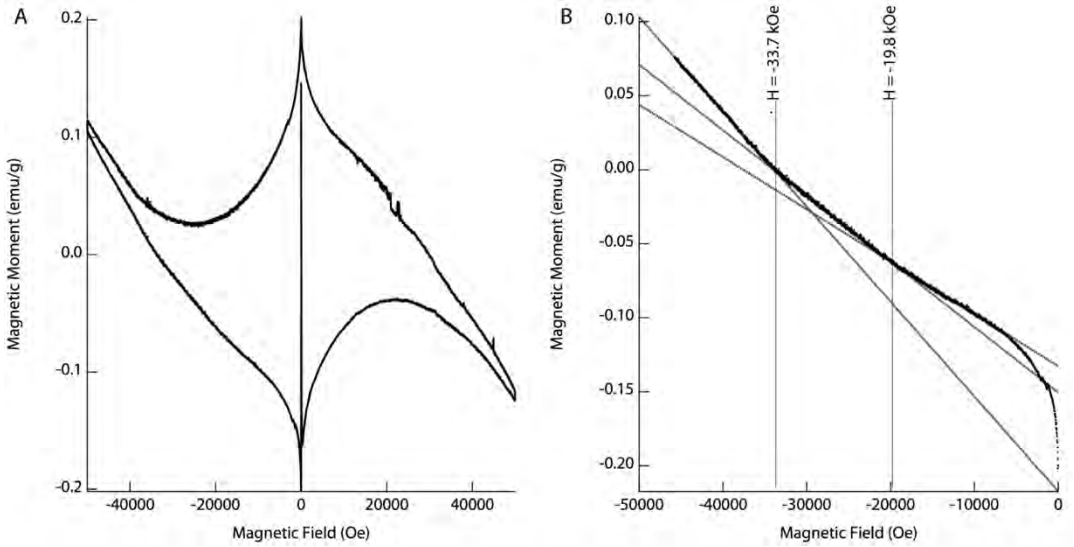

Figure 2.S15. High-field magnetization behavior at 2.5K of ISO-86k derived NbN material heat treated to 865ºC. The field was swept from 0 kOe to 50kOe, then from 50kOe to -50kOe, and finally from -50kOe to 0kOe, as shown in (A). The behavior during the final sweep (B) exhibits changes in slope around 19.8 kOe and 33.7kOe, consistent with interactions of the field with the periodic mesostructure of the sample. Specifically, a field of 19.8kOe corresponds to one flux quantum per pore on a ~33nm lattice and 33.7kOe corresponds to two flux quanta per pore on a ~35nm lattice. Assuming a Bean model interpretation, the subtle increases in magnetization at these fields indicate an increase in critical current due to pinning of the flux quanta.

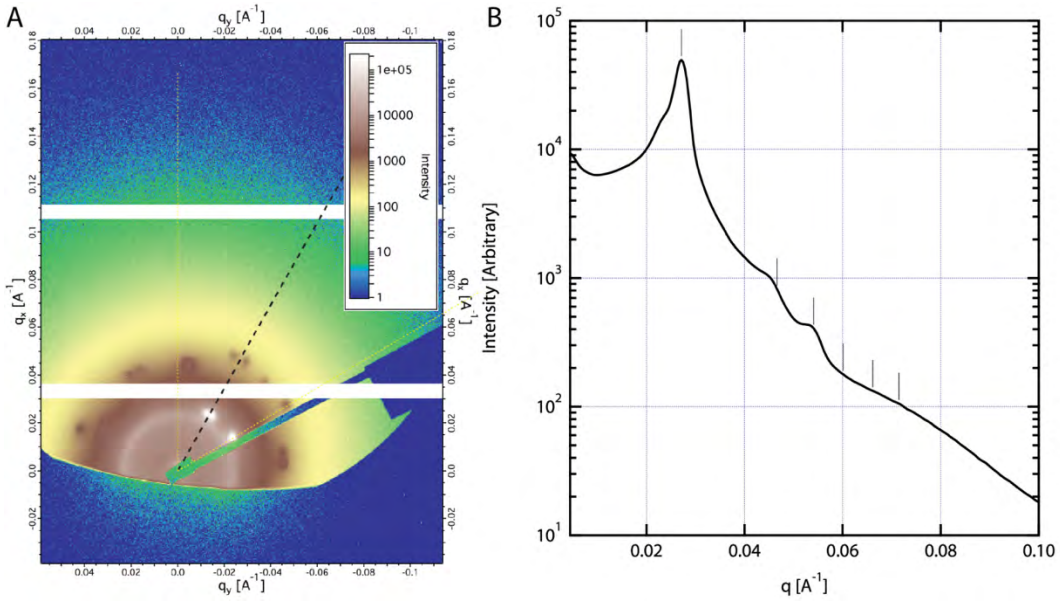

Figure 2.S16. Two-dimensional (A) and integrated (B) SAXS patterns of ISO-86k derived material processed in the same batch as that in Figure 2.S3. Tick markings in (B) are expected reflections for an alternating gyroid with d_{100} = 33.0 nm, a shift of 2.7 nm relative to the measurement shown in Figure 2.S3. The two-dimensional data were integrated over azimuthal angles from 30-90º, indicated by the yellow lines in (A), due to the substantial orientation of the mesostructure.

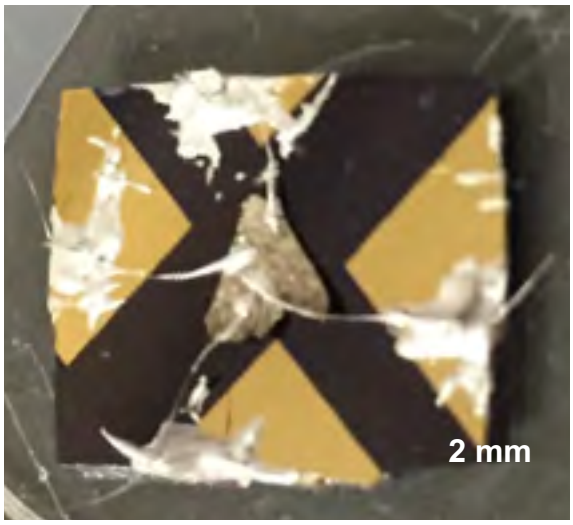

Figure 2.S17. Photograph of the four-point conductivity measurement apparatus. The sample is contacted with Epo-tek H20E epoxy and rests on a carrier chip fabricated from thermal oxide on silicon (100).

CHAPTER 3

DISCOVERING SYNTHESIS ROUTES TO ORDERED MESOPOROUS NIOBIUM NITRIDES USING POLOXAMER/PLURONICS BLOCK COPOLYMERS[2]

Abstract

Ordered mesoporous transition metal nitrides are interesting as high-surface-area catalyst supports, as materials for energy conversion and storage devices, and as a platform for investigating mesostructured superconductors. The Pluronics/poloxamer family of ABA triblock copolymers has been widely used to produce crystalline ordered mesoporous transition metal oxides, but is considered to pose a major challenge in the synthesis of the corresponding nitrides and other classes of inorganic materials. We report a synthesis of hexagonally-ordered mesoporous niobium nitrides based on commercially available ABA triblock copolymers of the poloxamer/Pluronics family. Employing *in situ* small- and wide-angle synchrotron x-ray scattering (SAXS/WAXS), we demonstrate that successful thermal processing conditions are confined to a narrow parameter window, which explains previous challenges to access such nitrides. These studies further suggest synthesis of high quality nitrides via *e.g.* rapid thermal processing. We anticipate that these routes will open the door to wider exploration of the impacts of mesostructural order on the properties and applications of transition metal nitrides.

[2] Peter A. Beaucage, Ethan M. Susca, Sol M. Gruner, Ulrich Wiesner *Chemistry of Materials* **29** (2017).

Introduction

Transition metal nitrides such as niobium nitride have been the subject of increasing scientific and technological interest in areas as diverse as supports for electrochemical catalysts(*1*), energy storage devices(*2*), and high critical field superconductors(*3*). In such applications, ordered mesoscale porosity has been shown to have a beneficial effect on material performance, *e.g.* by increasing the surface area for a catalyst support(*4*), by improving the performance of lithium-air batteries(*5*), or by enabling studies of emergent properties such as flux pinning and angle-dependent magnetoelectric coupling in superconductors(*6*). Block copolymer-inorganic hybrid co-assembly(*7*, *8*) is a reproducible, convenient, and tunable route to produce such ordered mesoporous structures in a wide variety of functional materials, ranging from highly crystalline transition metal oxides(*9*, *10*) to single-crystal silicon nanostructures(*11*). However, only a handful of studies to date have examined the use of block copolymers to structure-direct transition metal nitrides(*5*, *6*, *12*, *13*), and most have made use of custom synthesized triblock terpolymers based on poly(isoprene-*b*-styrene-*b*-ethylene oxide) to generate complex co-continuous gyroidal block copolymer network morphologies. These materials, which are available commercially only from a single vendor at extreme cost, represent a substantial impediment to the expanded study and application of ordered mesoporous transition metal nitrides. In contrast, poloxamer/Pluronics family poly(ethylene oxide-*b*-propylene oxide-*b*-ethylene oxide) (PEO-PPO-PEO) ABA triblock copolymers are widely commercially available. These

ABA triblocks have been widely used to produce ordered mesoporous silica and transition metal oxides with varying mesostructures and degrees of crystallinity(*14*, *15*), but as reviewed recently, their use in controlling the mesostructure of other families of functional inorganic materials such as carbides, sulfides, and nitrides has remained challenging(*16*). Indeed, the sole report of a mesoporous transition metal nitride from a Pluronics ABA triblock involved a titanium nitride material produced as a composite with carbon as support(*13*), substantially limiting opportunities for further processing and application in areas requiring the mechanical, electrochemical, and superconducting properties of the pure nitrides. Furthermore, to the best of our knowledge, no report exists to date of any block copolymer-directed pure mesoporous transition metal nitride with hexagonal morphology, the most common structure in studies of mesoporous materials.

One route to the synthesis of transition metal nitrides is treatment of transition metal oxides at high temperatures in flowing ammonia gas(*17*). This process has been used to produce niobium nitride from fibers of niobium oxide(*18*) and from both monolithic(*6*) and thin film(*4*) ABC triblock terpolymer-derived niobium oxides with strut sizes around 30 nm. In the micron-scale fibers, nitride formation was first reported at 800 ˚C, while in the terpolymer-derived materials nitride formation was first observed at 600 ˚C. This decrease is correlated with the dramatically decreased solid-state diffusion length and increased accessibility to gas flow in mesostructured materials, suggesting that further increasing porosity and/or lowering wall thickness may enable oxide-

nitride conversion at even lower temperatures, thereby allowing use of the relatively low molar mass Pluronics copolymers.

The synthesis of mesoporous structures consisting of atomically crystalline materials generally relies on either confining crystallization with a mechanical support such as carbon(*9*), or on optimizing the kinetics of crystal growth so that individual crystal grains do not grow larger than the size of the mesostructured pore walls(*19*). The first route is multi-step and requires optimization of chemistries to remove the support material without degradation to the underlying functional material (*e.g.* oxidation of a nitride), while the second route is direct, but requires careful choice of reaction parameters to balance the competing kinetically-limited processes of formation of the phase of interest with isotropic grain growth. For inorganic materials derived from poloxamer/Pluronic triblock copolymers, typical pore wall thickness is between 50 and 100 Å,(*20*) only slightly larger than the first supercritical crystalline nuclei which form in classical nucleation theory. Any synthetic approach based on the latter route must therefore reach a temperature high enough to nucleate the phase of interest, but remain at a temperature low enough and for a time short enough that grains do not continue to grow significantly. The challenging combination of small wall thickness and high formation and crystallization temperatures have prevented access to poloxamer/Pluronics copolymer derived pure mesoporous nitrides in the past *(14)*.

Results and Discussion

Based on these considerations, we developed synthetic routes (Figure 3.1) to

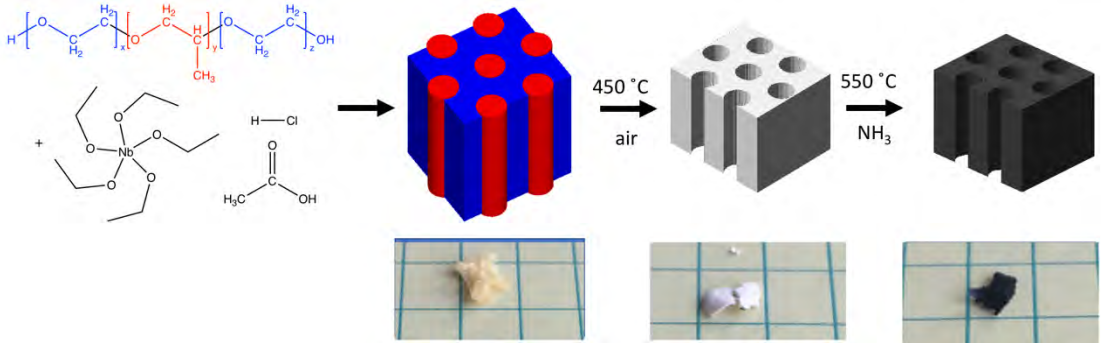

Figure 3.1: Schematic of synthetic route to mesoporous niobium nitride (top row) and photographs (bottom row) of corresponding oxide-polymer hybrid, freestanding oxide, and freestanding nitride against quarter-inch gridlines.

hexagonally ordered, mesoporous niobium nitrides with sub-10-nm pores using poly(ethylene oxide-*b*-propylene oxide-*b*-ethylene oxide) ABA triblock copolymers (BASF Pluronic F127) and carefully tuned thermal processing conditions. First, a mesostructured oxide-polymer hybrid composite is prepared by a sol-gel condensation of niobium (V) ethoxide catalyzed by a combination of acetic and hydrochloric acid in ethanol, followed by solvent evaporation. The resulting hybrid films can then be calcined at 450 ˚C in air to remove the block copolymer and other organic species, producing an amorphous, white, ordered mesoporous niobium (V) oxide. This oxide is then treated in flowing ammonia gas, *e.g.* at a temperature of 550 ˚C for 90 min, to produce a visibly black, monolithic material. As revealed by *ex situ* as well as *in situ* small- and wide-angle x-ray scattering (SAXS/WAXS), small deviations from these processing conditions often result in either amorphous but mesostructured materials or highly crystalline materials with poor mesostructure retention due to the delicate

balance between crystallization of the nitride phase of interest and growth of the crystalline domains beyond the pore wall thickness. The narrowness of this processing window is likely responsible for previous failures in the synthesis of Pluronics directed mesoporous nitrides.

To characterize the mesoporosity and crystallinity of the material after every processing step, we first used *ex situ* SAXS and WAXS, see Figure 3.2. SAXS patterns exhibited a strong main peak which, if assigned to a hexagonal lattice, represent d_{100} spacings of 13 nm, 9.7 nm, and 8.8 nm for the hybrid, oxide, and nitride, respectively (Figure 3.2A, bottom to top). Interestingly, the lattice order improves with each processing step, as determined by the sharpness of the smallest angle peak and appearance and increase in intensity of higher order peaks. The WAXS pattern for the freestanding oxide (Figure 3.2B, bottom) was indicative of an atomically amorphous material, consistent with past observations of mesoporous niobium (V) oxide treated at these temperatures(*6*, *20*). The WAXS pattern for the nitride sample (Figure 3.2B, top) exhibited peaks consistent with a rock salt lattice (space group Fm3m) with a lattice constant of 4.26 Å. This lattice constant is considerably lower than that of pure, bulk delta-phase niobium nitride samples grown by, *e.g.*, magnetron sputtering(*21*), and is consistent with residual oxygen and cation site vacancies in the lattice, as observed in other mesoporous nitrides(*12*) as a result of incomplete interdiffusion of oxygen and nitrogen during ammoniolysis. This class of materials is also referred to as niobium oxynitrides, with formulae most accurately given by $NbN_xO_y[]_{1-x-y}$ where [] indicates vacancies. The material

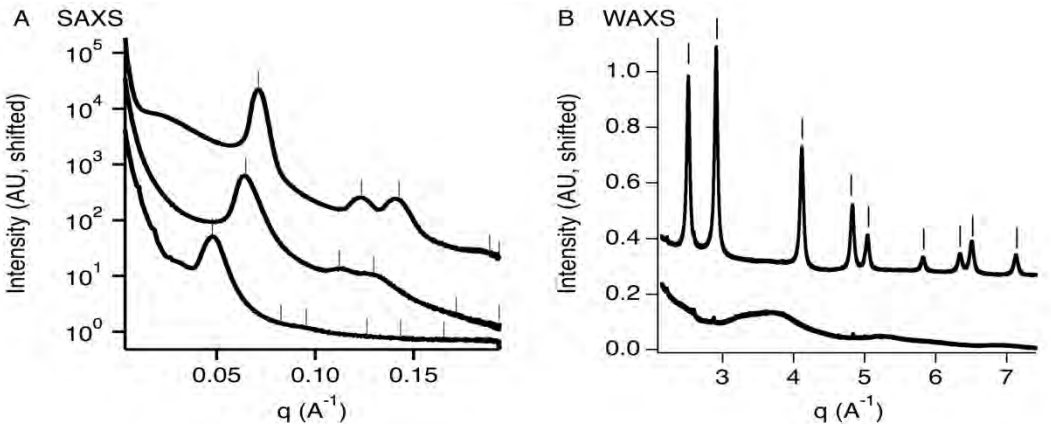

Figure 3.2: Material characterization by small- and wide-angle X-ray scattering (SAXS and WAXS). (A) SAXS traces of polymer-oxide hybrid (bottom, d_{100} = 13 nm), freestanding oxide (middle, d_{100} = 9.7 nm), and freestanding nitride (top, d_{100} = 8.8 nm). All markings indicate expected reflections for a hexagonal lattice with the given d_{100} spacings. (B) Synchrotron WAXS traces of mesoporous oxide (bottom) and nitride (top). Peak markings (|) are consistent with a NaCl-type lattice with a unit cell dimension of 4.26 Å. This material was nitrided at 550 ˚C for 90 minutes.

may also possess a significant fraction of cation vacancies driven by incomplete reduction of the Nb^{5+} to Nb^{3+} and incomplete densification of the material during ammoniolysis. Both factors – oxygen and anion site vacancies as well as cation site vacancies – may contribute to a reduced lattice parameter when compared with defect-free NbN.

Debye-Scherrer analysis of the WAXS data gives an upper bound for the coherent scattering domain size of 6.5 nm. This is smaller than reported pore wall sizes in similar F127-derived mesoporous materials(*20*), consistent with crystallization within the bounds of the mesostructured material wall. We suspect that the relatively low temperature of 550 ˚C for formation of the nitride

allows extremely little grain growth, essentially trapping the first supercritical nuclei and producing a highly nanocrystalline material, thereby enabling retention of the mesostructure.

To corroborate the SAXS structure assignment and confirm that the materials had open and accessible mesopores, we used a combination of transmission electron microscopy (TEM) and nitrogen physisorption (Figure 3.3). The TEM images were consistent with mesoporous structures with repeat distances of 9 nm for the oxide and 8 nm for the nitride, comparable to lattice parameters observed by SAXS (*vide supra*). The nitride image (Figure 3.3B) clearly shows both face-on (along the cylinders' long axis) and edge-on (normal to the cylinders' long axis) views consistent with hexagonal symmetry. The nitrogen physisorption data (Figure 3.3C) exhibited a type IV(a) behavior with a H1 type hysteresis(*22*), consistent with other block copolymer-derived mesoporous materials. The

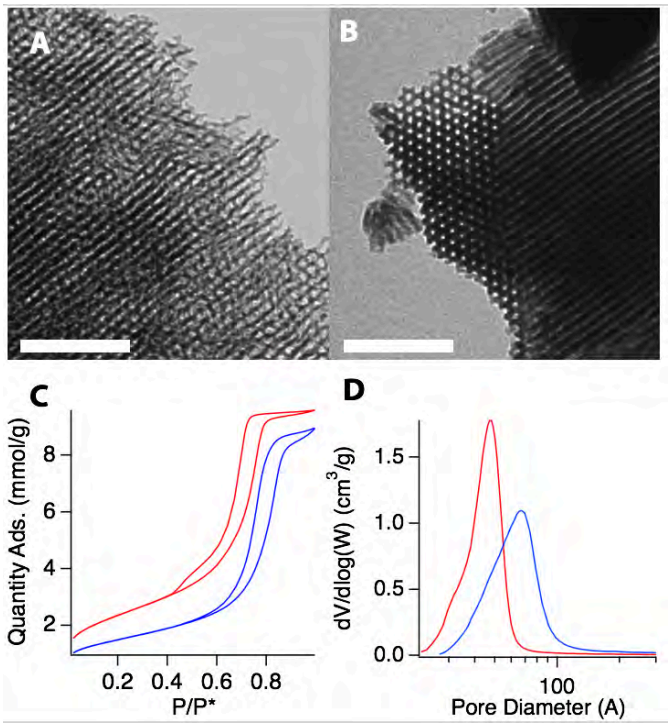

Figure 3.3: Material characterization by transmission electron microscopy and nitrogen physisorption. (A) TEM of freestanding mesoporous oxide and (B) of freestanding mesoporous nitride. All scale bars are 100 nm. (C) Nitrogen sorption isotherms of oxide (red) and nitride (blue). (D) Nitrogen sorption-derived pore size distributions of oxide (red) and nitride (blue).

physisorption patterns were analyzed(*23*, *24*) to determine the pore size distribution and overall pore surface area (Figure 3.3D). The oxide sample had a surface area of 183.3 $m^2 g^{-1}$, while the nitride sample had a surface area of 116.6 $m^2 g^{-1}$. Both values are consistent with those reported for mesoporous oxides(*20*), with the lower surface area in the nitride likely being due to shrinkage and densification of the material overall(*6*). The oxide pore size distribution included a pronounced tail toward smaller pore sizes, while the nitride pore size distribution exhibited a more uniform behavior. This may be a result of micropores collapsing or access to the pores closing over as the structure shrinks during processing. Further, the pore size distribution shows an increase in pore diameter from 48 Å in the oxide to 68 Å in the nitride. This is consistent with observation of the micrographs and with the expected densification of the material (ca. 50% based on comparison of bulk densities(*25*)).

The combination of SAXS and N_2 sorption data suggests that the overall mesoscale lattice shrinks slightly, but the densification of the material is so dramatic that the pore size increases despite the overall structure shrinkage. In other words, the material deforms as it undergoes solid-state chemical reaction to accommodate a 50% or greater volume shrinkage by a combination of direct densification of the pore walls (leading to larger BET-measured pore sizes) and by shrinkage of the entire mesoscale lattice (leading to smaller SAXS-measured lattice parameters). Specifically, the SAXS lattice parameter decreases by 10% indicating overall material volume shrinkage of 25% (based on SAXS-measured

lattice parameters), yet the pore wall diameter shrinks by 24% (based on analysis of TEM images), indicating a pore wall volume shrinkage of ca. 40%. The 20% increase in pore diameter observed by N_2 sorption is thus reasonable in the context of the SAXS and TEM measurements.

The optimization of crystallinity in block copolymer-derived mesoporous materials has been a significant challenge. Since the reported heat treatment at 550 ˚C for 90 min produces materials on the edge of the first observable crystalline nitride grains, small variations in processing conditions substantially influence the crystallinity of the resulting nitride and/or retention of the mesostructure. For example, *ex situ* SAXS and WAXS on a material treated for a slightly longer time of 120 minutes (Figure 3.4, top traces) instead of 90 minutes at 550 ˚C (Figure 3.4, middle traces) show larger coherent scattering domain sizes and lattice parameters in WAXS indicative of lower oxygen and vacancy concentration, but lower mesostructure quality as indicated by significantly lower intensity in the higher-order SAXS peaks. In contrast, SAXS and WAXS on samples treated for 90 minutes at a lower temperature of 500 ˚C indicate equivalent mesostructure retention to treatment at 550 ˚C for 120 minutes but a lack of any WAXS peaks (Figure 3.4, bottom traces), consistent with very limited or no crystal growth. Interestingly, despite having no detectable crystallinity in WAXS, the sample treated at 500 ˚C remained optically black, a feature typically associated with metallic conducting materials (*e.g.* NbN) and not with semiconductors and insulators (*e.g.* Nb_2O_5).

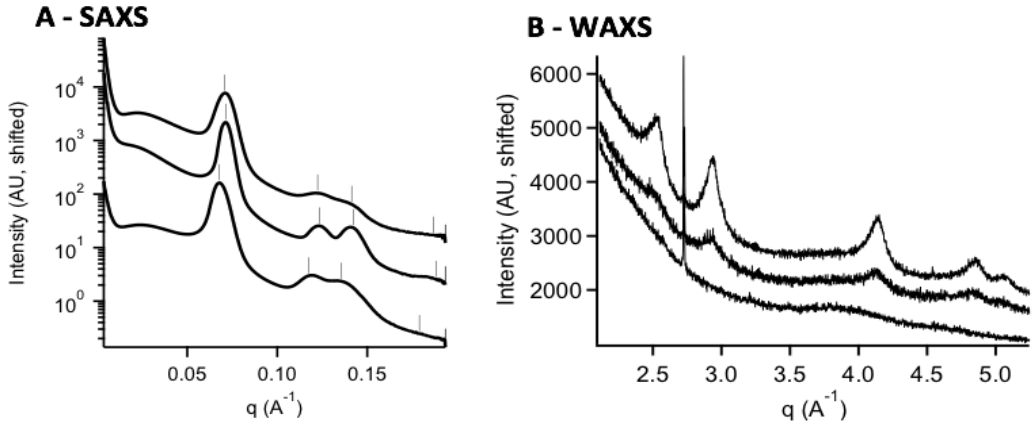

Figure 3.4: (A) SAXS patterns for nitrides produced at (top) 550 ˚C for 120 min, (middle) 550 ˚C for 90 min, and (bottom) 500 ˚C for 90 min. Tick marks indicate expected peak positions for a hexagonal morphology relative to the observed primary peak, with the top two traces having a d_{100} spacing of 8.8 nm. The bottom trace has a d_{100} spacing of 9.1 nm, indicative of a lower degree of shrinkage. (B) Lab source WAXS patterns from the materials in (A), showing a corresponding increase in crystallinity with increasing heating temperature or time (as in A). Mesostructure loss occurs concurrently with additional crystallization of the material at even slightly longer times, while materials treated at lower temperatures do not exhibit any resolvable WAXS peaks. The extremely sharp WAXS peak at ca 2.65 $Å^{-1}$ is a known instrument artifact. The lower intensities and increased widths relative to the synchrotron data are a result of lower signal and increased source broadening on the lab diffractometer.

To further probe the thermal conditions under which crystalline, mesoporous nitrides can be synthesized, we used *in situ* synchrotron SAXS/WAXS during annealing in ammonia in a custom flow furnace (see photo in Figure 3.S1) during a 5 ˚C min^{-1} ramp from room temperature to 720 ˚C (Figure 3.5). Please note that because of the time constraints at a synchrotron, this thermal

processing history is considerably different from the *ex situ* experiments described so far, where the final temperatures of 500 ˚C or 550 ˚C were held between 90-120 minutes, *vide supra*, while here the temperature steadily increased at the 5 ˚C min^{-1} rate. Consistent with results in Figure 3.4A, *in situ* SAXS (Figure 3.5A) reveals: (i) A hexagonal mesostructure at a temperature around 540 ˚C, which at the heating rate of 5 ˚C min^{-1} vanishes above 680 ˚C, as evidenced by the loss of higher-order SAXS reflections; (ii) Between 540 ˚C and 680 ˚C the first order peak steadily shifts to higher q values indicating continuous material densification, from a lattice parameter of 9.3 nm at 540 ˚C to a lattice parameter of 8.8 nm at 680 ˚C. The final pattern at 720 ˚C, if assigned to a hexagonal lattice, would have a lattice parameter of 8.4 nm. These parameters are consistent with *ex situ* observations, *vide supra*. *In situ* WAXS (Figure 3.5B) exhibited clear peaks consistent with the rocksalt NbN phase beginning at 610 ˚C, at which point the nitride lattice parameter is 4.12 Å. The first emergence of such peaks may occur at lower temperatures of ca. 540-560 ˚C, but at the ramp rate of 5 ˚C min^{-1} the peak widths are so high that unequivocal peak identification above the background is challenging. As the temperature increases, the WAXS peaks shift gradually toward increased lattice parameters, reaching a value of 4.23 Å at 680 ˚C, the last temperature where the sample exhibits clear higher order reflections in SAXS indicative of long range hexagonal mesostructural order, and ultimately reaching a value of 4.32 Å at 720 ˚C. Compared to the lattice parameter of 4.26 Å attained after holding at 550 ˚C for 90 minutes, these results suggest alternative routes to similar quality

nitrides (or even better, less defective materials) involving shorter anneals at higher temperatures.

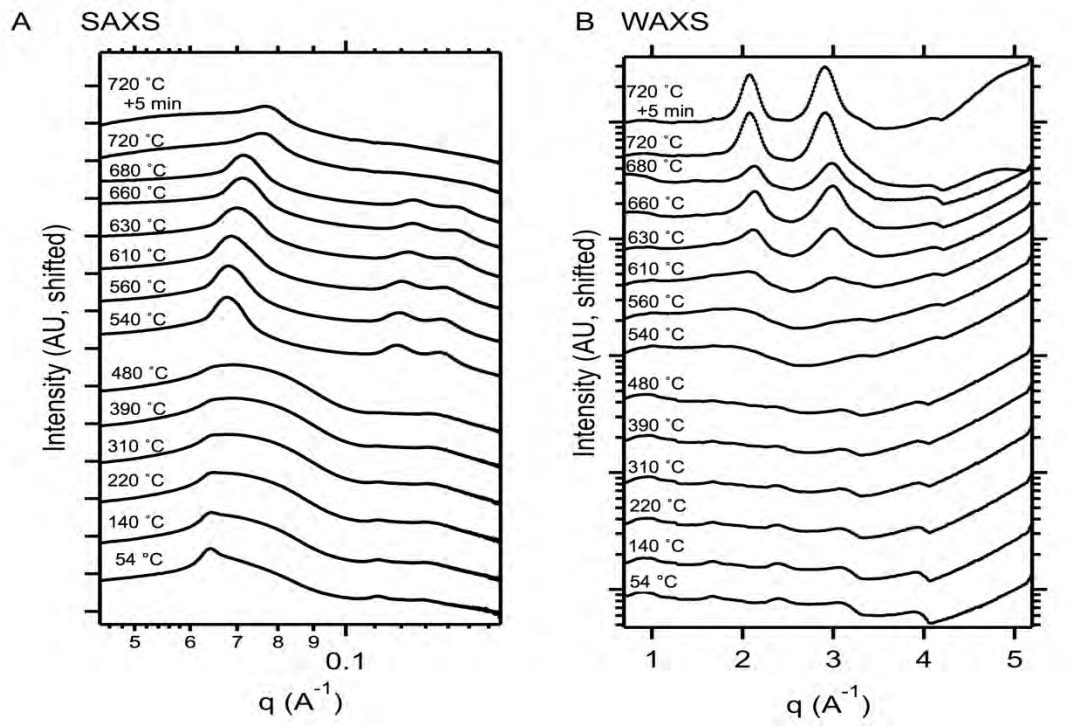

Figure 3.5: *In situ* SAXS (A) and WAXS (B) data collected from a mesoporous oxide sample during a 5 ˚C min^{-1} ramp from room temperature to 720 ˚C under flowing ammonia gas. The window from 560 ˚C to 660 ˚C in which both SAXS peaks (indicative of mesoporosity) and WAXS peaks (indicative of crystalline nitride) are observed can be used to guide processing.

Conclusion

In summary, we described routes to synthesize hexagonally ordered freestanding mesoporous niobium nitrides from ordered mesoporous niobium oxide structured by commercially available Pluronics ABA triblock copolymers based on treatment at moderate temperatures and times (*e.g.* 550 ˚C for 90 min) under flowing ammonia gas. We further demonstrated the sensitivity of

mesostructural order and crystallinity of the resulting materials to relatively small variations of heat treatment temperature and duration, which likely is the reason Pluronics-based routes to mesoporous nitrides had previously been challenging. We expect the synthetic routes discussed will open the door to wider exploration of the impact of mesoscale order on the properties and applications of mesoporous transition metal nitrides.

Acknowledgements

We thank the NSF for support via a Single Investigator Award (DMR-1707836). P.A.B. was supported by the NSF Graduate Research Fellowship Program (DGE-1650441). This work made use of the Cornell High Energy Synchrotron Source, which was supported by the NSF and the NIH/National Institute of General Medical Sciences under NSF award DMR-0936384, and the Cornell Center for Materials Research, which is supported by the NSF Materials Research Science and Engineering Centers program (DMR-1120296). We thank J.P.C. Ruff and J. Lee for kind assistance with synchrotron WAXS measurements, F.J. DiSalvo for helpful discussions, and H. Joress, D. Richter, and A. Woll for kind assistance with *in situ* synchrotron experiments.

Materials and Methods

Materials Ethanol (anhydrous, SureSeal) and Pluronic F127 were purchased from Sigma-Aldrich. Niobium (V) ethoxide (99.999% metals basis) was purchased from Alfa Aesar. Acetic acid (glacial) and hydrochloric acid (37%) were purchased from

Fisher Scientific. Ammonia (electronic grade, 99.9995%) was purchased from Praxair. Nitrogen (BIP grade) and air (Ultra Zero grade) were purchased from Airgas. All materials were used as received unless otherwise noted.

Methods Mesoporous niobium (V) oxide films were prepared via a slightly modified version of a previously reported acetic-acid-mediated sol-gel synthesis procedure (20). Briefly, 800 mg of Pluronic F127 was dissolved in a mixture of 15 mL anhydrous ethanol, 0.570 mL acetic acid, and 0.371 mL hydrochloric acid. 1.25 mL niobium (V) ethoxide was added under vigorous stirring. The resulting solution was stirred vigorously for 12 h before transferring to a 30mL PTFE beaker. The solvent was then allowed to evaporate at 40 ˚C for 24 h, after which the film was transferred to an oven at 60 ˚C for an additional 24 h. No particular measures were taken to control relative humidity during evaporation, which ranged from 40% to 70% with no noticeable differences in film quality.

The resulting hybrid films were treated in an open tube furnace (Lindberg model 55035) in air by ramping at a temperature of 1 ˚C min^{-1} to 450 ˚C, holding for 3 h, then cooling at 25 ˚C min^{-1} to room temperature.

To convert the oxides to nitrides, a flow-through tube furnace (Lindberg model 55035, with a 1” quartz tube and gas flow meter) was used with a flow rate of 10 L h^{-1} of ammonia gas. The furnace was ramped at 5 ˚C min^{-1} to 550 ˚C, held for 90 minutes, and cooled at 25 ˚C min^{-1} or slower to room temperature. For some samples 500 ˚C or

120 minutes were used – see main text. After cooling to room temperature, the tube was purged first with dry nitrogen (10 L h^{-1} for 2 h) and then with dry air (20 L h^{-1} for 1 h). The air purge was intended to limit any possible oxidation of the material to a thin, passivating surface layer.

Nitrogen physisorption Nitrogen physisorption isotherms were collected on a Micromeritics ASAP 2020 surface area and porosity analyzer at 77 K. Samples were loaded in oven-dried glass tubes and degassed under vacuum at 130 ˚C for at least 12 h before measurement.

Small-Angle X-Ray Scattering (SAXS) SAXS data were collected at station G1 of the Cornell High Energy Synchrotron Source (CHESS) with an incident beam energy of 9.83 keV collimated to a 200 um square via a standard three-slit setup, and a sample-to-detector distance of 2.2 m. Scattering patterns were recorded on an Eiger 1M pixel array detector (Dectris, Inc.). The resulting 2D SAXS patterns were radially integrated using the Nika package for Igor Pro (26).

Wide-Angle X-Ray Scattering (WAXS) WAXS data in Figure 3.2 were collected at station A2 of the Cornell High Energy Synchrotron Source, with an incident beam energy of 18.9 keV. A four-circle diffractometer was used with a Dectris Eiger 1M pixel array detector (Dectris, Inc.) scanning over an angular range from 0˚ to 49˚ in 2θ in 5˚ steps, collecting for 240 s at each step. The resulting datasets were corrected for differential solid angle and other factors using the in-house instrument software to

produce one-dimensional intensity *vs* q datasets. The reported coherent scattering domain size was determined by use of the Debye-Scherrer equation using a shape factor **K** of 0.9 and the average of the first five observed peaks for the d-NbN phase. WAXS data in Figure 3.4 were collected on a Rigaku Ultima IV diffractometer using Cu Kα radiation (E=8.95 keV) and a D/Tex Ultra detector. Scans were conducted at 2 ˚ min^{-1} over a range of 2θ from 30˚ to 80˚ and converted to the scattering vector $\mathbf{q}=4\pi \sin(\theta)/\lambda$ for direct comparison with synchrotron data, where 2θ is the total scattering angle and λ is the x-ray wavelength.

***In situ* SAXS/WAXS** *In situ* SAXS and WAXS data in Figure 3.5 were collected simultaneously on oxide samples undergoing thermal treatment in flowing ammonia gas using a custom apparatus (Figure 3.S1). A commercial SabreTube rapid thermal processing unit (Absolute Nano) was equipped with a custom quartz tube with sealed Mylar windows to allow the transmission of incident and scattered x-ray beams. The SabreTube design uses a semi-consumable silicon resistive heating element to which a thermocouple can be adhered (using high-temperature cement or spring contacts) for temperature control. The furnace was equipped with a gas flow manifold and an exhaust system in order to allow the use of toxic gases, *e.g.* ammonia in addition to inert gases and air. In order to minimize the risk of personnel exposure to ammonia, the furnace area was ventilated by the exhaust system, the tube was thoroughly purged before opening, and only small quantities of ammonia (<0.3 lb) were used at any given time.

A Dectris Pilatus 100k pixel array detector was used for collection of WAXS data. The detector was placed ca. 5 cm from the exit window of the furnace at a ca. 30 degree angle from the incident beam to maximize the solid angle captured. The exact tilt and sample-detector distance was calibrated by the use of a lanthanum hexaboride standard, then further refined for the exact sample geometry used by comparison of *ex situ* and *in situ* datasets from the same sample at the conclusion of heat treatment. Images were corrected using the values of tilt and sample-detector distance from this comparison and radially integrated with the Nika software package for Igor Pro (26).

A Dectris Eiger 1M pixel array detector placed at the end of a 1.6m evacuated flightpath was used for collection of SAXS data. The sample-detector distance was calibrated using a silver behenate standard and images radially integrated using the Nika software package for Igor Pro (26).

A sample of mesoporous oxide was placed on the heating platform and translated into the beam position. The heating platform was leveled with respect to the incoming beam so as to eliminate any diffraction contribution from the silicon heater substrate. The furnace was then programmed to ramp at a rate of 5 ˚C min^{-1} to 720 ˚C, with SAXS and WAXS patterns collected continuously in 5 s frames.

Transmission Electron Microscopy (TEM) TEM images were collected on an FEI Tecnai T12 microscope operated at an accelerating voltage of 120 kV. Samples were finely ground in water using an agate mortar and pestle and drop-cast onto polyvinyl

butyral-coated copper TEM grids (Butvar ® B-98, Sigma-Aldrich). Lattice parameters were determined from TEM images by analysis of integrated profiles of edge-on regions of the images to obtain a cylinder-to-cylinder distance, which was then converted to hexagonal lattice spacing. Pore wall thicknesses were determined by fitting representative line-cuts of pore walls with a series of inverse Gaussian functions to determine the average wall thickness.

Author Contributions

P.A.B. and U.B.W conceived the project. P.A.B synthesized samples, performed and analyzed N_2 sorption, WAXS, and *in situ* SAXS/WAXS measurements. S.M.G. and P.A.B. performed and analyzed SAXS measurements. E.M.S. performed and analyzed TEM measurements. P.A.B., S.M.G., and U.B.W. wrote the manuscript. All authors have given approval to the final version of the manuscript.

REFERENCES

1. M. Yang, A. R. Van Wassen, R. Guarecuco, H. D. Abruña, F. J. DiSalvo, *Chem. Commun.* **49**, 10853–10855 (2013).
2. H. Cui *et al.*, *Adv. Sci.* **2**, 1500126 (2015).
3. Z. Wang, A. Kawakami, Y. Uzawa, B. Komiyama, *J. Appl. Phys.* **79**, 7837–7842 (1996).
4. K. E. Fritz, P. A. Beaucage, F. Matsuoka, U. Wiesner, J. Suntivich, *Chem. Commun.* **6**, 1582–1588 (2017).
5. B. G. Kim *et al.*, *ACS Nano*. **11**, 1736–1746 (2017).
6. S. W. Robbins *et al.*, *Sci. Adv.* **2**, e1501119 (2016).
7. M. Templin, *Science.* **278**, 1795–1798 (1997).
8. T. N. Hoheisel, K. Hur, U. B. Wiesner, *Prog. Polym. Sci.* **40**, 3–32 (2015).
9. J. Lee *et al.*, *Nat. Mater.* **7**, 222–228 (2008).
10. Y. Zhu *et al.*, *J. Am. Chem. Soc.* **139**, 10365–10373 (2017).
11. H. Arora *et al.*, *Science.* **330**, 214–219 (2010).
12. S. W. Robbins, H. Sai, F. J. Disalvo, S. M. Gruner, U. Wiesner, *ACS Nano.* **8**, 8217–8223 (2014).
13. E. Ramasamy *et al.*, *Chem. Mater.* **24**, 1575–1582 (2012).
14. D. Zhao *et al.*, *Science.* **279**, 548–52 (1998).
15. P. D. Yang, D. Y. Zhao, D. I. Margolese, B. F. Chmelka, G. D. Stucky, *Nature.* **396**, 6–9 (1998).

16. J. Wei *et al.*, *J. Am. Chem. Soc.* **139**, 1706–1713 (2017).

17. G. Brauer, *J. Less Common Met.* **2**, 131–137 (1960).

18. K. Nomura, Y. Takasuka, K. Kamiya, H. Nasu, *J. Mater. Sci. Mater. Electron.* **5**, 53–58 (1994).

19. S. C. Warren *et al.*, *Nat. Mater.* **11**, 460–467 (2012).

20. J. Fan, S. W. Boettcher, G. D. Stucky, *Chem. Mater.* **18**, 6391–6396 (2006).

21. S. P. Chockalingam, M. Chand, J. Jesudasan, V. Tripathi, P. Raychaudhuri, *Phys. Rev. B.* **77**, 214503 (2008).

22. M. Thommes *et al.*, *Pure Appl. Chem.* **87**, 1051–1069 (2015).

23. S. Brunauer, P. H. Emmett, E. Teller, *J. Am. Chem. Soc.* **60**, 309–319 (1938).

24. E. P. Barrett, L. G. Joyner, P. P. Halenda, *J. Am. Chem. Soc.* **73**, 373–380 (1951).

25. D. R. Lide, *CRC Handbook of Chemistry and Physics, 94th Edition, 2013-2014* (2013), vol. 53.

26. J. Ilavsky, *J. Appl. Crystallogr.* **45**, 324–328 (2012).

APPENDIX

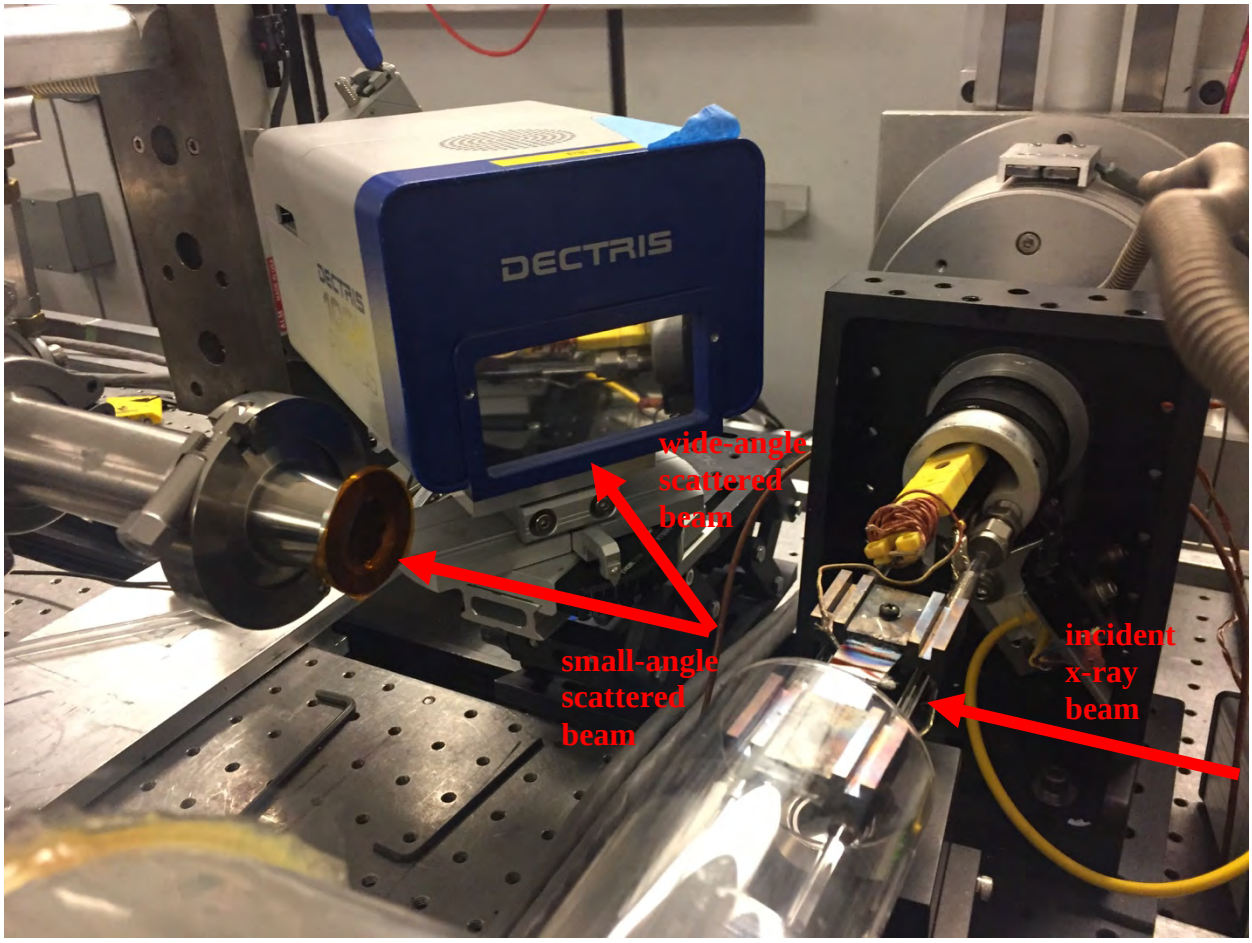

Figure 3.S1. Photograph of the apparatus for *in situ* SAXS/WAXS measurements, with the quartz tube temporarily removed.

CHAPTER 4

MESOPOROUS NIOBIUM CARBONITRIDE SUPERCONDUCTORS FROM BLOCK COPOLYMER SELF-ASSEMBLY: TOWARD SOFT QUANTUM MATERIALS[3]

Introduction

Ordered mesostructures allow access to mesostructure-derived materials properties that can be very different from their bulk counterparts. For example, simulations have shown the appearance of a photonic bandgap and negative refractive indices in metals with the alternating gyroid ($I4_132$) structure(*1*), and simulations of other mesoscale network phases show topologically protected Weyl states(*2*) and phononic band gaps(*3*). The manipulation of material symmetry via such superstructures can further open access to properties disallowed by the symmetry of the underlying crystal, e.g. "improper" ferroelectricity(*4*). This strategy has shown substantial promise in simple superstructures, e.g. layers, but has not been substantially expanded to more complex symmetries, e.g. the noncentrosymmetric alternating gyroid (space group $I4_132$). Mesostructured superconductors, in particular, are expected to be a fertile area for exploration of the impact of mesoscale order on the properties of correlated electron systems. For example, the introduction of simple one- or two-dimensional ordered porosity can create arrays of artificial flux pinning centers and enhance the critical field, among other properties(*5, 6*). However, the exploration of these phenomena is

[3] Peter A. Beaucage, Francis J. DiSalvo, Sol M. Gruner, Ulrich B. Wiesner, *manuscript in preparation*

extremely limited by a lack of synthetic strategies to prepare three-dimensionally ordered mesostructured superconducting materials.

One promising method to fabricate such structures is block copolymer self-assembly (BCP SA). BCP SA is an extremely versatile, tunable technique to produce ordered structures with potentially complex symmetry on length scales typically between 10-100 nm. The method, traditionally strictly in the realm of soft condensed matter physics, has recently been extended to produce functional materials (e.g. oxides(*7*), semiconductors(*8*), and low-T_c superconductors(*9*)) with mesostructure controlled by the parent block copolymer structure. This convergence of soft and hard condensed matter physics may prove to be an exceptionally fruitful area for development of new quantum materials, applying the exceptional structure control and unique, noncentrosymmetric structures accessible by block copolymer self-assembly to emergent and improper properties in correlated electron systems. However, the synthesis of high-purity quantum materials (e.g. superconductors) is extremely limited by the constraints of crystal growth inside mesoporous materials. In short, conventional solid-state thermal processing requires operation in a narrow window of temperature and time so as to produce the phase of interest without growth of crystalline domains beyond the boundaries of the mesostructure, which results in structure collapse(*10*). While methods such as addition of a support framework(*11*) or directional recrystallization may extend the processing window, the realization of mesostructured quantum materials via direct templating requires careful selection of the material of interest and optimization of its synthetic conditions. In superconductors in particular, the only study to date(*9*) produced niobium oxynitrides

on the edge of mesostructure collapse and with T_c of about 8 K, less than half the best-reported bulk value.

Results and Discussion

In this work, we developed a series of synthetic routes to mesostructured niobium carbonitrides based on a block copolymer self-assembly route to niobium nitrides(*9*). Briefly, a triblock terpolymer poly(isoprene-b-styrene-b-ethylene oxide) ISO (86 kDa, 29 vol% PI, 64 vol% PS, 7 vol% PEO) was used to template sol-gel-derived niobium (V) oxide nanoparticles into the alternating gyroid morphology. The resulting polymer-oxide hybrid was calcined at 450 ˚C in air to remove the polymer, then nitrided at 700 ˚C for 12 h in flowing ammonia gas to produce a niobium oxynitride of the approximate formula $NbN_{0.55}O_{0.45}$. This oxynitride was then subjected to one of four gas treatments: either an additional anneal at at 865 ˚C for 3 h in NH_3 (as in (*9*)), 865 ˚C for 3 h in argon, 865 ˚C for 3 h in forming gas (5% H_2 in N_2) to produce a reduced nitride, or at up to 1000 ˚C for 3 h in carburizing gas (16/4/80 vol% $CH_4/H_2/N_2$) to produce a carbonitride or carbide (Figure 4.1).

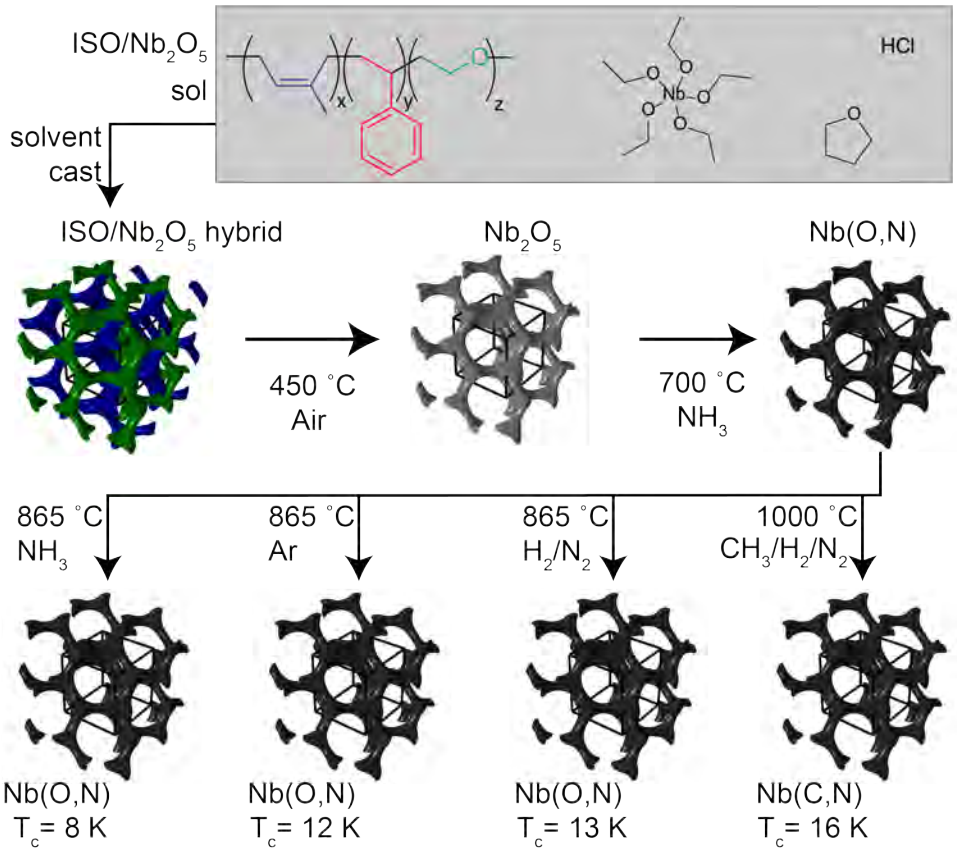

Figure 4.1: Synthetic Routes to Mesostructured Nitrides and Carbonitrides. Variation of the final gas annealing step can change the T_c of the resulting material by a factor of 2 (*vide infra*).

The resulting materials were first characterized using x-ray diffraction/wide angle x-ray scattering (XRD/WAXS) to probe their transformation (Figure 4.2B, Table 4.1). Interestingly, annealing in inert gas (Ar) results in a higher lattice parameter (typically associated with higher N/O ratio) than annealing in ammonia. This serendipitous result can be understood in the context of a material of the form $NbN_xO_y[]_{1-x-y}$, where [] denotes vacancies. The vacancy concentration stems from kinetic trapping of vacancy states in the lattice during transformation, with an equilibrium limit

associated with the oxidation state of the Nb centers in the lattice (*12*). Annealing in high-purity argon, rather than in ammonia, does not involve reactive processes and allows the material to equilibrate at a lower overall vacancy concentration. Even more interestingly, the coherent scattering domain size of the sample annealed in argon is lower relative to that of the superconducting sample re-annealed in ammonia. This result, while *prima facie* counterintuitive, is expected in the context of the driving forces for crystal growth. Using the conventional wisdom that bulk diffusion contributes to domain growth at $T > 1/2\ T_m$, one would not expect bulk crystal growth from temperature alone until about 1150 ˚C. The remarkable crystal growth in the 865 ˚C ammonia re-annealing is thus likely a product of reactive re-precipitation of nitride, rather than thermal crystal growth. Therefore, solid-state reactions with a lower tendency toward recrystallization may result in less grain growth. To further probe this hypothesis, we annealed the starting nitride in forming gas, which should more fully reduce the niobium and also exhibit limited grain growth. As expected, the lattice parameter shifted toward the lower-vacancy or higher-nitrogen direction, consistent with reduction of the material, while the domain size remarkably does not differ significantly from the starting material.

During these studies, we annealed the starting material in carburizing gas at temperatures of 910 ˚C and 1000 ˚C, again first due to a serendipitous error. Remarkably, the material treated at 1000 ˚C had a lattice parameter near that expected for a pure NbC material, despite a domain size of just 9 nm. Further experiments confirmed that temperature variation produced a series of lattice parameters with

minimal grain growth up to 1000 ˚C, though at 1100 ˚C the grains grew substantially and the mesostructure was lost (Figure 4.S1).

To confirm the Debye-Scherrer domain size results from WAXS, we used small-angle X-ray scattering (SAXS) to directly probe the degree of mesostructural order (Figure 4.2A, Table 4.1). Consistent with the WAXS data, the samples treated in Ar, FG, and carburizing gas had dramatically better retention of the mesostructure, as shown by the presence of a second-order feature in the Ar and FG treated nitrides and the clear presence of second- and even third-order reflections in the carbides/carbonitrides. To correlate the measured lattice parameters to superconducting properties, we used vibrating sample magnetometry (VSM, Figure 4.2C, Table 4.1). Strikingly, the Ar treated sample exhibited an onset T_c of 12.4 K (Figure 4.2C, inset) and flux exclusion nearly two orders of magnitude greater than the previous best-in-class NH_3 treated sample. Interestingly, despite a slightly higher Tc of 12.8 K, the FG treated sample had flux exclusion comparable to that of the original nitride. The carbonitride/carbide samples exhibited both strikingly enhanced flux exclusion (comparable to the Ar-treated nitride) and T_c as high as 16K, approaching the best literature reports for the pure NbN system(*13*) and within a few degrees of the best reported for the Nb-C-N pseudobinary alloys(*14*). The observed variation in T_c may be related primarily to the composition of the material (O/N ratio, vacancy concentration, and Nb oxidation state), while the flux exclusion may be related to the superconducting fraction of the material or to other inherent material properties.

Finally, to confirm the mesostructure retention in real space, we used scanning electron microscopy (SEM, Figure 4.2D-G). Consistent with the WAXS and SAXS

results, the structure in the ammonia treated nitride (Figure 4.2E) was noticeably degraded from the starting material (Figure 4.2D) with the forming gas treated nitride (Figure 4.2F) having a markedly better-preserved structure and the carbide (Figure 4.2G) having structure comparable to that in the starting material.

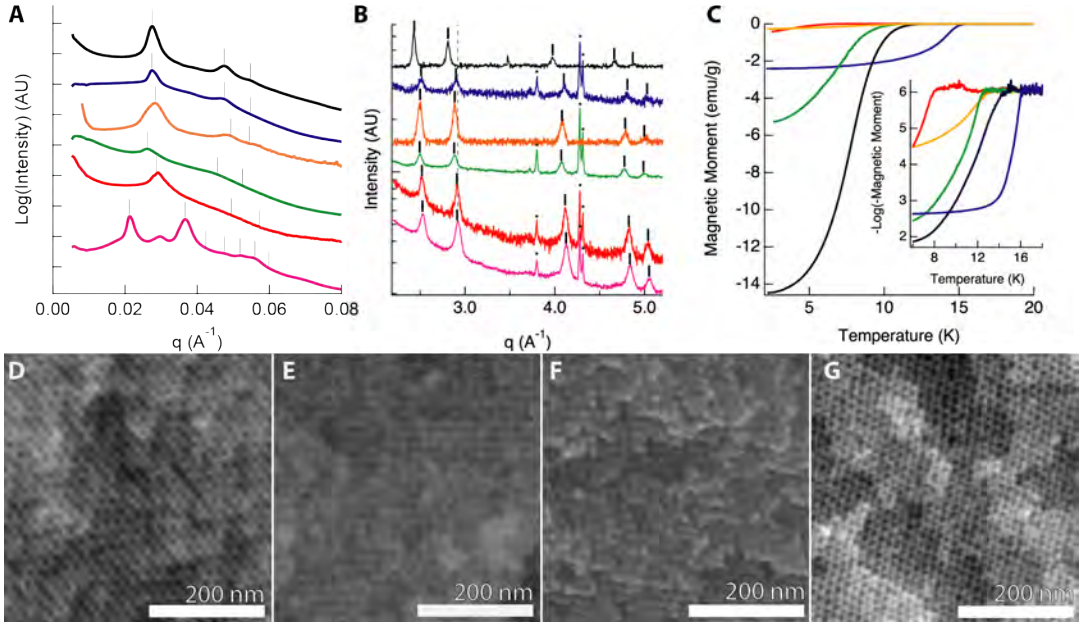

Figure 4.2: Structural characterization of samples re-annealed in various gases. (A) Synchrotron SAXS and (B) powder XRD/WAXS of starting nitride treated at 700 ˚C (bottom) and re-annealed nitrides treated at 865 ˚C in (bottom to top) ammonia, argon, forming gas, at 910 ˚C in dilute carburizing gas, and at 1000 ˚C in carburizing gas. In SAXS patterns, | denotes peaks consistent with a $I4_132$ structure (space group #214) with lattice parameters as given in Table 4.1. In WAXS | denotes peaks consistent with the NaCl type structure (lattice parameters given in Table 4.1), while * denotes instrument background peaks. (C) Temperature-dependent magnetization curves of samples re-annealed at 865 ˚C in (red) ammonia, (green) argon, (orange) forming gas, (black) carburizing gas, and (blue) dilute carburizing gas. (D-G) Scanning electron

micrographs showing structure preservation in the starting nitride (D) and samples re-annealed at 865 ˚C in ammonia (E), forming gas (F), and at 1000 ˚C in carburizing gas (G).

Table 4.1: Structural Parameters of Treated Materials

Gas Treatment	**Lattice Param. (A)**	**Coherent Scattering Domain Size (nm)**	**Mesostructure ($I4_132$) d_{100} (nm)**	**T_c (onset, K)**
Starting Material – 700 ˚C / 12 h	4.308	8	42.0 nm	N/A
+ 865 ˚C / 3h in NH_3	4.318	12	30.5 nm	7.9 K
+ 865 ˚C / 3h in Ar	4.363	10	33.8 nm	12.4 K
+ 910 ˚C / 3h in H_2/N_2	4.355	10	31.3 nm	12.8 K
+ 910 ˚C / 3h in $CH_3/H_2/N_2$	4.333	8	32.1 nm	14.2 K
+ 1000 ˚C / 3h in $CH_3/H_2/N_2$	4.469	9	32.2 nm	16.0 K

We speculate that the remarkable quality of the structure retention in the carbonitrides is due to the multistep pathway involved in production of active gas-phase species from methane as compared to ammonia. Ammonia is known to readily degrade to N and H radical species at temperatures above 700 ˚C(*15*), while methane degradation follows complex, multistep pathways(*16*). It stands to reason that these pathways may produce a strikingly lower concentration of active carbon species (ACS) in a CH_4-based gas blend when compared with NH_3, particularly considering that the presence of a carrier gas and H_2 likely shifts the degradation equilibrium for CH_4 to favor even lower ACS concentration. This low concentration of ACS results in a low rate of nitride-carbide conversion as compared to the rate of oxynitride-nitride conversion, resulting in less crystal growth at a given temperature and a dramatically

increased maximum processing temperature, from 865 ˚C to over 1000 ˚C (*vide supra*). The ability to process the material at such high temperatures enables yet-unachieved levels of both mesostructured retention and electronic material quality in mesostructured superconductors.

To demonstrate the versatility of this block copolymer-derived synthetic pathway, we used a single parent block copolymer to prepare samples with four characteristic morphologies based on a theoretical description of the phase behavior of the block copolymer(*17*) (Figure 4.3A) by adding varying amounts of oxide nanoparticle sol: one alternating gyroid network ($I4_132$, Fig. 4.3N), a perforated lamellar phase (layer group p-1, Figure 4.3J) , the double gyroid matrix (Ia3d, Figure 4.3F), and inverse hexagonally packed cylinders (P6, Figure 4.3B). The resulting materials' mesostructure retention was characterized at all processing stages by SAXS (Figure 4.3E,I,M,Q, from bottom to top: hybrid, oxide, nitride, and carbide). In all cases, the relative positions of the peaks remain consistent, indicating retention of the morphology through the various heat treatments, while the main peak position gradually shifts to higher q, indicating shrinkage of the mesostructure in all cases except the lamellae. These results are confirmed by SEM of both the intermediate nitrides (Figure 4.3C,G,K,O) and the final carbides (Figure 4.3D,H,L,P), which shows characteristic projections for each morphology.

In the case of the lamellae, SEM imaging suggests the presence of ordered perforations between the lamellar sheets (Figure 4.3K). This observation is corroborated by the presence of a peak at approximately 0.031 A^{-1}, a position which is

not consistent with an expected lamellar reflection but which is consistent with hexagonal order ($q/q^* = \sqrt{2}$). Generally, lamellar mesostructures cannot survive removal of the other block copolymer domains with retention of mesoscale porosity due to material collapse. The presence of these perforations may explain why the material is able to retain mesoscale structure despite heating to 1000 ˚C. The very weak and low-angle features observed in the SAXS patterns for the nitride and carbide likely originate from this hexagonal sublattice.

XRD was used to verify the production of the carbide phase (Figure 4.3S). Consistent with the results from the single-morphology studies, in all cases the carbide was prepared without significant impurity phases. The carbide lattice parameters and coherent scattering domain sizes are summarized in Table 4.S2, and the diffraction patterns for the intermediate nitrides are given in Figure 4.S2.

Finally, to verify that the ordered carbides were superconducting, we used VSM (Figure 4.3R). All four morphologies exhibited a superconducting transition with a high flux exclusion consistent with that of the carbides studied earlier. Remarkably, the samples of different morphology exhibited transition temperatures varying systematically with oxide loading in the starting hybrid from about 12 K in the alternating gyroid to over 15 K in the hexagonal cylinders. This result would not be unexpected given the highly surface-sensitive nature of the solid-state reaction, but it is curious that the transition temperatures vary without substantial variation of the XRD-measured lattice parameters. This suggests that the variation may be due to an inherent size- or morphology-related effect, rather than processing-induced compositional variations. Comparison of the strut thickness (derived from volume

fractions and SAXS-measured lattice parameters) and the T_c suggests a correlation, but is inconclusive (Figure 4.S3).

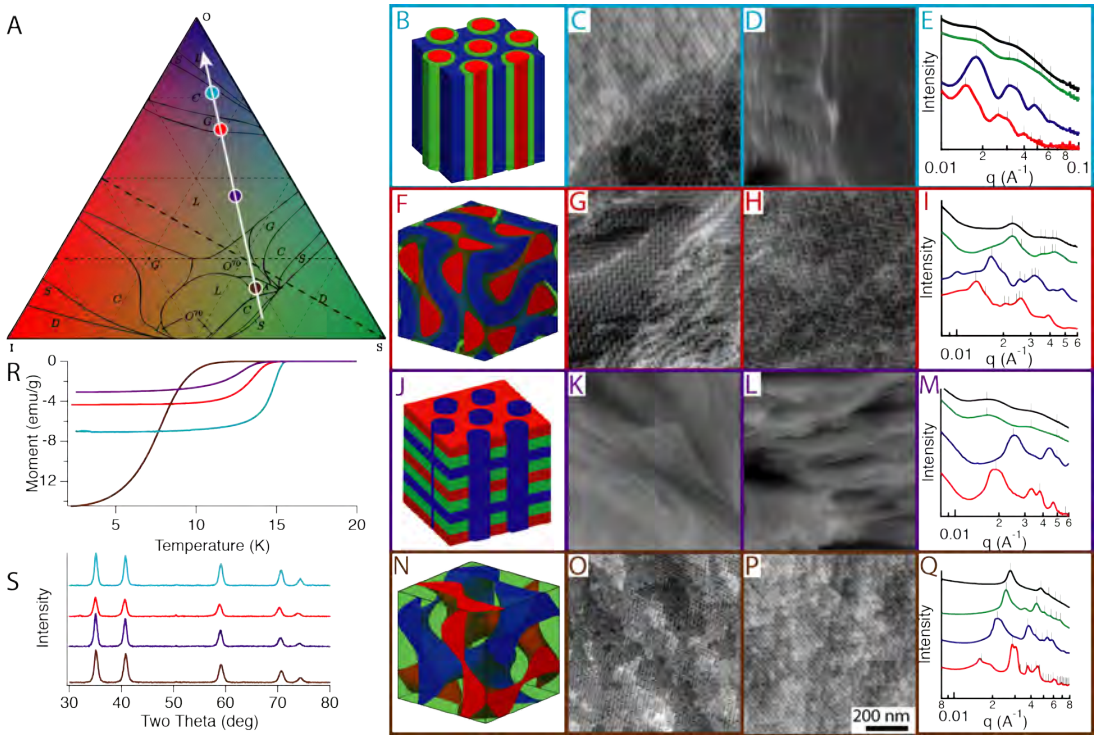

Figure 4.3: Block copolymer morphology tuning in niobium carbonitrides. (A) Simulated phase diagram for isoprene-b-styrene-b-ethylene oxide (ISO) triblock terpolymers (modified from (*17*)). The isopleth highlighted by the white line corresponds to the ISO-83 terpolymer used here, with the base of the isopleth at the neat polymer volume fractions and the brown, purple, red, and teal markings indicating the positions of the alternating gyroid, lamellar, double gyroid matrix, and hexagonal morphologies. (B,F,J,N) Renderings of the target morphology, where the blue domain is the PEO+Nb_2O_5 component retained during thermal processing (C,G,K,O) Scanning electron micrographs (SEMs) of 700 ˚C nitrides of each morphology (D,H,L,P) SEMs of 1000 ˚C carbides with each morphology. (E,I,M,Q) Small-angle X-ray scattering (SAXS) patterns of each morphology as it progresses

through heat treatment, from bottom to top in each frame: polymer-oxide hybrid, freestanding oxide, nitride, and carbide. Ticks indicate the expected peak positions for the targeted mesoscale lattice with lattice parameters given in Table 4.S1. (R) Temperature-dependent magnetization of structured carbides showing a clear superconducting transition beginning at temperatures between 12 K and 16 K for the various morphologies. (S) X-Ray Diffraction Patterns of structured carbides showing the phase-pure rocksalt NbC structure.

Based on this unexpected morphology-T_c correlation, the field-dependent magnetization of the double-gyroid sample was measured at a temperature of 2 K (ca. 0.15 T_c, Figure 4.4). In contrast to field-dependent magnetization measurements at 7 K (ca. 0.5 T_c) which have a typical hysteretic behavior, the 2 K measurement exhibits abrupt jumps in the magnetization during the field sweep. These jumps are comparable in overall behavior to flux avalanches(*6, 18*), but have several striking differences. First, the avalanches occur at incoherently uniform spacing from very low field (ca. 1 kOe) to the highest field measured (40 kOe). Second, the avalanches have nearly constant beginning and ending magnetizations. Finally, the magnitude of the magnetization remains relatively constant throughout the entire region scanned. While definitively or even conclusively assigning such an incoherent behavior to a physical phenomenon would require extensive modeling, we believe that these three atypical features point to a unique means of flux inclusion into the material consistent with an interpretation of the thermomagnetic (TM) model for flux avalanche initiation and propagation in a porous, bulk solid(*19, 20*). In brief, the TM model describes flux

jumps resulting from local Joule heating of the superconductor at a defect site coupled with slow heat transfer out of the material due to a very low temperature (where electronic heat conduction modes are “frozen out”) and the material geometry and properties. In the case of this gyroidal superconductor, we suspect that a circulating supercurrent through the material struts eventually migrates to a strut with a defect – high angle grain boundary, an off-stoichiometry grain, etc. This material locally heats, becomes non-superconducting, and allows flux into not only the strut but also the adjacent, now unshielded, pore volume. This simple conceptual model, while not quantitatively provable or disprovable with the current evidence, explains the flux jumps’ consistent magnitude, their quasi-periodicity, and their presence to high field.

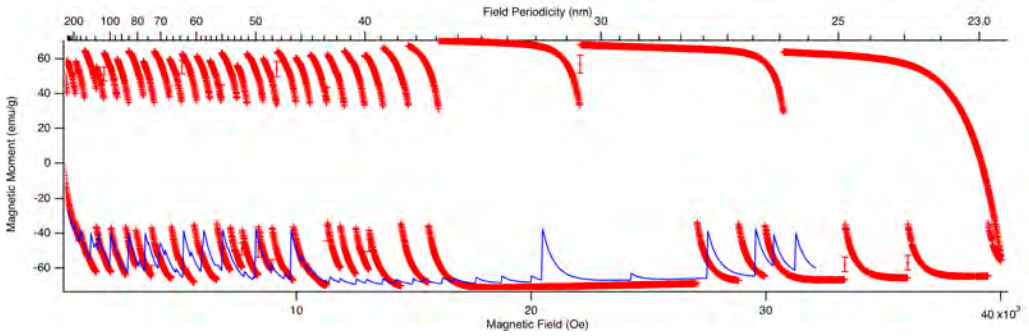

Figure 4.4: Field-dependent magnetization of a double-gyroid matrix carbonitride showing high-field flux avalanches. Red and blue traces are successive replicate measurements on the same sample, showing that the position of the flux jumps is not systematically reproduced. The top axis reflects the field in units of the density of magnetic flux quanta at that field. The combination of the avalanches’ incoherent spacing and the lack of unique or pronounced changes as the field matches the mesoscale repeat suggests that this effect cannot be explained merely as flux pinning on the mesoscale lattice.

Conclusion

Despite substantial promise for the realization of yet-unexplored structure-property correlations, the convergence of block copolymer-inorganic hybrid co-assembly and quantum materials (e.g. correlated electron systems) remains elusive. This gap is largely due to a lack of synthetic approaches to produce mesostructured, electronic-grade materials from block copolymers. In this work, we use systematic variation of high-temperature annealing conditions to discover a route to niobium carbonitrides from block copolymer-derived niobium oxides and nitrides. The resulting materials have superconducting transition temperatures as high as 16 K, doubling the previous record for block copolymer-derived mesoporous superconductors. To demonstrate the robust, tunable nature of this synthesis, we synthesize four different ordered morphologies from a single parent triblock terpolymer. Remarkably, the T_c of the materials varies systematically with the overall oxide loading, suggesting a confinement- or mesostructure-driven effect, and the double-gyroid sample exhibits unexpected flux jumps possibly consistent with strut-by-strut infiltration of the porous mesostructure. We expect that this design strategy for superconductors with controlled, high quality mesoscale order will prove to be a robust platform for studies of mesostructure-property correlations in superconductors and other quantum materials.

Acknowledgements

We thank Jörg G. Werner for kind assistance with graphics and R. Bruce van Dover and Ethan M. Susca for helpful discussions. PAB was supported by the National Science Foundation (NSF) Graduate Research Fellowship Program under grant

number DGE-1650441. This work made use of the Cornell High Energy Synchrotron Source (CHESS) which is supported by the NSF under award DMR-1332208, and the Cornell Center for Materials Research shared facilities which are supported by the NSF MRSEC program (DMR-1719875).

Materials and Methods

Materials

All reagents were purchased from Sigma-Aldrich and used as received unless otherwise noted. Benzene was purchased from TCI America and vacuum-distilled from n-butyllithium before use. Isoprene and styrene were vacuum-distilled from n-butyllithium and calcium hydride, respectively, before use. Tetrahydrofuran (inhibitor free) used for polymer synthesis was purchased from Fisher Scientific and vacuum-distilled from n-butyllithium before use. Methanol and chloroform were purchased from Avantor Performance Materials. Tetrahydrofuran for self-assembly was purchased from Sigma-Aldrich and used as received. Hydrochloric acid (37 wt%) was purchased from Fisher Scientific. Niobium (V) ethoxide (99.999% metals basis) was purchased from Alfa Aesar. Ammonia (electronic grade, 99.9995%) was purchased from Matheson Tri-Gas or Praxair based on availability; no differences were observed between the two suppliers. Argon (ISP grade), forming gas (certified standard), carburizing gas (certified standard), and air (Ultra Zero grade) were purchased from Airgas.

Methods

Polymer Synthesis. The poly(isoprene-b-styrene-b-ethylene oxide) (ISO) triblock terpolymer used was synthesized by sequential anionic polymerization using known techniques(*21*, *22*). In brief, isoprene polymerization was initiated in benzene by sec-butyllithium. Styrene was then added after at least 8 h. After at least 8 h, one molar equivalent of ethylene oxide gas was double-distilled and added, followed by termination of the polymer with methanolic HCl. The resulting methoxy-terminated poly(isoprene-b-styrene) was redissolved in chloroform, washed with water, and precipitated into cold methanol before drying for at least 5 d at 130 ˚C on a high vacuum line. Tetrahydrofuran was then vacuum-distilled onto this polymer, which was re-initiated with potassium napthalenide before the addition of a quantitative amount of ethylene oxide monomer. The termination, washing, and precipitation steps were then repeated and the resulting ISO characterized by a combination of size exclusion chromatography and 1H nuclear magnetic resonance. The polymer had a dispersity of 1.09 and an overall molar mass of 86 kDa with 29.1 vol% PI, 64.4 vol% PS, and 6.5 vol% PEO.

Mesoporous Niobium (V) Oxide and Niobium Nitride Synthesis. The ISO triblock terpolymer was used to prepare mesostructured niobium (V) oxide and niobium nitride following previously reported procedures. Briefly, a stock solution of Nb_2O_5 nanoparticles was prepared via an acid-catalyzed sol-gel method in tetrahydrofuran. Predetermined amounts of the stock solution were added to solutions of the block copolymer (75 mg / 2 mL THF) to give the desired morphology: 0.247 mL for the alternating gyroid strut samples shown in Fig. 4.2 and Fig. 4.3 O,P,Q; 0.401 mL for the perforated lamellar samples shown in Fig. 4.3 K,L,M; 0.958 mL for the double-

gyroid matrix samples shown in Fig. 4.3 G,H,I; 1.058 mL for the hexagonal cylinders samples shown in Fig. 4.3 C,D,E. Volume fractions shown in Fig. 4.3A were determined by assuming 100% incorporation of the sol-gel oxide into the final nanocomposite and assuming a density of 2 g cm^{-3} for the alternating gyroid sample and 0.52 g cm^{-3} for all other samples in the hybrid state. These densities are dramatically lower than the literature value of 4.6 g cm^{-3} for bulk Nb_2O_5(*23*), but well within the expected range for fractal aggregates (*24*). We suspect that the lower density needed at high oxide loading reflects a combination of a shift in the effective Flory-Huggins interaction parameter of the PEO+oxide phase with the other components at high oxide loadings and possible crosslinking of the oxide component during the evaporation and self-assembly process, enhanced by the higher volume fraction of oxide particles. After sol addition, the solutions were allowed to evaporate under a glass dome at 35 ˚C until dry. The resulting films were then annealed at 130 ˚C under vacuum. The block copolymer was then removed by calcination at 450 ˚C for 3h (heating ramp rate 1 ˚C min^{-1} and ambient cooling) to give freestanding oxide. These oxides were then treated in flowing ammonia gas at 700 ˚C for 12 h (heating ramp rate 5 ˚C min^{-1} and cooling 25 ˚C min^{-1}) to give a niobium oxynitride.

Solid State Synthesis. The reactions described in Fig. 4.1 were performed in a Lindberg model 55035 tube furnace equipped with a custom gas switching manifold and 1” quartz tube. The sample to be treated was placed in a quartz crucible (Technical Glass Products) and the tube ends sealed to the gas system. The gas was flowed during the entire duration of furnace heating and cooling at 10 L hr^{-1}. After cooling, argon was flowed over the sample at a rate of 20 L hr^{-1} for two hours,

followed by flowing dry air at a rate of 20 L hr^{-1} for one hour. This final step was intended to controllably grow a dense surface oxide layer rather than a porous layer which may form on exposure to humid air during sample removal. After synthesis, samples were stored in a nitrogen-purged, light-free dessicator cabinet to minimize environmental degradation. No degradation was observed in samples stored in air, though systematic studies of this behavior were not undertaken.

Scanning Electron Microscopy. Scanning electron micrographs were captured using a Tescan Mira microscope operating at an accelerating voltage of 5 kV and using an in-lens secondary electron detector. Samples were fractured on carbon tape and sputter coated with Au-Pd to reduce charging prior to imaging.

X-Ray Diffraction. XRD/WAXS patterns were collected on either a Rigaku Ultima IV equipped with a Cu tube operated at 40 kV and 50 mA and a D/max Ultra strip detector, or a Bruker D8 Advance Eco equipped with a 1 kW Cu tube and a 160-channel Si strip detector. Scan rates were between 2 deg. min^{-1} and 5 deg min^{-1} depending on the quantity of sample available and observed signal to noise ratio. Reported lattice parameters were determined by averaging Gaussian fits to the five observed peaks consistent with the rocksalt (Fm3m) structure, while coherent scattering domain sizes were determined using the Debye-Scherrer equation with a shape factor of 0.9.

Small Angle X-Ray Scattering. SAXS patterns were collected either at station G1 of the Cornell High Energy Synchrotron Source (all patterns except the forming gas-treated sample in Fig. 4.1b) or on a home-built beamline. The apparatus at CHESS consisted of a standard three-slit setup used to collimate the beam to a 0.25 x 0.25 mm

rectangle, an evacuated sample-to-detector distance of typically 2 m, and a Dectris EIGER 1M pixel-array detector. The home-built setup consisted of a Rigaku rotating anode source, a set of orthogonal Franks focusing mirrors, a sample-detector distance of ca. 88 cm, and a phosphor-coupled CCD described in detail elsewhere.

Vibrating Sample Magnetometry. VSM data were collected using a Quantum Design Physical Property Measurement System equipped with a 9 T superconducting magnet and a liquid helium cryostat. Samples were mounted in polypropylene capsules inside a brass half-tube mounted on the VSM transport head and zero-field-cooled to 2 K. A small field of either 50 or 100 Oe was applied and the sample position determined by scanning the transport through its travel, then the sample was warmed at 0.2 K min^{-1} while continuously measuring the magnetic moment until a temperature of 20 K was reached. The sample was then either warmed and removed or the field switched off and the sample re-cooled for further measurements.

REFERENCES

1. K. Hur *et al.*, *Angew. Chemie - Int. Ed.* **50**, 11985–11989 (2011).
2. M. Fruchart *et al.*, *Proc. Natl. Acad. Sci. U. S. A.* **115**, E3655–E3664 (2018).
3. K. Hur, R. G. Hennig, U. Wiesner, *J. Phys. Chem. C.* **121**, 22347–22352 (2017).
4. E. Bousquet *et al.*, *Nature*. **452**, 732–736 (2008).
5. L. Piraux, X. Hallet, *Nanotechnology*. **23**, 355301 (2012).
6. M. Motta, A. V. Silhanek, W. A. Oritz, in *Oxford Handbook of Small Superconductors* (2018), pp. 379–414.
7. M. Templin, *Science.* **278**, 1795–1798 (1997).
8. K. W. Tan *et al.*, *Science.* **349**, 54–58 (2015).
9. S. W. Robbins *et al.*, *Sci. Adv.* **2**, e1501119 (2016).
10. P. A. Beaucage, E. M. Susca, S. M. Gruner, U. B. Wiesner, *Chem. Mater.* **29**, 8973–8977 (2017).
11. J. Lee *et al.*, *Nat. Mater.* **7**, 222–228 (2008).
12. R. Shipra, N. Kumar, A. Sundaresan, (2013), doi:10.1016/j.matchemphys.2013.01.048.
13. S. P. Chockalingam, M. Chand, J. Jesudasan, V. Tripathi, P. Raychaudhuri, *Phys. Rev. B.* **77**, 214503 (2008).
14. N. Pessall, R. E. Gold, H. A. Johansen, *J. Phys. Chem. Solids.* **29**, 19–38 (1968).
15. F. Schüth, R. Palkovits, R. Schlögl, D. Su, *Energy Environ. Sci.* **5**, 6278 (2012).
16. V. L. S. T. Silva, M. Schmal, S. T. Oyama, **182**, 168–182 (1996).

17. Christopher A. Tyler, Jian Qin, and Frank S. Bates, D. C. Morse*, (2007), doi:10.1021/MA062778W.

18. I. A. Rudnev, D. V Shantsev, T. H. Johansen, A. E. Primenko, *Appl. Phys. Lett.* **87**, 42502 (2005).

19. R. G. Mints, A. L. Rakhmanov, *Rev. Mod. Phys.* **53**, 551–592 (1981).

20. P. S. Swartz, C. P. Bean, *J. Appl. Phys.* **39**, 4991–4998 (1968).

21. Travis S. Bailey, Cordell M. Hardy, I. and Thomas H. Epps, F. S. Bates*, (2002), doi:10.1021/MA011716X.

22. M. Stefik *et al.*, *Chem. Mater.* **21**, 5466–5473 (2009).

23. Springer Materials, in *Non-Tetrahedrally Bonded Binary Compounds II* (Springer-Verlag, Berlin/Heidelberg), pp. 1–4.

24. J. Gregory, *Water Sci. Technol.* **36**, 1–13 (1997).

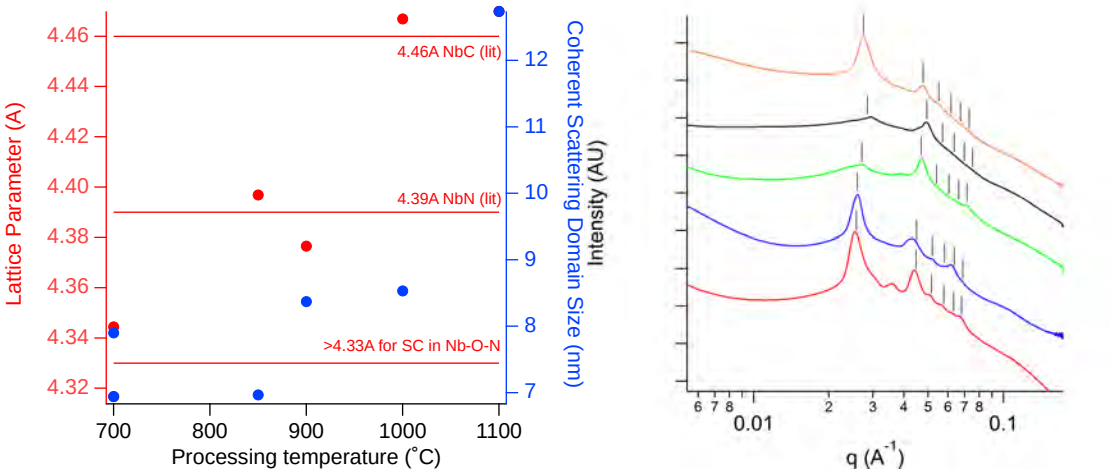

Figure 4.S1: (A) Analyzed XRD data and (B) SAXS patterns from starting nitride and carbonitrides treated under carburizing gas at temperatures of (bottom to top) 700 ˚C, 850 ˚C, 900 ˚C, 1000 ˚C, and 1100 ˚C (no SAXS data available). A smooth progression in lattice parameter is observed with minimal coherent scattering domain growth between 700 ˚C and 1000 ˚C. At 1100 ˚C, the domains are observed to grow dramatically , presumably correlating with loss of the mesostructure.

Table 4.S1: Morphology/Space Group and Lattice Parameter for Peak Markings in Figure 4.3

Morphology	**Processing Stage**	**Space Group Marked**	**d_{100} spacing Marked**
Alternating Gyroid	Hybrid	$I4_132$	54 nm
Alt. Gyroid	Oxide	$I4_132$	41 nm
Alt. Gyroid	Nitride	$I4_132$	35 nm
Alt. Gyroid	Carbide	$I4_132$	32 nm
Perforated Lamellae	Hybrid	Layer grp. p-1	33 nm
Perf. Lam.	Oxide	p-1	25 nm
Perf. Lam.	Nitride	p-1	38 nm
Perf. Lam.	Carbide	p-1	38 nm
Double Gyroid	Hybrid	Ia3d	82 nm
Dbl. Gyroid	Oxide	Ia3d	65 nm
Dbl. Gyroid	Nitride	Ia3d	48 nm
Dbl. Gyroid	Carbide	Ia3d	48 nm
Hexagonal Cylinders	Hybrid	P6	42 nm
Hex. Cyl.	Oxide	P6	35 nm
Hex. Cyl.	Nitride	P6	35 nm
Hex. Cyl.	Carbide	P6	35 nm

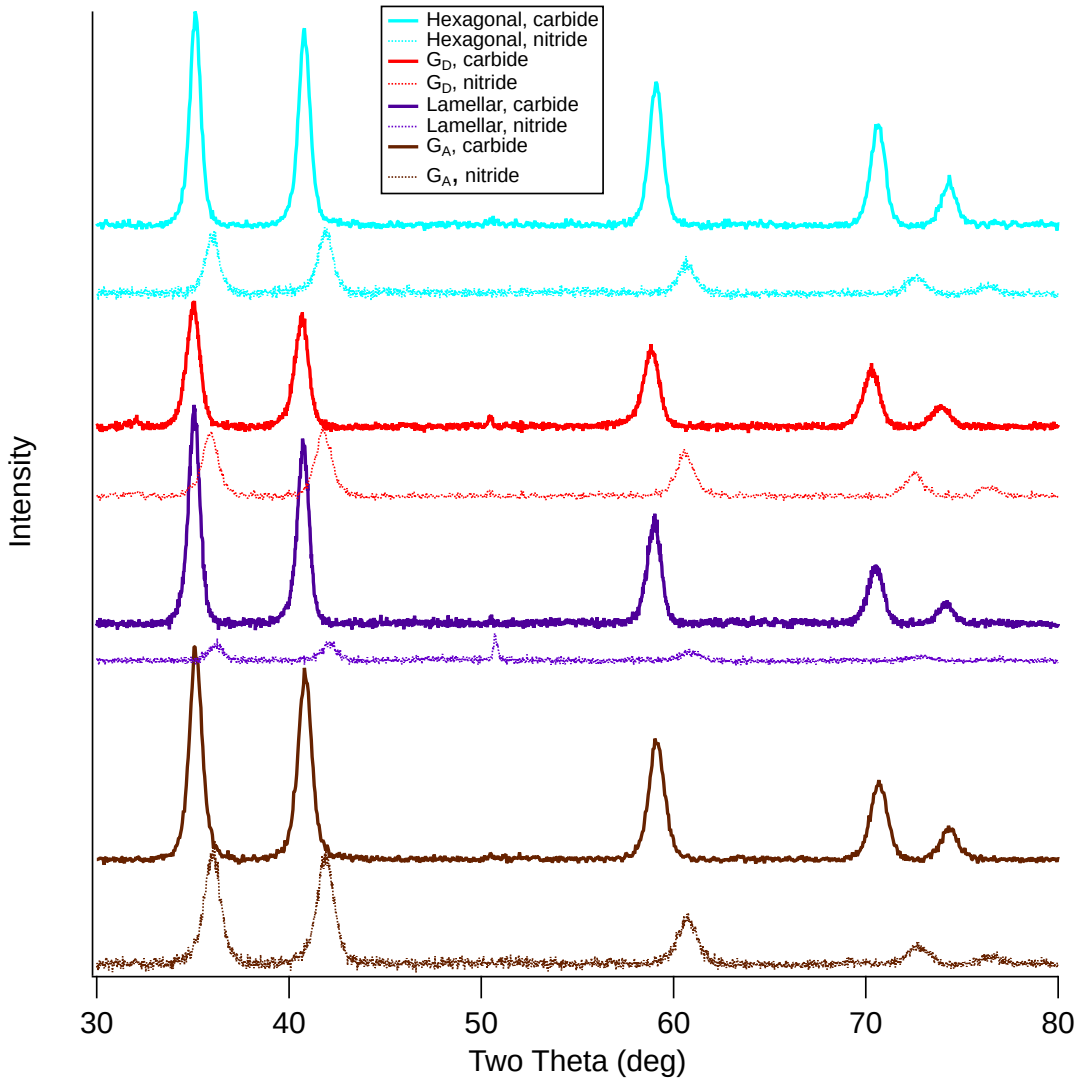

Figure 4.S2: X-Ray Diffraction Patterns for Intermediate Nitrides.

Table 4.S2: Lattice Parameters and Domain Sizes for Nitrides and Carbides

Morphology	**Processing Stage**	**Lattice Parameter (A)**	**Coherent Scattering Domain Size (nm)**
Alternating Gyroid	Nitride	4.31 A	7.6 nm
Alt. Gyroid	Carbide	4.41 A	9.2 nm
Perforated Lamellae	Nitride	4.30 A	7.4 nm
Perf. Lam.	Carbide	4.42 A	10.4 nm
Double Gyroid	Nitride	4.32 A	8.2 nm
Dbl. Gyroid	Carbide	4.43 A	9.6 nm
Hexagonal Cylinders	Nitride	4.31 A	8.7 nm
Hex. Cyl.	Carbide	4.42 A	10.8 nm

Figure 4.S3: Comparison of Tc and Structural Parameters in Mesostructured Carbonitrides.

CHAPTER 5

DISCOVERING ROUTES TO ROOM TEMPERATURE δ-BI_2O_3 ION CONDUCTORS FROM TIME-TEMPERATURE QUENCH MAPS[4]

Abstract

Devices using oxygen-ion conductors (OICs), including oxygen-ion batteries, solid oxide fuel cells, and oxide-based oxygen sensors, are typically limited to temperatures above 300˚C due to low conductivities. One OIC, the δ-phase of Bi_2O_3, has exceptionally high oxygen-ion conductivities above 650˚C. Its predicted outstanding room temperature conductivity has never been realized due to phase transformations that occur during conventional temperature quenches. Utilizing a high throughput laser annealing technique to map quench rates 5-8 orders of magnitude faster than previously possible, here we have successfully quenched δ-Bi_2O_3 to room temperature resulting in films with few structural defects, and device conductivities several orders of magnitude higher than from previous best-in-class materials. The high-resolution/throughput phase mapping and OIC material described here hold substantial fundamental as well as technological promise.

Introduction

An absence of highly oxygen-ion conductive materials at low temperatures has limited the application of rechargeable oxide batteries, solid oxide fuel cells, oxygen pumping

[4] R.T. Bell, M.J. Murphy, P.A. Beaucage, U.B. Wiesner, R.B. van Dover, M.O. Thompson, *in revision*

devices, and oxide-based oxygen sensors to temperatures above ~300˚C (*1–4*). The *δ*-phase of Bi_2O_3 is one of the best oxygen-ion conductors when stable above 729˚C, but transforms during conventional cooling into polymorphs with substantially lower conductivities (*5, 6*). Even best-in-class oxygen-ion conductors (*3, 7–9*) extrapolated to room temperature have conductivities orders of magnitude lower than expected for *δ*-Bi_2O_3 (*3, 10, 11*).

A range of approaches have been attempted to preserve or duplicate the high oxygen-ion conductivity of *δ*-phase Bi_2O_3 at low temperatures. Direct quenching of the *δ*-phase from high temperatures has been explored at quench rates up to 10˚C min^{-1} (*6, 12*), but always resulted in transformation below 600˚C to either the low temperature stable *α*-phase or metastable *β* or *γ*-phases, all with substantially lower conductivities (*4–6, 12*), leading to the general consensus that thermal quenching of *δ*-Bi_2O_3 to room temperature is impossible (*13, 14*). Stabilization of the *δ*-phase by alloying with heavy metals has been demonstrated (*4, 7, 9*), but results in dramatically reduced low temperature oxygen-ion conductivities compared to pure *δ*-Bi_2O_3. Direct low-temperature synthesis of *δ*-Bi_2O_3 has been reported using a variety of synthesis techniques (*7, 11, 15, 16*), but have not included conductivity measurements of *δ*-Bi_2O_3 below 350˚C (*11*), likely due to poor film quality or phase purity. We speculate that such issues have also prevented the application of room temperature *δ*-Bi_2O_3 in devices.

We report here the nucleation and quenching of *δ*-Bi_2O_3 to room temperature using lateral gradient laser spike annealing (lgLSA) (*17*); lgLSA accesses heating and quenching rates up to millions of degrees Celsius per second, orders of magnitude

faster than conventional techniques (*6, 12*), by limiting annealing durations to micro- to milliseconds (*17*). The unique capabilities of laser annealing have been applied for decades in the semiconductor industry to activate dopants (*18, 19*) and more recently to control phase changes (*20, 21*) and nano-confined crystal growth (*22, 23*). However, rapid screening of laser annealing times and temperatures has only recently been enabled by the development of the lgLSA technique (*17*) which combines spatial gradients of peak temperature across single laser scans (Fig. 5.1A) with variable dwell time, enabling the creation of a broad array of peak temperature and time annealing conditions. We measured lgLSA-prepared samples with spatially resolved synchrotron X-ray diffraction to enable the systematic high-throughput exploration of phase behavior as a function of annealing conditions between room temperature and 900˚C (above the 830˚C equilibrium melting point) and dwell times between 0.15 – 10 ms (peak quench rates between 10^4 and 10^6 ˚C s^{-1}, Fig. 5.1B,C), a regime well beyond that previously explored for Bi_2O_3 by any other method. By starting with amorphous Bi_2O_3, which has the extremely high free energy of a “frozen liquid”, the driving force for nucleating an initial crystalline phase is much larger than the driving force for subsequent crystal-crystal transformations, allowing the limited kinetics of a short anneal to capture even the first nucleated phases. For anneals exceeding the melting temperature, the anneal erases as-deposited film defects (Fig. 5.1D), leading to pinhole-free films required for device applications and providing a great deal of flexibility for post-processing, regardless of the deposition method.

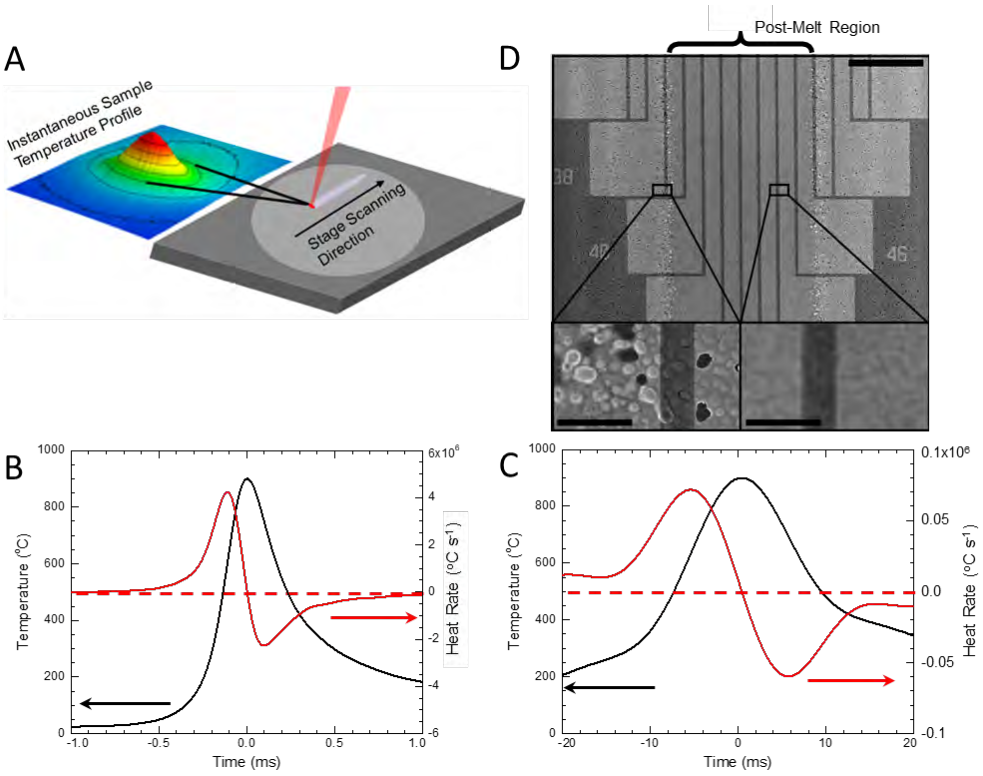

Figure 5.1: Laser spike annealing of Bi_2O_3. (**A**) Illustration of lgLSA scan over a sample and instantaneous temperature profile. (**B,C**) Time, temperature, and heating rate profiles for a 0.15 ms (B) and 2 ms (C) dwell anneal with peak temperatures of 900˚C and peak quench rates of ~$2x10^6$ ˚C s^{-1} (B) and ~$7x10^4$ ˚C s^{-1} (C). (**D**) SEM of electric contacts patterned on top of 1 ms dwell annealed Bi_2O_3 film showing the pinhole-free post-melt region in the center bounded by regions with peak temperature below the melt on either side of the center (scalebar 100 µm). Insets are magnified views of both post-melt and sub-melt regions (scalebars 10 µm).

Mapping Phase Formation

Phase development across lgLSA temperature gradients was determined using spatially resolved X-ray diffraction (Fig. 5.2A). Spatial maps (Fig. 5.2B) of diffraction patterns for dwells of 0.25, 2, and 10 ms show the transition from amorphous at low peak temperatures (edges) to crystalline at higher temperatures (centers). Peak-splitting at 2, 2.3, and 3.8 $Å^{-1}$ indicates formation of multiple phases as a function of peak temperature and dwell. In the case of 2 ms and 10 ms anneals, damage is observed at the highest peak temperatures. Characteristic diffraction patterns for α, β, and δ (shown for two regions, δ_S and δ_L) are given in Figure 5.2C. The contribution of each phase to the measured diffraction was identified as a function of position (Fig. 5.2D) and peak temperature (Fig. 5.2E).

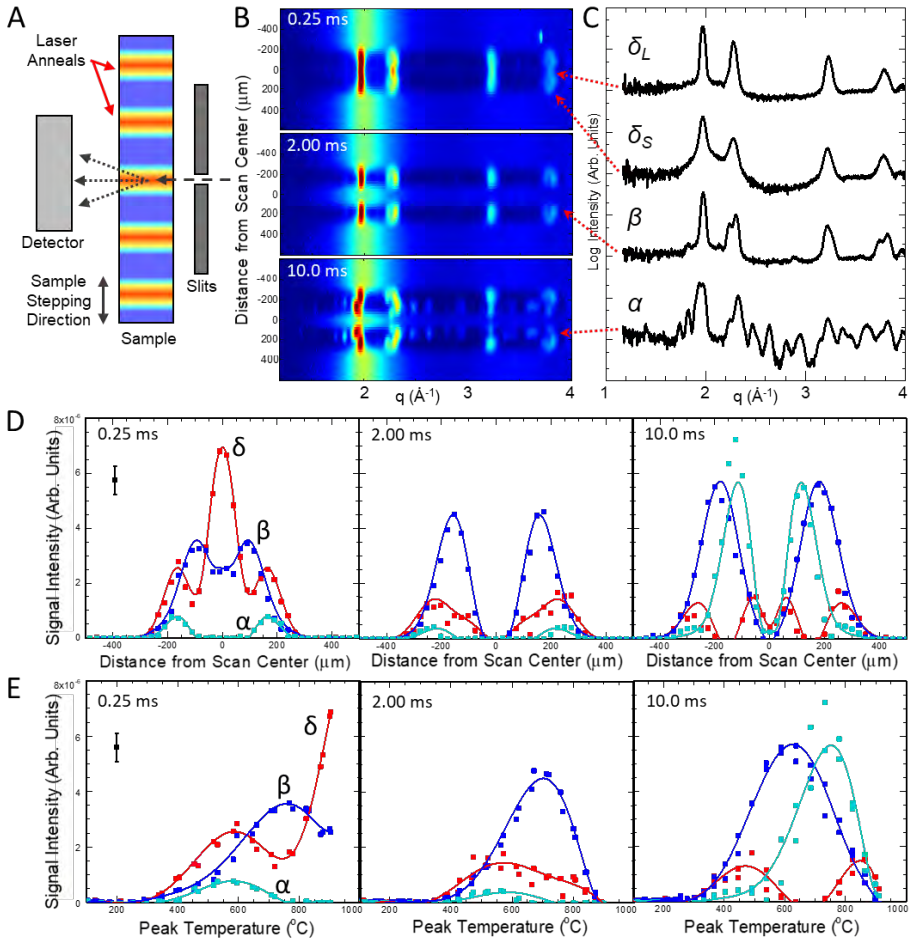

Figure 5.2: Mapping spatial and temperature dependent phase formation for different annealing dwell times. (**A**) Schematic showing X-ray micro-beam mapping of laser annealed sample. The incident X-ray beam (dashed, 25 μm wide after slits) is parallel to the laser annealed regions. Diffraction patterns are taken across varying peak temperature and dwell conditions as the sample is stepped. (**B**) Heat maps of diffraction intensity, I(q), as a function of spatial location across lgLSA scans for dwells of 0.25, 2.00, and 10.0 ms with 900˚C peak temperatures in the scan centers. (**C**) Diffraction patterns for

resultant δ (cubic; nucleated by liquid→solid, δ_L, and solid→solid, δ_S, transformations), β (tetragonal), and α (monoclinic) phases with arrows marking their location in (B). (**D**) Relative diffraction intensities for δ (red), β (blue), and α (teal) phases across each lgLSA scan in (B). A typical least-squares fitting error bar is shown in black in the 0.25 ms figure. Solid lines are symmetric fits. (**E**) Intensities from (D) converted from location to calibrated peak temperature.

By identifying the dominant phase for each peak temperature at seven dwells between 0.15 and 10 ms, a temperature-dwell-transformation (TDT) diagram was constructed (Fig. 5.3A). Processing regimes resulting in the same dominant phase are identified. The film remains amorphous for temperatures below 350˚– 400˚C for all dwells investigated. Above these temperatures, the fractional intensity of each phase was mapped (Fig. 5.3B-D). Two δ-phase forming regimes are identified, one for a solid-state transformation (δ_S) in a shrinking temperature window ranging from just above the amorphous transition to 750˚C at 150 μs and 500˚C at ≤ 5 ms, and the other via a melt mediated transformation (δ_L) for temperatures above ~750˚C and dwells below 2 ms. A β-rich region is found between high and low temperature δ-phase regions and extends to 10 ms, and an α-rich region appears at the longest dwells and highest temperatures.

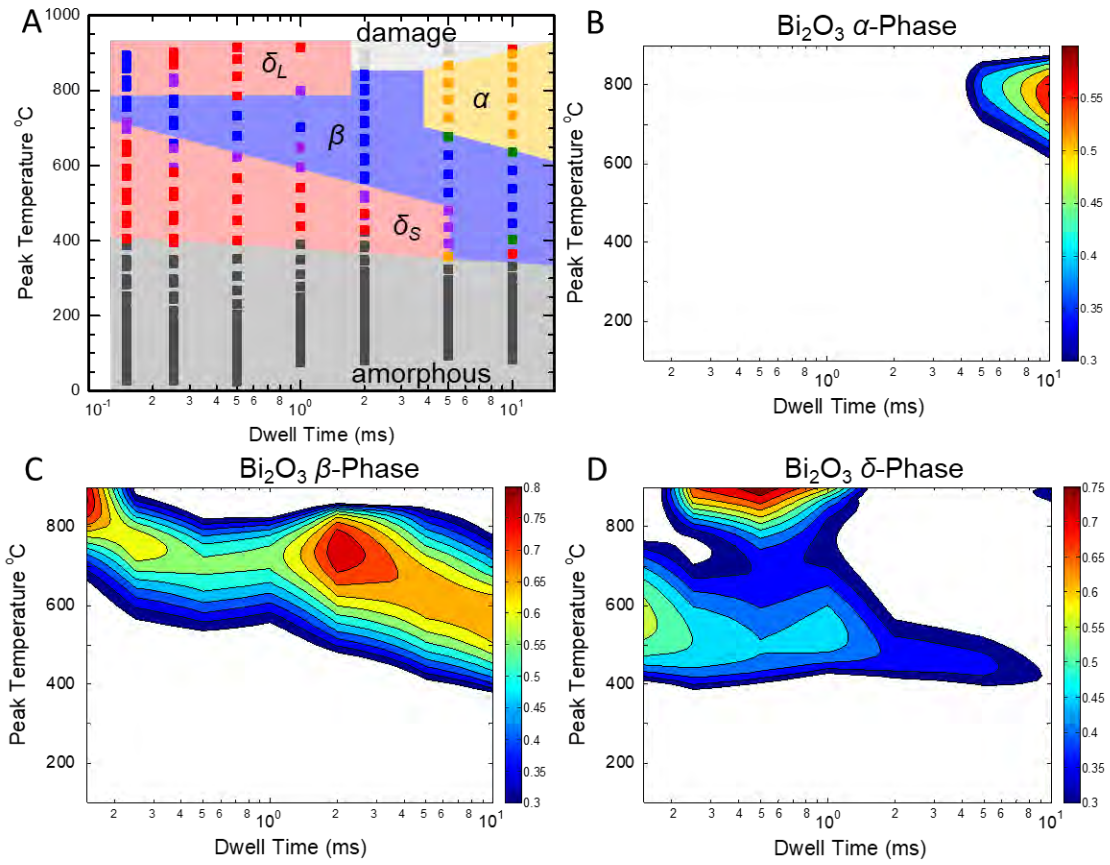

Figure 5.3: Peak annealing temperature and dwell time maps of Bi_2O_3 phases. (**A**) Temperature-dwell-transformation (TDT) diagram displaying the predominant room temperature phase as a function of dwell time and peak temperature: δ red, β blue, α yellow, mixed α/β green, mixed δ/β purple, amorphous dark grey, and damage light grey. Each square is a measured condition and colored regions indicate the approximate processing regimes expected to result in each phase. (**B-D**) Weighted phase fractions of room temperature stable α-phase (B), β-phase (C), and δ-phase (D).

We believe the low temperature δ_S regime is the result of a direct amorphous to δ transformation, as evidenced by a remnant amorphous fraction Bi_2O_3 that appears as a broad peak near 2 $Å^{-1}$ for δ_S shown in Figure 5.2c. Additionally, the lower bound of the high temperature δ_L-region is likely depressed from the 830˚C equilibrium melting point to closer to 750˚C due to a glass to liquid transition of the amorphous precursor. In this δ_L-region, a combination of faster liquid kinetics and nucleation-limited growth (grain growth much faster than nucleation) results in no remnant amorphous peak, high phase purity, and large domains (>100 nm by Scherrer analysis).

These transformation maps suggest that the δ-phase initially nucleates and grows under all the conditions explored, with subsequent solid-phase transformations from δ to β and α phases in specific time/temperature regimes. The presence of an amorphous signal in short dwell δ_S strongly suggests that δ-phase nucleates first in solid state transformations. The β rich region between δ_S and δ_L largely overlaps the temperature region where δ is the equilibrium phase and thermodynamics would favor δ nucleation. While direct β-phase nucleation is impossible to rule out with these ex-situ measurements, this β-rich region is likely the product of an amorphous$\rightarrow\delta\rightarrow\beta$ transformation pathway, as the rapid transformation of $\delta\rightarrow\beta$ at 650˚C has been widely reported in furnace quenches (*6*) and the δ-phase fraction appears to exchange directly with the β-phase at higher temperatures and dwell times (Fig. 5.3C,D). In fact, the continued presence of δ to longer dwells at lower temperatures suggest that the $\delta\rightarrow\beta$ nucleation rate maximum occurs between 550˚C and 650˚C. The presence of a local maximum in β-composition at the shortest dwells and highest temperatures is not fully explained by this model, suggesting that another factor may influence nucleation

under the most extreme conditions. The lack of the very distinct α signal until long times and high temperatures suggests that, despite being the stable phase at temperatures below 730˚C, α does not directly nucleate from the amorphous and is instead produced by an amorphous$\rightarrow\delta\rightarrow\beta\rightarrow\alpha$ transformation pathway. This mirrors the transformation pathway during furnace quenching from high temperature stable δ-phase of $\delta\rightarrow\beta\rightarrow\alpha$ (*4*, *6*). The disappearance of both δ regimes by 10 ms dwells, with quench rates greater than 10^4 ˚C s^{-1}, explains why the quench of the δ-phase has not been previously accomplished by studies using much lower quench rates.

The δ-phase is preserved in melt processed films for dwells up to 1 ms, despite nucleation of β at sub-melt temperatures for dwells as short as 0.15 ms. These results suggest that melt processing substantially lowers the concentration of defects in the Bi_2O_3 film, reducing the number of heterogeneous nucleation sites and subsequently depresses $\delta \rightarrow \beta$ nucleation rates compared to solid state processing. This also suggests that melt produced δ-films may have increased low-temperature stability compared to δ-films produced by other methods.

Ionic Conductivity Measurements

Annealing conditions of 850˚C with 0.25 ms dwell were chosen to create phase-pure, large domain, pinhole free δ-Bi_2O_3 devices (Fig. 5.4A) that enable measurement of the room temperature conductivity. Impedance spectroscopy was used to determine the frequency dependence of the real and imaginary impedance of δ-Bi_2O_3 devices (Fig. 5.4B-D). The conductivity of the δ-Bi_2O_3 layer was determined by fitting a circuit

model (red lines in Fig. 5.4 B-D), yielding a room temperature conductivity of $10^{-5.05\pm0.03}$ S cm^{-1}. This is over 6 orders of magnitude greater than the conductivity of the room temperature stable α-phase ($10^{-11.9}$ S cm^{-1}) (*12*). DC resistance was unmeasurable (beyond the instrumental limit of 1 MΩ), indicating that conduction was most likely mediated by δ-Bi_2O_3 and not through pinholes. These results represent the lowest temperature reported δ-Bi_2O_3 device and conductivity measurements by over 300˚C (*11*).

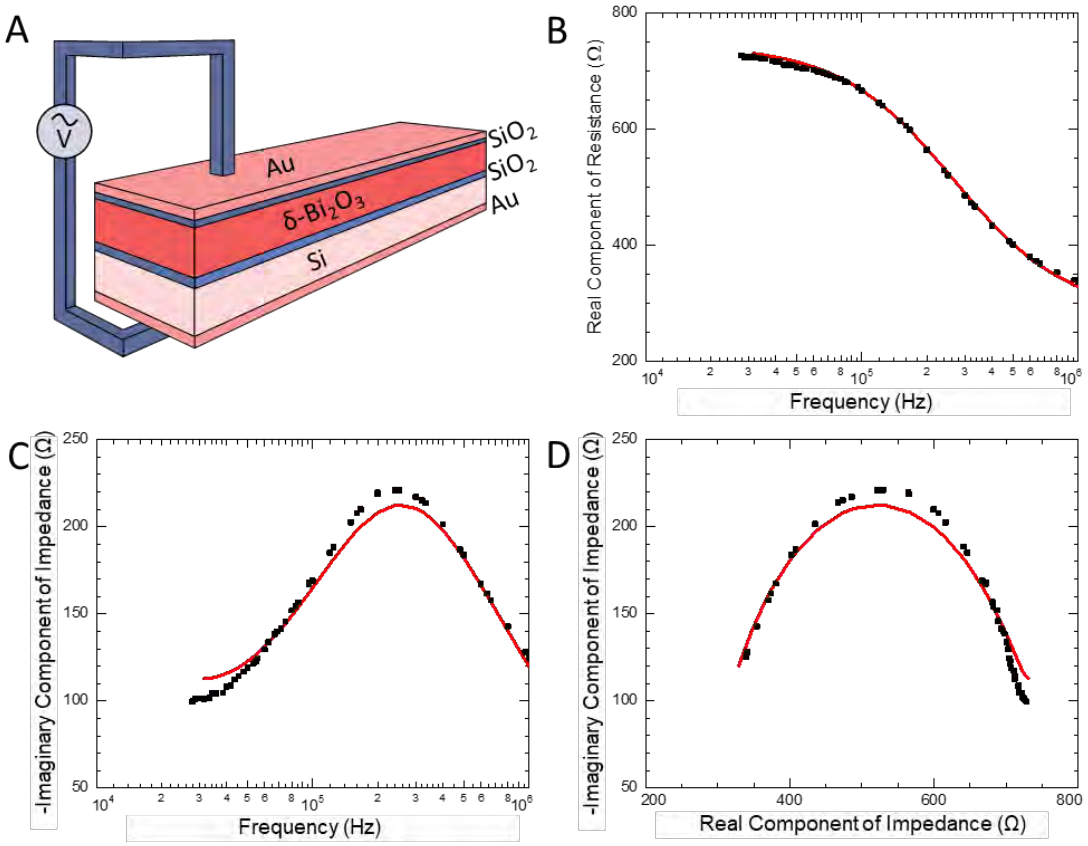

Figure 5.4: Electrical measurements of δ-phase Bi_2O_3. (**A**) Schematic of δ-Bi_2O_3 devices tested via impedance spectroscopy. (**B,C**) Real (B) and imaginary (C) components of impedance as a function of frequency. (**D**) Real vs. imaginary impedance showing a semicircle

shape typical of ionic conductors. Squares are raw data and red lines are derived from modeling the circuit in (A).

The conductivity of ~10^{-5} S cm^{-1} for δ-Bi_2O_3 is orders of magnitude higher than extrapolations to room temperature of any known oxygen-ion conducting material reported to date, including YSZ (10^{-13} S cm^{-1}) (*11*), $Na_{0.5}Bi_{0.5}TiO_3$ (10^{-10} S cm^{-1}) (*8*), Pb and Y stabilized δ-Bi_2O_3 (10^{-8} S cm^{-1}) (*9*), and Er stabilized δ-Bi_2O_3 (10^{-8} S cm^{-1}) (*7*). Extrapolations of pure δ-phase Bi_2O_3 from high temperatures suggest a room temperature conductivity near $10^{-3.6}$ S cm^{-1} (*10*, *11*), still higher than our experimental value. This discrepancy may be due to ordering of the oxygen sublattice, an effect observed to decrease conductivity by ~2 orders of magnitude at temperatures below 600-800˚C for dopant stabilized δ-Bi_2O_3 (*7, 24*). Reports of δ-Bi_2O_3 at 350˚C show no deviations from high temperature extrapolations (*11*), suggesting that the ordering temperature of pure δ-Bi_2O_3 occurs between 25˚C and 350˚C. Measurements of Pb and Y stabilized δ-Bi_2O_3 continue to show oxygen-ion conduction rather than electron conduction after oxygen ordering (*9*); we expect the same to be true for pure δ-Bi_2O_3. Our results on δ-Bi_2O_3 present, by several orders of magnitude, the highest reported room temperature oxygen-ion conductor. The device-grade room temperature δ-Bi_2O_3 may therefore be an enabling material for low temperature oxygen-ion driven sensors, batteries, and other devices previously limited by materials performance. Finally, we expect that time-temperature phase mapping via lgLSA will substantially accelerate metastable phase screening enabling advanced materials discovery and exploration.

Acknowledgements

We thank A. Woll and H. Joress for assistance with equipment for synchrotron diffraction. This work made use of the Cornell Center for Materials Research Shared Facilities which are supported through the NSF MRSEC program (DMR-1719875), the Cornell High Energy Synchrotron Source (CHESS) which is supported by the NSF (DMR-1332208), and the Cornell NanoScale Facility, a member of the National Nanotechnology Coordinated Infrastructure (NNCI), which is supported by the NSF (ECCS-1542081). R.T.B. was supported by the NSF GK12 fellowship program (DGE-1045513) and Kionix fellowship. P.A.B. was supported by the NSF Graduate Research Fellowship Program (DGE-1650441) and by the U.S. Department of Energy, Office of Science Graduate Student Research program (DE-SC0014664). U.W. thanks the U.S. Department of Energy Office of Science, Basic Energy Sciences, under Award No. DE-SC0010560 for support.

Author Contributions

RTB and MJM proposed the study. MJM and RTB designed deposition. MJM deposited samples. RTB designed and ran laser annealing. PAB and RTB designed and ran X-ray experiments. RTB, MOT, and PAB analyzed X-ray data. RTB, MOT, RBVD, PAB, and MJM designed ionic conductivity experiment and equipment. RTB fabricated electrical devices. RTB and MJM measured electrical devices. PAB measured and UW supervised SEM experiments. RTB, MJM, and PAB wrote the manuscript with input from all authors.

Materials and Methods

Deposition. Sample films of Bi_2O_3 were sputtered from a metallic Bi target (>99.99%) using an active plasma of argon and oxygen onto silicon wafers (p type, 0.01 Ω-cm, WRS Materials) with a thermal SiO_2 buffer layer. The substrate was unheated during sputtering, and the as-deposited Bi_2O_3 was amorphous (Fig. 5.S1). The thermal SiO_2 buffer layer between the silicon wafer and Bi_2O_3 was used to prevent melt alloying with the silicon wafer in the center of the laser scans where temperatures exceed the 830˚C Bi_2O_3 melting temperature. Melt alloying of Bi_2O_3 and SiO_2 is known to precipitate a stable body centered cubic bismuth silicate phase with a melting point near 900˚C at low silicon concentrations (*6*, *25*); this phase was not observed for melt anneals in this study. On these time scales, the SiO_2 buffer layer appears to successfully prevent alloying of the Bi_2O_3 films even during melt. Samples used for structural analysis had a 100 nm thermal SiO_2 buffer, while samples used for electrical conductivity measurements had a thinner, 5 nm SiO_2 buffer layer. Production of phase pure δ-Bi_2O_3 in the devices used for electrical measurements was verified by XRD (Fig. 5.S2). After laser annealing and X-ray analysis, and prior to device patterning, an additional 5 nm of SiO_2 was deposited using electron beam evaporation from an SiO_2 target as a capping layer on top of the Bi_2O_3 film. This protected films from solvents during photolithographic patterning of electrical

contacts. Thermal evaporation was used to deposit adhesion layers (1 nm Cr) and gold top and bottom contacts (30 nm).

Laser Annealing. Laser spike annealing was performed by scanning a continuous 10.6 μm wavelength line-focused CO_2 laser (as described previously (*17*)) across the sample, as shown in Figure 5.1a. A measure of annealing duration, the dwell time, is defined as the full width at half maximum (FWHM) of the laser intensity profile in the scanning direction divided by the scanning speed. All anneals were performed in air. Temperature evolution as a function of time across the entire scan width was measured as described previously (*17*). The peak temperature experienced across the laser scan width is approximately Gaussian with a maximum slope of 2˚C μm^{-1} and FWHM of 680 μm. The Bi_2O_3 thickness dependent perturbation to surface temperature was calibrated by Bi_2O_3 and Au dot melts (*17*). Laser scans create a line of annealed material where annealing conditions are invariant along the scan length but vary across the scan width. This allows the use of high aspect ratio rectangular areas for both X-ray diffraction and ion conduction measurements, with large areas of comparable annealing conditions despite the steep temperature gradient across the scan width. On the same sample, multiple separated scans were made with dwells of 0.15 – 10 ms and peak temperatures in the scan centers ~900˚C and center-center separations of 3 mm. This allowed high throughput measurements of annealing times and temperature conditions on a single sample using spatially resolved measurements.

Phase Identification. X-ray diffraction measurements were conducted at station G1 of the Cornell High Energy Synchrotron Source (CHESS). The X-ray beam was reduced to a 25x200 μm rectangle using a standard three-slit setup. The sample was

mounted in a near-grazing-incidence configuration (ω= 3˚) and aligned such that the temperature gradient across the laser scans was orthogonal to the incident beam, allowing diffraction measurements to be spatially indexed to precise temperature (averaging over a 0-50˚C temperature range) and dwell annealing conditions. Diffracted X-rays were collected on a Pilatus3-300K pixel array detector (Dectris, Inc.). The incident beam energy was 9.81 keV and a typical sample-detector distance was 20 cm; the precise sample-detector distance was calibrated using copper tape adhered to each end of each sample. Radial integration was performed using the Nika package for Igor Pro (*26*). An average of the amorphous SiO_2 peak near 3 $\dot{A}^{-1}$ (Fig. 5.S1) was taken and subtracted for all diffraction results on a sample to sample basis to better allow phase identification. The fraction of polymorphs present in each diffraction pattern was determined by multi-peak fitting and scaled relative to phase-pure patterns. For Figure 5.3a, if a single phase has more than 25% higher signal than all other phases it is defined as dominant, if two phases have intensities within 25% then it is mixed phase. Fits in Figure 5.2d were developed using even polynomials which forced symmetry of the fit for equivalent annealing conditions on either side of the laser scan, and were transformed into temperature for Figure 5.2e using lgLSA calibrations. 3D surfaces used to create contour plots in Figure 5.3b-d were developed using fitting shown in Figure 5.2e. The reported limit on coherent scattering domain size was determined by the Debye-Scherrer equation assuming zero instrumental broadening and, as such, represents a lower limit on domain size. Prolonged anneals above the equilibrium melt resulted in damage in the form of an amorphous structure with a shifted amorphous peak compared to the as-deposited amorphous film, likely

due to the well reported instability of Bi_2O_3 in low oxygen partial pressure environments at high temperatures (*7*).

Scanning Electron Microscopy. The morphology of the annealed areas was examined using a Tescan Mira3 scanning electron microscope (SEM) using an in-lens detector and an accelerating voltage of 15 kV. The laser scan image in Figure 5.1d had a 1 ms dwell and 900˚C peak temperature.

Electrical Measurements and Devices. Devices with a Bi_2O_3 contact area of 0.328 mm^2 were constructed on areas of 160 nm thick δ-Bi_2O_3 generated by lgLSA to a peak temperature of 850˚C with a 0.25 ms dwell (Fig. 5.4a). Conductivity was measured by impedance spectroscopy using a 4284A LCR meter (Hewlett-Packard Inc) at frequencies from 25 kHz to 1 MHz at room temperature. The impedance of the Bi_2O_3 layer was extracted by fitting the measured curves using a model consisting of parallel resistor and constant phase element (Bi_2O_3 film) in series with a parallel resistance and capacitance circuit (SiO_2 buffer layers) and series resistor (substrate). Conductivity measurement error was calculated from errors of fit and device dimensions. DC measurements were conducted using handheld multimeters and confirmed by 10 Hz measurements with the 4284A LCR meter.

REFERENCES

1. C. M. Berger *et al.*, Calcium-Iron Oxide as Energy Storage Medium in Rechargeable Oxide Batteries. *J. Am. Ceram. Soc.* **99**, 4083–4092 (2016).
2. N. Mahato, A. Banerjee, A. Gupta, S. Omar, K. Balani, Progress in material selection for solid oxide fuel cell technology : A review. *Prog. Mater. Sci.* **72**, 141–337 (2015).
3. E. D. Wachsman, K. T. Lee, Lowering the Temperature of Solid Oxide Fuel Cells. *Science*. **334**, 935–939 (2011).
4. M. Drache, P. Roussel, J.-P. Wignacourt, Structures and Oxide Mobility in Bi-Ln-O Materials: Heritage of Bi_2O_3. *Chem. Rev.* **107**, 80–96 (2007).
5. R. D. Bayliss, S. N. Cook, S. Kotsantonis, R. J. Chater, J. A. Kilner, Oxygen ion diffusion and surface exchange properties of the α- and δ-phases of Bi_2O_3. *Adv. Energy Mater.* **4**, 1–6 (2014).
6. H. A. Harwig, A. G. Gerards, The polymorphism of bismuth sesquioxide. *Thermochim. Acta*. **28**, 121–131 (1979).
7. S. Sanna *et al.*, Enhancement of the chemical stability in confined δ-Bi_2O_3. *Nat. Mater.* **14**, 500–504 (2015).
8. N. Bi *et al.*, A family of oxide ion conductors based on the ferroelectric perovskite $Na_{0.5}Bi_{0.5}TiO_3$. *Nat. Mater.* **13**, 31–35 (2014).
9. A. Borowska-Centkowska *et al.*, Conductivity in lead substituted bismuth yttrate fluorites. *Solid State Ionics*. **254**, 59–64 (2014).

10. H. A. Harwig, A. G. Gerards, Electrical Properties of the α, ß, γ, and δ Phases of Bismuth Sesquioxide. *J. Solid State Chem.* **26**, 265–274 (1978).

11. K. Laurent, G. Y. Wang, S. Tusseau-Nenez, Y. Leprince-Wang, Structure and conductivity studies of electrodeposited δ-Bi_2O_3. *Solid State Ionics*. **178**, 1735–1739 (2008).

12. F. Schröder, N. Bagdassarov, F. Ritter, L. Bayarjargal, Temperature dependence of Bi_2O_3 structural parameters close to the α–δ phase transition. *Phase Transitions*. **83**, 311–325 (2010).

13. P. Conflant, C. Follet-Houttemane, M. Drache, The Bi_2O_3–Sm_2O_3 System: Phase Diagram and Electrical Properties. *J. Mater. Chem.* **1**, 649–653 (1991).

14. N. A. S. Webster, C. Ling, C. Raston, F. Lincoln, The structural and conductivity evolution of fluorite-type Bi_2O_3–Er_2O_3–PbO solid electrolytes during long-term annealing. *Solid State Ionics*. **179**, 697–705 (2008).

15. J. A. Switzer, M. G. Shumsky, E. W. Bohannan, Electrodeposited Ceramic Single Crystals. *Science*. **284**, 293–296 (1999).

16. T. Takeyama, N. Takahashi, T. Nakamura, S. Itoh, Growth and characterization of high-quality δ-Bi_2O_3 thin films grown by carbothermal evaporation. *Mater. Lett.* **60**, 1733–1735 (2006).

17. R. T. Bell *et al.*, Lateral Temperature-Gradient Method for High-Throughput Characterization of Material Processing by Millisecond Laser Annealing. *ACS Comb. Sci.* **18**, 548–558 (2016).

18. C. W. White, J. Narayan, R. T. Young, Laser Annealing of Ion-Implanted Semiconductors. *Science*. **204**, 461–469 (1979).

19. A. L. Robinson, Laser Annealing: Processing Semiconductors Without a Furnace. *Science*. **201**, 333–335 (1978).

20. J. Orava, A. L. Greer, B. Gholipour, D. W. Hewak, C. E. Smith, Characterization of supercooled liquid $Ge_2Sb_2Te_5$ and its crystallization by ultrafast-heating calorimetry. *Nat. Mater.* **11**, 279–283 (2012).

21. M. Wuttig, N. Yamada, Phase-change materials for rewriteable data storage. *Nat. Mater.* **6**, 824–832 (2007).

22. K. W. Tan *et al.*, Transient laser heating induced hierarchical porous structures from block copolymer-directed self-assembly. *Science*. **349**, 54–58 (2015).

23. H. Arora *et al.*, Block Copolymer Self-Assembly-Directed Single-Crystal Homo- and Heteroepitaxial Nanostructures. *Science*. **330**, 214–219 (2010).

24. S. Boyapati, E. D. Wachsman, N. Jiang, Effect of oxygen sublattice ordering on interstitial transport mechanism and conductivity activation energies in phase-stabilized cubic bismuth oxides. *Solid State Ionics.* **140**, 149–160 (2001).

25. E. M. Levin, R. S. Roth, Polymorphism of bismuth sesquioxide. II. Effect of oxide additions on the polymorphism of Bi2O3. *J. Res. Natl. Bur. Stand. Sect. A Phys. Chem.* **68A**, 197 (1964).

26. J. Ilavsky, Nika: Software for two-dimensional data reduction. *J. Appl. Crystallogr.* **45**, 324–328 (2012).

APPENDIX

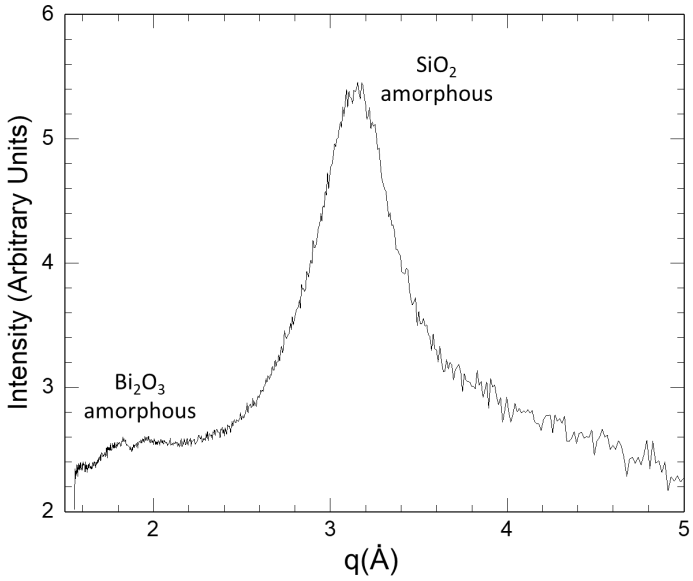

Figure 5.S1. X-ray diffraction pattern of as-deposited Bi_2O_3 on SiO_2 buffer layer on silicon single crystalline wafer.

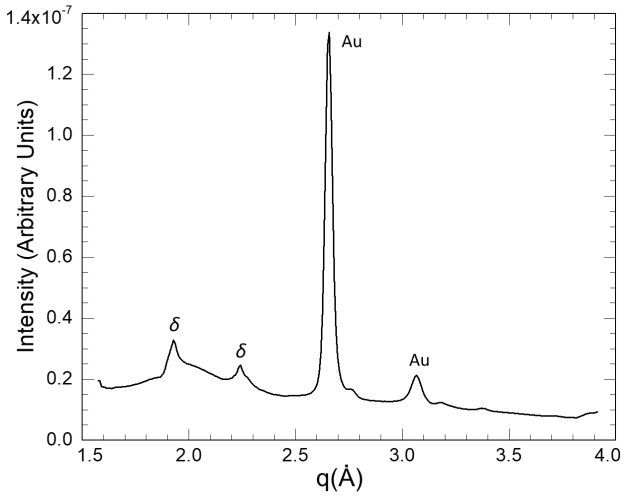

Figure 5.S2. X-ray diffraction pattern of δ-Bi_2O_3 device with Au top contact demonstrating preservation of δ-phase through device patterning.

CHAPTER 6

MESOSTRUCTURED SUPERCONDUCTING INDIUM VIA HIGH-PRESSURE INFILTRATION OF CERAMIC SINGLE MESOCRYSTALS[5]

Introduction

Superconductors with mesoscale order are expected to have a wide variety of emergent electronic and magnetic properties, including directional flux pinning behavior, enhanced upper critical field, and access to "improper" properties disallowed by symmetry. These phenomena have not been extensively experimentally or theoretically explored, however, due to a lack of versatile synthetic approaches that might enable such studies. The only route to such materials that allows facile tuning of morphology and length scale is block copolymer-inorganic hybrid co-assembly. The only route to date to block copolymer-derived SCs, however, involves multistep, high temperature processing to prepare niobium nitrides(*1*) and carbides(*2*). This route, while capable of producing superconductors with reasonable superconducting properties, inherently convolutes the material chemistry (e.g, in simplest form, O/N and N/C ratios) with the mesostructure due to the surface area and chemistry sensitive nature of high temperature gas decomposition and diffusion. This makes direct comparison between one morphology and another, or one length scale or another, essentially impossible. Even comparison to bulk samples, the benchmark for establishing whether an effect is due to mesoscale order, requires completely different

[5] P.A. Beaucage*, R.P. Thedford*, E.M. Susca*, S.M. Gruner, U. Wiesner, *manuscript in preparation*

synthetic pathways from the corresponding mesoscale sample to produce a material with the same chemistry.

Some of the most interesting mesostructure-derived properties in block copolymer-templated superconductors are expected to be highly anisotropic; for example, the different pore projections of the gyroid structure along [111] directions as compared to [100] may lead to unique flux pinning effects. The exploration of these phenomena, however, requires the synthesis of large single crystals and their isolation for single-crystal, angle-dependent measurements. Current oxide-derived syntheses produce mesocrystals with longest dimensions on the order of tens of um, which would require careful focused ion beam nanomachining for isolation of a single crystal domain. Recent developments have resulted in a robust synthetic strategy that produces single crystals of silicon oxynitride (SiON) ceramic with total area up to 14 mm^2 and thickness on the order of hundreds of um, enabling the robust synthesis of bulk single crystals of mesoporous morphologies(*3*). This synthesis cannot be readily expanded to oxides and related materials, however, due to its reliance on a relatively unreactive preceramic polymer as an additive rather than a reactive oxide sol, carbon precursors. Therefore, realization of bulk single crystals of superconductors relies on the infiltration of SiON templates with a compositionally stable additive, e.g. a metal. The high quality templating of bulk metallic materials using block copolymer self-assembly can be considered a grand challenge of the last decade in block copolymer-inorganic hybrid assembly. While remarkable strides have been made toward this goal in the form of incorporation of metallic nanoparticles in a BCP domain (*4*), most approaches have focused on backfilling a BCP-derived porous structure with metal,

primarily by electro- or electroless deposition. Even with this route, careful selection of the electrodeposition chemistry is needed to ensure complete deposition, and to date only a handful of metals including gold, copper, and aluminum have been successfully templated. Even with these constraints, complete and uniform backfilling has only been achieved in thin films.

High pressure infiltration of molten metal into ceramic templates has been used in inverse opal-type templated materials to prepare mesoscale ordered superconductors with periodicities on the micrometer scale(*5*). In this facile route, a robust, periodically ordered template material is placed in a pressure reactor with a metal of interest. The metal is melted by heating the entire reactor, and then a large hydrostatic pressure (several kbar) is applied, forcing the metal to enter the pores. The reactor is then cooled and depressurized, trapping the now-solid metal in the pores of the template (Figure 6.1).

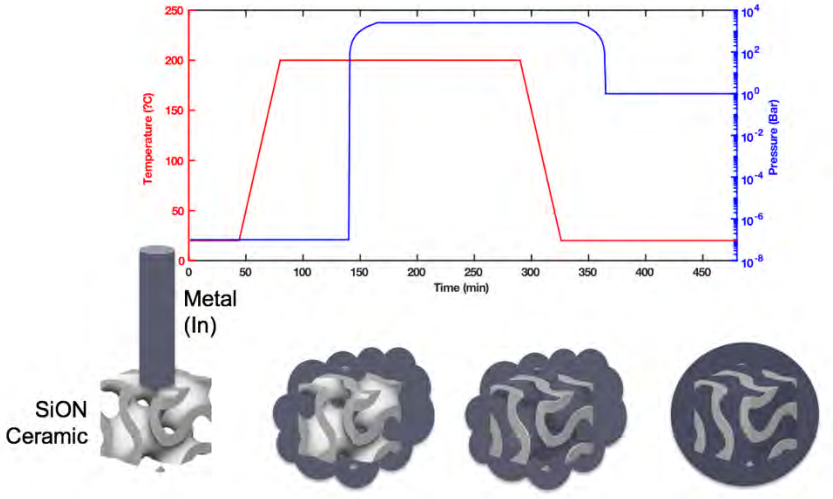

Figure 6.1: Schematic of pressure, temperature, and material state during high-pressure indium infiltration into SiON single mesocrystal templates.

Results

The infiltration of In into the ceramic template was first studied by scanning electron microscopy (SEM) on polished, fractured cross sections of the material (Figure 6.2). It should be noted that high-electron-density regions (such as the In) are brighter than low-electron-density regions (such as the SiON). This measurement revealed a variety of infiltration states across the material, from areas with near-complete In infiltration (right to areas with very little infiltration. Noticeably, areas were observed where only one of the two gyroid networks was filled, a state which should result in a chiral material. It is possible that, e.g. due to surface chemistry variation, one network may have a slightly different pressure to infiltrate than the other, opening the possibility to synthesize chiral materials via careful pressure/temperature control.

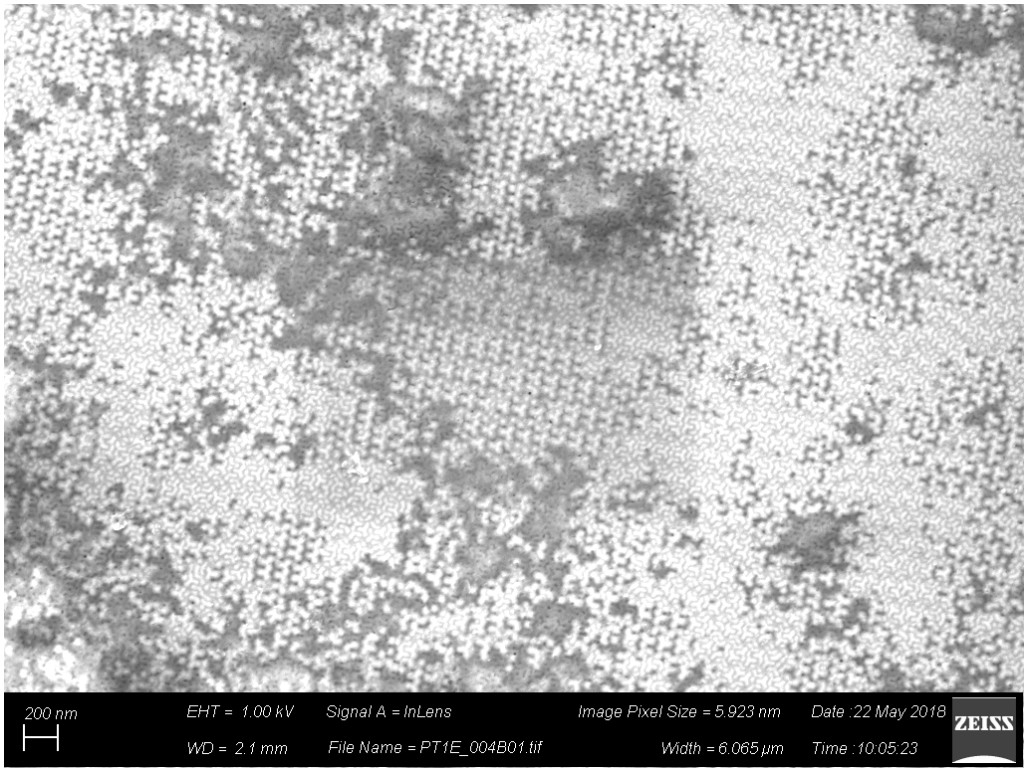

Figure 6.2: Scanning electron micrograph (SEM) of a polished cross section of an indium-infiltrated SiON polycrystal.

To check that the indium remained superconducting, we used magnetic moment vs. temperature (M vs. T) scanning in a vibrating sample magnetometer (VSM) (Figure 6.3). The bulk indium (red trace) exhibits a narrow transition at about 3.36 K, consistent with literature reports(*7*). The mesoscopic sample, in contrast, exhibits a much broader transition beginning at 3.7 K, with the midpoint depressed to ca. 3.1 K.

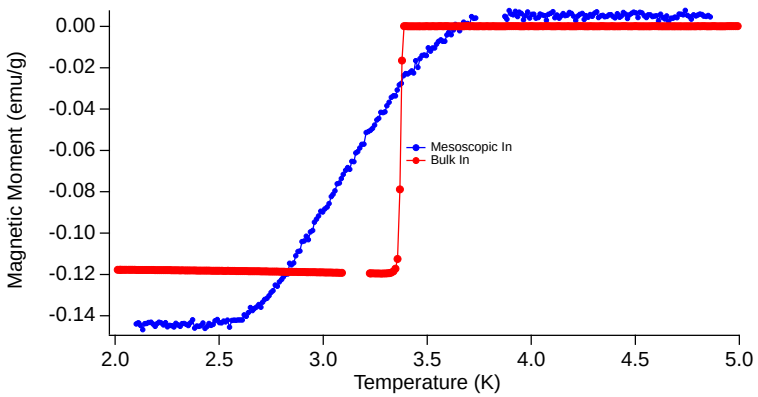

Figure 6.3: VSM Moment vs. Temperature measurement of bulk (red) and mesoporous (blue) indium. The transition midpoint is slightly depressed in the mesoporous sample, with the overall transition broadened.

The increase in the onset T_c in the mesostructured samples, while at first quite compelling, agrees well with predictions and measurements of small In particles(*8*), in which T_c in a confined system is observed to increase by as much as 15% in e.g. 10 nm diameter particles. This effect can be explained as changes in accessibility of the various phonon modes induced by the confined state. The overall depression of T_c is difficult to explain conclusively without more extensive studies; it may be related to the highly nonuniform infiltration of the material or to other factors.

To further probe the superconducting properties of the mesostructured material, we used field-dependent moment measurements (M vs. H) in the VSM (Figure 6.4). The bulk sample (Figure 6.4A, red), again as expected, exhibits a characteristic type-I curve with no hysteresis and a critical field H_c = 130 Oe, comparable to literature reports. In striking contrast, the mesoscopic sample exhibits a hysteretic curve most closely associated with type-II superconductors. The first critical field was lower than the bulk H_c at about 60 Oe, but the material remained superconducting to at least 1000 Oe – extrapolations suggest an upper critical field H_{c2} about 1500 Oe.

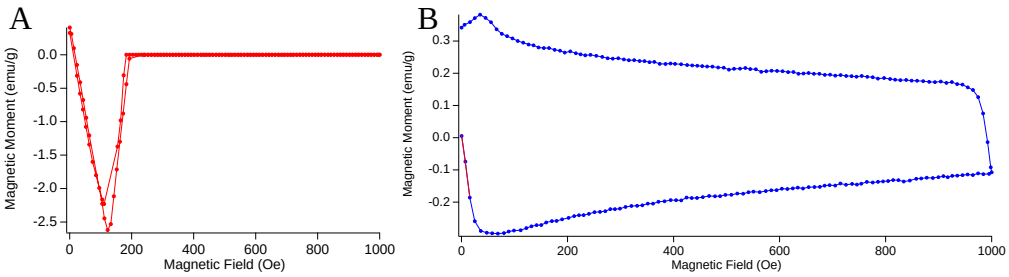

Figure 6.4: VSM Moment vs Field Scans of bulk (left) and mesostructured (right) Indium. The behavior changes from the non-hysteretic behavior characteristic of a type I material to hysteretic behavior consistent with a type II material, accompanied by an increase in critical field from 150 Oe to ca. 1200 Oe.

The change of the superconductor type can be understood as a function of the underlying material properties and length scales. The seminal BCS theory(*9*) classifies the superconducting type as a function of the specific energy for a superconductor-normal interface; in cases where the interface has negative energy, formation of vortices is favorable and the material can access the type II state, while in cases where the interface has positive energy there is no driving force for vortex formation and the material exhibits type I behavior. This interfacial energy, in turn, is

determined by the balance between the coherence length for Cooper pairs in the material (ξ_0) and the London penetration depth (λ_L). If $\xi_0 < \lambda_L$, the material is type II. The London penetration depth is essentially intensive, but the coherence length depends intrinsically on the mean free path for an electron in the material. In this complex, confined geometry the mean free path is highly directional, ranging from about 10 nm in the surface normal direction to several um along certain crystallographic directions. We hypothesize that the nature of the confinement reduces the overall coherence length – as probed by this particular orientation – from the bulk value of 250 nm to below the London penetration depth of 40 nm(*10*), causing the conversion from type I to type II. In principle, careful angle-dependent measurements should allow the switching of the material between the two states depending on the orientation relative to the incident magnetic field.

Conclusions and Future Outlook

These first VSM measurements of polycrystalline In gyroids present substantial promise for high-pressure infiltration of metals into single-crystal templates as a route for fabrication of mesoporous superconductors. While indium was chosen as a first target purely for its low melting point and accessible superconducting transition, a metal without known confinement effects on T_c such as lead(*11*) would allow the facile deconvolution of mesoscale order-induced effects from those due merely to the confinement of the superconductor. Substantial modifications to the high-pressure/high-temperature infiltration apparatus, borrowing insight from the geosciences(*12*), might allow the extension from relatively low-melting metals such as

In, Pb, and Sn to metals useful for catalytic or photonic applications such as aluminum (T_m= 660 ˚C), silver (T_m = 962 ˚C), or even gold (T_m = 1064 ˚C). The combination of high-pressure infiltration and single crystal templates presents a plethora of potential projects bridging, at long last, the disparate fields of soft matter and electronic materials.

REFERENCES

1. S. W. Robbins *et al.*, *Sci. Adv.* **2**, e1501119 (2016).
2. P. A. Beaucage, F. J. DiSalvo, S. M. Gruner, U. B. Wiesner, *Manuscr. Prep.*
3. E. M. Susca, P. A. Beaucage, A. Singer, L. A. Estroff, U. B. Wiesner, *Revis.*
4. S. C. Warren *et al.*, *Nat. Mater.* **11**, 460–467 (2012).
5. A. E. Aliev, S. B. Lee, A. A. Zakhidov, R. H. Baughman, *Phys. C Supercond.* **453**, 15–23 (2007).
6. Quantum Design, “Using PPMS Superconducting Magnets at Low Fields” (2009).
7. J. H. P. Watson, *Phys. Rev. B.* **2**, 1282–1286 (1970).
8. S. Matsuo, H. Sugiura, S. Noguchi, *J. Low Temp. Phys.* **15**, 481–490 (1974).
9. J. Bardeen, L. N. Cooper, J. R. Schrieffer, *Phys. Rev.* **108**, 1175–1204 (1957).
10. R. A. Anderson, D. M. Ginsberg, *Phys. Rev. B.* **5**, 4421–4434 (1972).
11. C. R. Leavens, E. W. Fenton, *Phys. Rev. B.* **24**, 5086–5092 (1981).
12. D. T. Griggs, *J. Geol.* **44**, 541–577 (1936).

APPENDIX

Materials

Double gyroidal single crystal Si(ON) ceramic templates were prepared using a previously-described method(*3*). In brief, a poly(isoprene-b-styrene-b-dimethylaminoethylmethacrylate) "ISA" triblock terpolymer with overall molar mass 79 kDa was mixed with a commercial poly(urea-methyl-vinyl-silazane) "Ceraset" in a predetermined loading to give the double-gyroid phase in toluene. The resulting solution was allowed to evaporate in a double-diffusion cell at 50 ˚C over a span of about two weeks, yielding a morphology with large planar regions. These regions were then cut from the surrounding film and heated to 1100 ˚C in flowing ammonia gas to produce freestanding, gyroidal single crystals of SiON.

Indium wire was purchased from the Indium Corporation and was cut into ca. 1cm sections and cleaned prior to use by rinsing in 10% hydrochloric acid (HCl), which was then removed using isopropyl alcohol. The sections were stored under isopropanol until use to inhibit oxide growth.

Methods

High Pressure Infiltration

Sample infiltration was performed in a custom-built high pressure / high temperature cell, using a high pressure manifold described previously with some modifications. The cell consisted of a set of HIP stainless steel fittings rated for 60,000 psig, wrapped in a fiberglass-jacketed heat tape, with a K type thermocouple embedded in the fitting thread using thermal grease. Samples to be infiltrated were placed in ca. 3 cm long, 4 mm diameter glass tubes with one end sealed in order to contain the molten In and

avoid contamination of the stainless steel cell walls. An activated carbon filter was placed between the cell and the rest of the manifold system to prevent indium vapor contamination of other parts of the apparatus. The temperature just beyond this carbon filter was actively monitored to check for any potential annealing behavior in the manifold itself.

The manifold was connected to a portable turbomolecular pump (Edwards Inc) capable of reaching a base pressure of about 10^{-7} torr; the line routinely reached this base pressure during pump-out.

In a typical infiltration cycle, a SiON single crystal was placed in the bottom of a glass tube. One or two 1cm pieces of In wire, cleaned as described, were quickly removed from isopropanol, placed in the tube, and the tube inserted into the reactor. The reactor was then connected to the pressure manifold and the vacuum pump started, typically within 2 min of removal of the In from the isopropanol bath. The sample was then allowed to degas until the pump reached its base pressure, typically 2-3 days at ambient temperature. Before high-pressure infiltration, the valve to the pump was closed and the line backfilled with helium gas. The cell was then heated at about 10 $^{\circ}$C min^{-1} to 200 $^{\circ}$C and the high pressure pump switched on until the manifold pressure reached about 2 kbar (ca 30,000 psi). This pressure was held, running the pump as necessary, for about an hour. The heating was then switched off and the cell allowed to cool to 60 $^{\circ}$C, ca 1 hr, at which point the system was depressurized. The In-SiON composite flakes were removed by breaking the glass tube and carefully heating the In slug until it melted

Scanning Electron Microscopy

The scanning electron micrograph in figure 6.2 was taken using a Zeiss Gemini 500 microscope operated at an accelerating voltage of 1 kV with an in-lens backscattered-electron detector. The sample was prepared by freeze-fracturing a bulk infiltrated sample, the fracture surface of which was then polished smooth.

Vibrating Sample Magnetometry

VSM data were taken using the Quantum Design VSM add-on for the Physical Property Measurement System (PPMS), equipped with a cryostat capable of accessing temperatures from 1.8 K to 400 K, a 9 T superconducting magnet, and an EverCool II Helium Reliquefier. The mesoporous indium piece was mounted using LakeShore cryogenic varnish on a quartz brace, which was then press-fit into a brass half-tube with the polished surface normal to the magnetic field. A small piece of In wire was mounted similarly and mounted with the wire drawing direction parallel to the magnetic field.

In both cases, the sample was cooled to 2.0 K with no applied field, then a small field of 20 Oe was applied to locate the sample by scanning the VSM transport through its range. It should be noted that the 9 T superconducting magnet used in the VSM has a mean field error of 20 gauss (ca. 20 Oe), (*6*) making precise determination of the exact field difficult; however, the field is highly stable once set.

For moment vs field measurements, the sample was located, using the above procedure, then warmed to 5 K and zero-field-cooled to erase any magnetic history. The field was ramped at 5 Oe sec^{-1} to 1000 Oe, then back to 0 Oe.

CHAPTER 7

CONCLUSION

This dissertation has explored a wide variety of pathways to the synthesis of mesostructured superconductors using block copolymer-inorganic hybrid co-assembly, including routes to niobium oxynitrides, niobium carbonitrides, and mesostructured metals.

In chapter two, I presented a route to the first block copolymer self-assembly derived mesostructured superconductor – niobium nitride with the alternating gyroid ($I4_132$) structure. The resulting materials had a T_c of about 7.8 K, dramatically below the best literature reported values of ca. 15 K, likely due to retained oxygen fraction in the material (ca. 45% O/(O+N) by XRD analysis). Nevertheless, the first potential evidence of flux pinning in such a material is observed as inflection points in high field-dependent magnetization. Further exploration of these phenomena, however, require a substantial increase in both the inorganic material quality, structure retention, and mesoscopic domain size, as realized in chapters four and six.

In chapter three, I expanded this synthetic route from custom ABC triblock terpolymers to commercially available Pluronics ABA poly(ethylene oxide-b-propylene oxide-b-ethylene oxide) triblocks using *in situ* small- and wide-angle x-ray scattering (SAXS/WAXS) during ammoniolysis. The resulting hexagonally ordered niobium nitride is not superconducting, but demonstrates that the *in situ* apparatus developed is an enabling technique for the discovery of synthetic pathways to such

materials. In addition, the ordered nitrides may prove to be interesting materials for catalysis or other applications. This technique, particularly when coupled with the capabilities of an upgraded Cornell High Energy Synchrotron source, may result in the rapid screening and discovery of routes for thermally processed mesoporous materials of a wide variety of classes – nitrides, carbides, oxides, and potentially others.

In chapter four, I extended the methodology developed in chapter two to produce niobium carbides by annealing a preliminary nitride in a blend of methane, hydrogen, and nitrogen at 1000 ˚C. The resulting carbides had improved structure retention (relative to the nitrides from chapter two) and exhibit nearly two orders of magnitude higher flux exclusion and T_c as high as 16 K. This synthetic route was used to demonstrate the versatility of the block copolymer-derived synthesis by preparing materials with four different morphologies from a single parent ISO triblock terpolymer: hexagonal cylinders, the double-gyroid matrix ($Ia3d;Q^{230}$), perforated lamellae, and the alternating gyroid network phase ($I4_132;Q^{214}$). Interestingly, the superconducting transition temperature of the four morphologies vary by as much as 4 K from morphology to morphology with minimal variation of the underlying lattice parameter – suggesting that confinement effects or even potentially effects of the order may be influencing the superconducting behavior. Preliminary data also shows flux avalanches at exceptionally high field (between 1000 Oe and 40,000 Oe) that may be consistent with unexpected mechanisms of flux intrusion into the material. With the expansion of the block copolymer-derived synthetic route to the carbonitrides, high-quality superconductors with good structural control can be readily realized, opening the door to a wide variety of systematic mesostructure-superconductivity correlation

studies. However, one critical remaining issue is compositional variability between samples. Because the carbonitrides are produced via gas-phase annealing, materials with different gas accessibility and material dimensions – i.e, different mesostructures – will necessarily have different lattice parameters and material compositions. This simple challenge prevents any direct mesostructured material – bulk material comparisons, making fundamental studies exceptionally difficult, despite the exceptional quality of both the mesostructure and underlying superconductor.

In chapter five, a method was developed using laser spike annealing and microbeam synchrotron diffraction to perform high-throughput studies of material processing, a technique we term XLAM (X-ray Laser Anneal Mapping). This method can be readily applied to high-throughput annealing studies of mesostructured materials (e.g. by performing combined microbeam GISAXS-WAXS) and may result in the discovery of processing regimes that lead to other families of block copolymer-derived mesostructured superconductors, e.g. complex oxides, but is first applied, as proof of principle, to unstructured thin films of bismuth oxide. The delta phase of bismuth oxide has the highest known oxygen ion conductivity of any solid oxide, but is only stable above 730 ˚C. Using XLAM, the delta phase was stabilized to room temperature, resulting in a material with an oxygen ion conductivity of 10^{-5} S cm^{-1}, the highest reported value for any solid oxide at room temperature by several orders of magnitude. The XLAM technique presents the possibility to perform high-throughput studies of crystal growth in mesostructured materials in a way that might lead to the rapid discovery of whole new families of mesostructured superconductor materials.

In chapter six, a route to block copolymer derived mesoporous superconductors is developed based on infiltration of a mesostructured Si(O,N) ceramic with molten indium at pressures around 30,000 psi. The resulting material's field-dependent magnetization behavior switches from a classic type-I system (as measured for bulk In) to a hysteretic curve characteristic of a type-II material. The critical field at which no superconducting fraction remains is enhanced from about 150 Oe to well over 1200 Oe. This result may be a consequence of the confinement of the material to a small thickness, with resulting dramatic decrease in the coherence length allowing the existence of vortices in the material. This methodology can be readily expanded to single mesocrystals of Si(ON) ceramics recently developed. It is expected that the compositional stability offered by this technique can be combined with improved apparatus to enable infiltration of a wider variety of high-melting metals and even potentially compounds. The Si(ON) templates' exceptional stability (up to ca. 1400 $^{\circ}$C) may further enable a wide variety of inorganic techniques for improvement of inorganic material quality, e.g. thermal zone refining to grow crystalline domains. Template removal *via* hydrofluoric acid etching, coupled with complementary infiltration or deposition strategies, may also enable the synthesis of multicomponent interfacial materials, taking advantage of the block copolymer-derived materials' exceptionally high specific surface area. It is expected that this platform will enable an exceptionally wide array of systematic mesostructure-superconductivity correlation studies and even broader work on emergent electromagnetic, mechanical, and other properties of ordered, single-mesocrystal nanocomposite materials.